

# **Free-Boundary Problem of Crack Dynamics: Phase-Field Modeling**

Von der Fakultät für Mathematik, Informatik und Naturwissenschaften  
der RWTH Aachen University zur Erlangung des akademischen Grades  
eines Doktors der Naturwissenschaften genehmigte Dissertation

vorgelegt von

Diplom-Physiker  
Clemens Gugenberger

aus Filderstadt-Plattenhardt

Berichter: Universitätsprofessor Dr. Heiner Müller-Krumbhaar  
Universitätsprofessor Dr. Walter Selke

Tag der mündlichen Prüfung: 9. Dezember 2008

Diese Dissertation ist auf den Internetseiten der Hochschulbibliothek online verfügbar.

# Abstract

This thesis describes the behavior of cracks and pores under the influence of elastic and curvature effects. In a continuum theory approach, these structure deformations are treated as free moving boundaries. Our investigation starts with well established sharp interface equations for which no fully dynamical solutions exist so far. The equations include only linear dynamical elasticity, surface energy and non-equilibrium transport theory. By proper use of the phase-field concept, we are now able to tackle the fully time-dependent free moving boundary problem to describe crack propagation in a fully self-consistent way. We concentrate on two material transport processes, namely surface diffusion and phase transition dynamics.

We show analytically that the intuitive and widely used approach for constructing a phase-field model for surface diffusion fails, since it does not reduce to the desired sharp interface equations, providing an uncontrolled approximation to the dynamics. We then develop two completely new models that ensure the correct asymptotic behavior and support our analytical findings by numerical simulations, which are computationally very demanding due to the high order equations that have to be solved.

We therefore derive another phase-field model based on a phase transition process. Incorporating elastodynamic effects into the theory makes the simultaneous self-consistent selection of a tip radius scale and the propagation velocity possible. Our simulations show that it describes the complicated tip behavior and the elastic far-field behavior correctly, also allowing the numerical extraction of quantities like the stress intensity factor. Our results agree with those found in the literature for the case of steadily propagating cracks and extend them into the previously unaccessible parameter regime of large elastic driving forces. Here, we are able to resolve a dynamical tip-splitting instability, in agreement with experimental observations.

Structures that are subjected to external loading often contain many small cracks already, which can weaken the structure substantially, depending on the initial crack density. We performed simulations of static inclusions and compared the results with the predictions we obtained with analytic approximation schemes. The use of our scheme reveals that the complicated three-dimensional behavior of the elastic modulus as a function of the crack density for randomly oriented cracks reduces to a simple exponential decay and exhibits the inability of the often used differential homogenization method to predict percolation, i. e. breaking of the system. The parallel arrangement of slit-like cracks, where percolation does not occur, is not easily accessible to the standard analytical techniques. We could show by use of thin-plate theory, scaling arguments and numerical calculations that for this geometrical setup, the relevant effective elastic constant decays not exponentially as for randomly oriented cracks, but as a power-law instead. Our method can thus describe morphological surface instabilities, fast crack propagation and even the collective behavior of multi-cracked materials with high quantitative precision.

# Zusammenfassung

Diese Arbeit beschreibt das Verhalten von Rissen und Poren, die dem Einfluss elastischer und Krümmungseffekte ausgesetzt sind. Diese Strukturdeformationen werden im Rahmen einer Kontinuumsmechanik als freie Randwertprobleme behandelt. Unsere Untersuchungen basieren auf gut etablierten Gleichungen für scharfe Grenzflächen, für die bisher keine vollständig dynamischen Lösungen existieren. Diesen Gleichungen liegen ausschließlich lineare dynamische Elastizitätstheorie, Oberflächenenergie-Effekte und Nichtgleichgewichts-Transporttheorie zugrunde. Durch sorgfältige Anwendung des Phasenfeld-Ansatzes sind wir damit in der Lage, das vollständige zeitabhängige freie Randwertproblem zu behandeln und Rissausbreitung auf selbstkonsistente Art und Weise zu beschreiben. Wir konzentrieren uns dabei auf zwei Materialtransportprozesse, Oberflächendiffusion und Phasenübergangsdynamik.

Wir zeigen analytisch, dass der intuitive und weit verbreitete Ansatz, ein Phasenfeld-Modell für Oberflächendiffusion zu entwickeln, fehlschlägt, da er nicht auf den verlangten Grenzfall für scharfe Grenzflächen zurückführt und somit eine unkontrollierte Approximation an die Dynamik darstellt. Wir entwickeln zwei neue Modelle, die das korrekte asymptotische Verhalten aufweisen und untermauern unsere analytischen Ergebnisse numerisch, wobei die Simulationen wegen der hohen Ordnung der zu lösenden Gleichungen numerisch sehr aufwendig sind.

Deswegen leiten wir ein weiteres Phasenfeld-Modell her, das auf einem Phasenumwandlungsprozess basiert. Durch Berücksichtigung elastodynamischer Effekte ist die gleichzeitige selbstkonsistente Selektion einer Skala des Rissspitzenradius und der Ausbreitungsgeschwindigkeit möglich. Unsere Simulationen zeigen, dass das Modell das komplizierte Verhalten der Rissspitze und der elastischen Fernfelder richtig beschreibt und es auch ermöglicht, Größen wie den Spannungsintensitätsfaktor numerisch zu bestimmen. Unsere Ergebnisse stimmen für den Fall mit konstanter Geschwindigkeit propagierender Risse mit denen in der Literatur überein und erweitern sie in den vorher unzugänglichen Bereich großer elastischer treibender Kräfte. Dort sind wir in der Lage, eine dynamische Rissspitzen-Instabilität aufzulösen, in Übereinstimmung mit experimentellen Beobachtungen.

Strukturen, die externen Belastungen ausgesetzt sind, enthalten oft schon viele kleine Risse, die diese Struktur abhängig von der Rissdichte erheblich schwächen können. Wir simulieren statische Einschlüsse und vergleichen die Ergebnisse mit Vorhersagen, die wir aus analytischen Näherungsmethoden gewonnen haben. Unsere Methode zeigt, dass sich das komplizierte dreidimensionale Verhalten des Elastizitätsmodul als Funktion der Rissdichte zufällig orientierter Risse in zwei Dimensionen auf einen einfachen exponentiellen Abfall reduziert. Dies belegt, dass die oft verwendete Methode der differentiellen Homogenisierung Perkolations, also den Bruch des Systems, nicht vorhersagen kann. Für die analytisch schwer zugängliche parallele Rissanordnung, bei der Perkolations nicht auftritt, können wir unter Verwendung von Theorie dünner Platten, Skalenargumenten und numerischer Rechnungen zeigen, dass die relevanten effektiven elastischen Konstanten hier nicht exponentiell, sondern algebraisch abfallen. Unsere Methode kann somit morphologische Oberflächeninstabilitäten, Rissausbreitung und das kollektive Verhalten von Materialien, die viele Risse enthalten, mit hoher quantitativer Genauigkeit beschreiben.

# Contents

<b>1. Overview</b>	<b>1</b>
<b>2. Introduction</b>	<b>5</b>
2.1. Continuum Theory of Elasticity . . . . .	5
2.1.1. Displacement Vector . . . . .	5
2.1.2. Strain Tensor . . . . .	6
2.1.3. Stress Tensor . . . . .	8
2.1.4. Solving Elastic Problems . . . . .	9
2.1.5. Relation Between Strain and Stress: Hooke's Law . . . . .	10
2.1.6. Plane Strain Loading . . . . .	13
2.2. Continuum Fracture Mechanics . . . . .	14
2.2.1. Modes of External Loading . . . . .	16
2.2.2. The Griffith-Criterion: Scaling Analysis . . . . .	17
2.2.3. Near-Tip Behavior: The Square Root Singularity . . . . .	19
2.2.4. Dynamic Effects . . . . .	20
2.3. Transport Mechanisms . . . . .	22
2.4. Asaro-Tiller-Grinfeld-Instability . . . . .	23
2.4.1. Interface Kinetics . . . . .	23
2.4.2. The Time Cusp Singularity . . . . .	27
2.5. The Phase-Field Method . . . . .	28
2.5.1. Constructing a Phase-Field Model . . . . .	29
2.6. Conclusion . . . . .	33
<b>3. Phase-Field Models for Surface Diffusion</b>	<b>35</b>
3.1. Phase-Field Modeling for Surface Diffusion . . . . .	35
3.2. Sharp-Interface Model for Motion Induced by Curvature . . . . .	36
3.3. Scalar-Mobility Phase-Field Model . . . . .	38
3.3.1. The Traditional Approach . . . . .	38
3.3.2. Local Coordinate System . . . . .	39
3.3.3. Inner Equations . . . . .	41
3.3.4. Expansions, Matched Asymptotic Analysis . . . . .	41
3.4. Tensorial Mobility . . . . .	46
3.5. Modified Tensorial Mobility Models with Correct Asymptotics . . . . .	49
3.6. Globally Conservative Model . . . . .	49
3.6.1. Restoring Global Conservation . . . . .	51
3.7. The Rätz-Ribalta-Voigt-Model . . . . .	52
3.8. Conclusion . . . . .	53

<b>4. Phase-Field Simulations of Surface Diffusion</b>	<b>55</b>
4.1. The Free Model . . . . .	56
4.1.1. Numerical Stability . . . . .	56
4.1.2. Interface Stability . . . . .	56
4.1.3. Elliptical Inclusions . . . . .	63
4.2. Surface Diffusion with Elastic Effects . . . . .	64
4.2.1. Elliptical Inclusions with Elasticity . . . . .	64
4.2.2. Quantitative Analysis of the Grinfeld Instability . . . . .	68
4.3. Conclusion . . . . .	73
<b>5. Fast Crack Propagation with Phase-Transformation Kinetics</b>	<b>75</b>
5.1. Sharp Interface Equations . . . . .	76
5.2. Fast Crack Propagation: Selection Principles . . . . .	79
5.2.1. Multipole Expansion Method . . . . .	80
5.3. Phase-Field Modeling for Crack Propagation . . . . .	84
5.3.1. Extrapolation . . . . .	86
5.4. Conclusion . . . . .	96
<b>6. Collective Behavior of Multi-Cracked Material</b>	<b>99</b>
6.1. Differential Homogenization Method . . . . .	100
6.1.1. Two- and Three Dimensional Elasticity . . . . .	102
6.2. Random Distribution of Spherical Holes . . . . .	103
6.3. Random Distribution of Elliptical Cracks . . . . .	107
6.3.1. Crack Density Parameter . . . . .	108
6.3.2. Iterated Homogenization for Randomly Oriented Cracks . . . . .	109
6.4. Asymptotic Behavior of Parallel Cracks . . . . .	115
6.5. Conclusion . . . . .	119
<b>7. Summary</b>	<b>121</b>
<b>A. Appendix</b>	<b>125</b>
A.1. Derivation of the Sharp Interface Equations . . . . .	125
A.2. Matching Conditions . . . . .	129
A.3. Homogenization Method for One-Dimensional Springs . . . . .	130
A.4. Effective Elastic Constants for a Regular Array of Cracks . . . . .	131
A.5. Numerical aspects . . . . .	133
Bibliography . . . . .	144
<b>B. Acknowledgements</b>	<b>145</b>
<b>C. Publications</b>	<b>147</b>

# 1. Overview

The average commercially operated airplane is estimated to contain well over 25000 cracks. In fact, the existence of crack-like flaws cannot be precluded in any engineering structure. Cracks occur on all lengthscales, from microcracks in high precision structural elements to large constructs like dams and even geological formations. Of course, most cracks are harmless and do not necessarily lead to material failure; when they do, the result can be catastrophic. To illustrate this, the large number of sudden and disastrous fractures that occurred in the welded merchant ships of type “Liberty” during and after the second world war, serves as a prime example. Out of about 5000 welded ships, over 1000 suffered substantial structural damage through fracture, some of them breaking cleanly into two parts; the investigation of these incidents set the foundations for industrial engineering fracture mechanics.

Crack growth is ultimately driven by elastic forces, when elastic stresses become so high locally that the material fails. Elastic effects come into play whenever forces, external or internal, act on a solid, making elasticity almost ubiquitous in industrial applications, like aerospace and automotive industry, civil engineering, nuclear power generation and many more. Consequently, fracture mechanics has been mainly an engineering discipline, known as damage tolerance analysis, for a long time.

Despite the bold engineering claim that “it is unlikely that damage tolerance analysis can be much improved” [17], present physical understanding of fracture still leaves a lot to be desired. While for practical applications, the prevention of cracks is typically the largest concern, other aspects are physically interesting, like stability of motion, crack path prediction or energy release mechanisms. There are many different physical aspects that contribute to the crack behavior: strong plastic flows at the crack tip, creation and motion of dislocations, bond breaking and granular effects of the material. It is particularly the multiscale nature of crack propagation that provides such enormous challenges for solid state physics and materials science: Cracks concentrate the macroscopic elastic energy of a solid to release it spontaneously on atomic scales; it can creep at rates of less than an atom per second or propagate with the speed of sound.

Due to their multi-scale nature, it seems that cracks have to be tackled on atomistic as well as on larger scales. In the atomistic approach, cracks are understood on the level of breaking bonds between atoms, leading to sharp crack tips. There are, however, several problems inherent to this approach. It requires detailed information, either theoretical or empirical, about atomic properties and interactions, comprising an often intractable many particle problem. The proper description of atomic many particle systems is in itself a very active branch of research and makes any quantitative description of material behavior depend heavily on the chosen model and its parameters. Also, this approach is computationally inhibitive or outright unfeasible for simulating fracture processes on industrially relevant lengthscales. Furthermore, the required detail of information about

---

the system, like density and distributions of dislocations, is much greater than can be provided experimentally. Therefore, the resort to valid approximations and a more coarse-grained picture is unavoidable.

Other experimental results also indicate that certain features of crack growth are generic. For example, it has been observed that the steady state velocity of the crack tip saturates well below the Rayleigh speed, which is known to be the theoretical upper limit. When high tensions are applied, tip splitting occurs. Additionally, it is known that plastic effects in ductile and quasi-brittle materials can lead to extended, “round” crack tips. The fundamental question is whether the generic features can be explained in a generic way, using only simple and well established theoretical concepts.

In the 1920s, Griffith proposed his pioneering idea to describe crack growth as a competition of two different effects [42]: the *release of the elastic energy* in the material and the *increase of surface energy* due to crack growth. This idea proved to be very fruitful and since his pioneering works, numerous approaches have been developed to describe the various features of cracks. Integral energy balance criteria demonstrated how such an approach could be used to obviate the need for a direct description of the discrete and nonlinear events involved in crack propagation. The fundamental questions to be answered are: When does a crack grow? How fast does it grow? What determines the path and consequently the shape of a growing crack?

We do not want to describe crack propagation by bond breaking, which leads to diverging stresses at an infinitely sharp tip. Instead, we want to find minimal models for fracture in such a way that not only the crack speed, but also the crack shape can be determined self-consistently. Those minimal models are designed such that they are free of microscopic details and the only ingredients are *linear theory of dynamic elasticity*, *surface energy density contributions* and *non-equilibrium transport theory*.

In order to find such a minimal macroscopic model of fracture, the Asaro-Tiller-Grinfeld instability [3, 43] provides a good starting point. It states that the surface of a stressed body can be unstable; the system can reduce its elastic energy by developing morphological surface perturbations, finally leading to fast propagating notches that look and behave very similar to cracks. In contrast to conventional fracture mechanics, the crack has a finite tip radius in our description, and therefore propagation requires a mass transport process.

As another consequence, fracture mechanics can now be understood in the framework of interfacial pattern formation processes. For a large class of pattern-forming systems, the essential dynamics to be understood and described is that of an interface between two phases. Mathematically speaking, part of the problem to be solved consists in determining the position of the interface as a function of time, i. e. a fully time dependent free moving-boundary problem. This means that for all surface points of the extended crack the interface motion has to be expressed by the local driving forces. Simultaneously, the difficulty arises that the elastic fields have to be determined in domains that continuously change their shape in the course of time and are not known in advance. The advantage, however, is that no guesses for the equations of motion, especially at an otherwise singular tip, have to be made, but instead the propagation is based on well established transport theories.

Phase-field models have been established as powerful tools for the numerical simulation

---

of this kind of problem. They avoid explicit front tracking and are versatile enough to deal with topological changes. The idea is not to deal with a sharp boundary that has to be tracked explicitly, but rather with a diffuse interface of finite width, so that a set of differential equations, which are valid in the whole bulk, can be derived and solved numerically. The flexibility of the phase-field method comes at the prize that the interface width introduces a new numerical length-scale that has to be resolved: the phase-field description reduces to the original sharp interface problem only asymptotically, if the interface width is small compared to all other length scales in the problem.

So, the underlying questions in the present thesis are: Can a continuum model of a free moving boundary, driven by elastic and surface energy effects, describe crack propagation? Can the phase-field technique be used for a quantitative description?

All these questions concern the behavior of a single crack. However, many work-pieces, like the initially mentioned airplane, contain many cracks which are not necessarily propagating. The important questions to ask here are: How is the material weakened by the presence of cracks? Which roles play crack orientation and distribution? Of course, there are analytical approaches available which rely on simplifying assumptions. This naturally leads to the next question to be asked: How well do the analytical approximations describe a given setup compared to numerical simulations?

The thesis is organized as follows:

First, in **chapter 2**, we will give an introduction to linear theory of elasticity and the basics of fracture mechanics. We will then explain the Grinfeld instability and point out the connection to the conventional continuum description of fracture. Finally, the fundamental idea behind the phase-field method is outlined.

In **chapter 3** we focus on the first transport mechanism for crack propagation, which is surface diffusion. We will show how to construct a phase-field model based on the sharp-interface equations. However, modeling surface diffusion with the phase-field method exhibits delicate intricacies, which will be presented. From a physical point of view, surface diffusion kinetics have the desirable property that mass conservation for each phase is fulfilled automatically, but the resulting higher order equations are computationally much more demanding. We will show that the conventional approach to set up phase-field models for surface diffusion represents an *uncontrolled approximation* to the nonequilibrium problem. Two fundamentally new models that overcome this restriction are developed and shown to have the correct sharp interface asymptotics.

In **chapter 4**, our analytical findings are supplemented by numerical comparisons of all models. Various aspects of numerical simulations are treated like time discretization stability and stability against interface fluctuations. Additionally, we investigate the dynamics of an elliptical inclusion with and without coupling to external fields, showing that crack propagation by surface diffusion is possible. Finally, we investigate the early stage of the Grinfeld instability and compare the numerical precision of all implemented models with the analytic solution.



---

Next, in **chapter 5**, we will present a sharp interface model for fast crack propagation where the dynamics are based on a phase transformation process. It has the same scale selection mechanisms as the surface diffusion model, but the constructed phase-field model has a more benign numerical behavior than the one for surface diffusion. We will show that the model comprises many aspects of fast crack propagation, like a self-consistent scale selection and tip splitting for high driving forces. These results are compared to the ones obtained with the multipole expansion technique, which is a completely independent method that can be applied to solve the same minimal model equations. The upshot of these considerations will be that with a careful separation of lengthscales in the phase-field method, quantitative results with high accuracy can be obtained.

In **chapter 6**, we move on to investigate the elastic properties of materials that consist of a random mixture of different media, one of which can also be vacuum. This is important for heterogeneous materials like concrete which contains microcracks and where cracking is the predominant way of material failure. We investigate several different geometrical setups in two and three dimensions analytically. We then use our phase-field code to compare the analytical results with numerical simulations.

Finally, in **chapter 7** we will summarize our results.

## 2. Introduction

In this chapter, we will give a short introduction to the continuum theory of fracture mechanics. We start with linear theory of elasticity, which lies at the heart of all the following investigations. We will also present the basics of continuum fracture mechanics and point out the link to pattern formation descriptions provided by the Asaro-Tiller-Grinfeld instability.

### 2.1. Continuum Theory of Elasticity

When an external force acts on solid bodies, some break, some flow slowly, but many deform only to return to their original shape after the load has been removed. This capability of a deformed body to recover its original shape after deformation is called **ELASTIC** behavior. The range of loading for which solids react elastically to external forces is known as **ELASTIC RANGE**. When an elastic body deforms, it stores internal elastic energy to provide the necessary counterforce, distributing the effects of the external forces over its entirety. Robert Hooke discovered that in many cases, the deformation of a rigid body is proportional to the applied force. Since then, linear theory of elasticity provided the basis for countless engineering applications. Since many geometrical aspects enter the theoretical description, like the shape of the body, the way the external forces are applied, or an internal anisotropy of the material, most of the relevant quantities must be expressed as tensors. To render notation more compact, it is very common to use the Einstein sum convention. This convention states that if an index appears twice in a single term, summation has to be performed over all possible index values. Because theory of elasticity has always not only been important in physics, but also in engineering disciplines, there are many equivalent representations of the same fundamental relationships, which can make the theory appear overwhelming at first sight. There are various textbooks that cover the topics presented in this section [73, 17, 37] in much greater detail.

#### 2.1.1. Displacement Vector

If external forces act on a solid body, the body will generally be relocated, turned or deformed. Translation and rotation are *rigid body* motions, which means that the relative position between every two points will remain constant during the motion. Deformation, on the other hand, implies that the body can change its form as well as its volume, and the relative distances between two points change. This reaction is described by assigning each vector  $\underline{r}^0$  (with components  $(r_x^0, r_y^0, r_z^0)$ ) of the undeformed body a vector  $\tilde{\underline{r}}$  of the deformed body. The **DISPLACEMENT VECTOR**  $\underline{u}$  is then defined as the difference of the

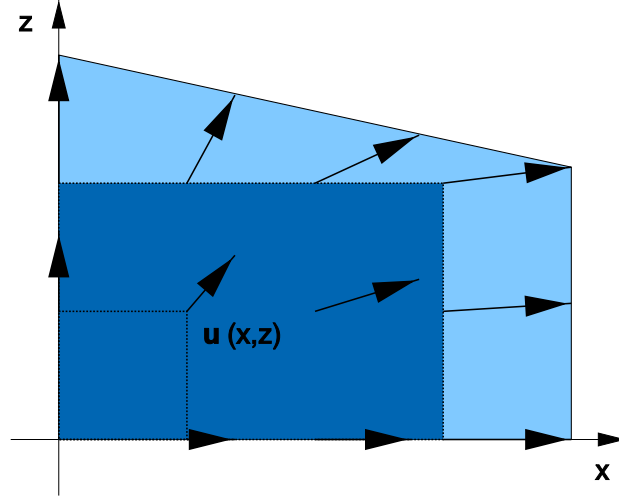


Figure 2.1.: Displacement field of an elastically deformed body

positions before and after the deformation:

$$\underline{u} = \tilde{\underline{r}} - \underline{r}^0 \quad (2.1)$$

and has dimension of a *length*. Since the new coordinates  $\tilde{x}_i(x, y, z)$  are functions of the original coordinates  $x_i^0$ , the displacement vector field  $\underline{u}(\underline{r}^0) = \underline{u}(x, y, z)$  is a function of the original coordinates  $x_i^0$ .

### 2.1.2. Strain Tensor

The displacement field as given in Eq. (2.1) still contains rigid body movements, i. e. pure translations and pure rotations, mixed with what one would call deformation. Since the displacement field is constant for a pure translation, it can be eliminated by going from  $\underline{u}(\underline{r})$  to  $\nabla \underline{u}$ . This elimination leads to the definition of the DISTORTION TENSOR  $\underline{\underline{\beta}}$  as

$$\underline{\underline{\beta}} = \nabla \underline{u} \quad \beta_{ij} = \nabla_i u_j = \frac{\partial u_j}{\partial x_i} \quad (2.2)$$

where the last expression is only valid in cartesian coordinates. In order to eliminate rotations, which are still contained in Eq. (2.2), one decomposes the tensor in a *symmetrical* part  $\underline{\underline{\epsilon}}$ , called STRAIN TENSOR, and a *antisymmetrical* part  $\underline{\underline{\omega}}$ .

$$\underline{\underline{\beta}}^{sym} = \underline{\underline{\epsilon}} \quad \epsilon_{ij} = \frac{1}{2}(\beta_{ij} + \beta_{ji}) \quad (2.3)$$

$$\underline{\underline{\beta}}^{asym} = \underline{\underline{\omega}} \quad \omega_{ij} = \frac{1}{2}(\beta_{ij} - \beta_{ji}) \quad (2.4)$$

$$\underline{\underline{\beta}} = \underline{\underline{\epsilon}} + \underline{\underline{\omega}} \quad (2.5)$$

In the case of the so-called GEOMETRICAL LINEARIZATION, which states that  $\underline{\underline{\beta}}$  is small (i.e.  $\beta_{ij} \ll 1$ ), the antisymmetric tensor  $\underline{\underline{\omega}}$  can be mapped to a rotation vector (axis)  $\underline{\varphi} = 1/2 \nabla \times \underline{u}$ :

$$\omega_{ij} = \varepsilon_{ijk} \varphi_k \quad \varphi_i = \frac{1}{2} \varepsilon_{ijk} \beta_{ik} = \frac{1}{2} \varepsilon_{ijk} \frac{\partial u_k}{\partial x_j} \quad (2.6)$$

where  $\varepsilon_{ijk}$  denotes the Levi-Civita-symbol. Note that the geometrical linearization is different to Hooke's law, which is a linearization due to a material constitutive law and will be defined in section 2.1.5. One should also note that since all considerations we presented so far are of pure geometrical nature, they also apply to plastically deforming systems.

The strain tensor  $\underline{\underline{\epsilon}}$  enables us to calculate the change of distance between neighboring points. For the distance  $dl'$  of two points *after* the deformation, we have:

$$dl'^2 = dl^2 + 2\epsilon_{ij} dx_i dx_j \quad , \quad (2.7)$$

with the strain tensor  $\epsilon_{ij}$  given by the following equation:

$$\epsilon_{ij} = \frac{1}{2} \left( \frac{\partial u_i}{\partial x_j} + \frac{\partial u_j}{\partial x_i} + \frac{\partial u_k}{\partial x_i} \frac{\partial u_k}{\partial x_j} \right) \quad (2.8)$$

where the indices  $i, j$  and  $k$  run from 1 to 3, denoting the cartesian components. The strain tensor has the dimension of a scalar and is symmetric,  $\epsilon_{ij} = \epsilon_{ji}$ , by construction. Please note that even though  $\epsilon_{ij}$  may be small, the displacement vectors  $\underline{u}$  could still be large, as can be understood intuitively by thinking of a long thin bent rod.

The step to LINEAR theory of elasticity is to assume that the values of the displacement vector are also small, so that the nonlinear (i.e. second order) elements of the full strain tensor can be dropped, reducing it to:

$$\epsilon_{ij} = \frac{1}{2} \left( \frac{\partial u_i}{\partial x_j} + \frac{\partial u_j}{\partial x_i} \right) . \quad (2.9)$$

If the strain is prescribed, Eq. (2.9) can be understood as system of six differential equations for the determination of three components of the displacement vector, resulting in an overdetermined system. Thus, not all arbitrary strain relations lead to a solution for the displacements. By satisfying the SAINT-VENANT COMPATIBILITY CONDITION

$$\frac{\partial^2 \epsilon_{ij}}{\partial x_k \partial x_l} + \frac{\partial^2 \epsilon_{kl}}{\partial x_i \partial x_j} = \frac{\partial^2 \epsilon_{il}}{\partial x_j \partial x_k} + \frac{\partial^2 \epsilon_{jk}}{\partial x_i \partial x_l} , \quad (2.10)$$

the number of independent equations is reduced to three and a unique solution can be obtained.

The trace of the strain tensor is an invariant and therefore independent of the chosen system of coordinates. The non-diagonal elements describe shear deformations, which do not lead to any volume change. Every deformation can be written as

$$\epsilon_{ij} = \frac{1}{3} \delta_{ij} \epsilon_{kk} + \left( \epsilon_{ij} - \frac{1}{3} \delta_{ij} \epsilon_{kk} \right) , \quad (2.11)$$

which is the sum of a pure volume change and a pure shape change. Remember that we use the Einstein convention to sum over the double index  $k$ .

The change of volume of the deformed body is given by

$$dV' = dV(1 + \epsilon_{ii}), \quad (2.12)$$

which means that the relative volume change can be written as

$$\frac{dV}{V} = \epsilon_{ii} = \text{Tr } \underline{\underline{\epsilon}} = \frac{1}{2} (\nabla_i u_i + \nabla_i u_i) = \nabla \cdot \underline{u}. \quad (2.13)$$

### 2.1.3. Stress Tensor

In the nondeformed state, all particles of a body stay at their thermodynamical equilibrium position due to the absence of deforming forces. As soon as the body is deformed elastically, there are inner forces trying to move the particles back to their equilibrium position. For a specific volume element, the resulting acting force  $F$  is given by the forces from all the neighboring volume elements,

$$\underline{F} = \int \underline{f}_{int} dV, \quad (2.14)$$

where  $\underline{f}_{int}$  denotes the internal force density. Under the natural assumption that the interaction range of the inner force is small, making it a local theory, the forces of the neighboring volume elements are only transferred via the surface of those elements. Therefore, each component  $F_i$  the resulting force can be written as a surface integral over all forces acting on the surface of our chosen volume element. From tensor analysis follows that the force density  $\underline{f}$  can be expressed as the divergence of a second order tensor  $\underline{\underline{\sigma}}$ :

$$\int f_i dV = \int \frac{\partial \sigma_{ij}}{\partial x_j} dV = \oint \sigma_{ij} ds_j, \quad (2.15)$$

where  $ds_j$  is the  $j$ -th component of the surface elements. The physical meaning of the stress tensor is that its  $i$ -th component gives the elastic force density that acts on a plane that has the normal vector  $\underline{e}_j$ :

$$f_i = \sigma_{ij} \cdot e_j \quad (2.16)$$

Conservation of angular momentum requires the symmetry of  $\underline{\underline{\sigma}}$ .

Those internal forces, which are called STRESSES, increase the internal energy of the body, because the deforming forces are performing work, or in short:

*Stresses are the energetic response to a strain.*

The above statement leads to an equivalent way of defining stress: it is the response of the local free energy density  $W$  to the strain  $\epsilon$ ,

$$\sigma_{ij} = \frac{\partial W}{\partial \epsilon_{ij}}. \quad (2.17)$$

Since a static situation leaves the temperature constant, the relevant thermodynamic potential is the free energy. With the local free energy density  $W$ , the total free energy is given by

$$E = \int W dV . \quad (2.18)$$

So, what does  $W$  depend on? Surely not directly on the displacement, since a pure translation does not increase the internal energy. Nor does a pure rotation, so the remaining candidate is the strain  $\underline{\underline{\epsilon}}$ . In classical theory of elasticity, it is assumed that

$$W(\underline{\underline{\epsilon}}) = W(\underline{\underline{\epsilon}}(\underline{\underline{r}})) , \quad (2.19)$$

and  $W$  does not depend on  $\nabla\epsilon$ ,  $\nabla\omega$  or higher derivatives.

To obtain the equations of motion for an elastic medium, the force density transferred by the stresses  $\partial\sigma_{ij}/\partial x_k$  and by external volume forces  $g_i^{ext}$ , like gravity, must be set equal to the product of the acceleration of the mass particles  $\ddot{u}_i$  and the mass density  $\rho$ :

$$\frac{\partial\sigma_{ij}}{\partial x_j} + \rho g_i^{ext} = \rho \ddot{u}_i \quad (2.20)$$

This is the general form of Newton's equation of motion for elastic systems; often, especially when looking for equilibrium conditions, the right hand side and external volume forces can be neglected, reducing Eq. (2.20) to the static elastic equilibrium condition

$$\frac{\partial\sigma_{ij}}{\partial x_j} = 0 \quad (2.21)$$

#### 2.1.4. Solving Elastic Problems

In general, the bulk solution of an elastic solid mechanics problem must fulfill

1. Equations of geometry or of motion
2. Compatibility of strains and displacements
3. Stress-strain relations or material constitutive laws.

We have seen that stresses are the body's energetic reaction to the internal or external forces acting on its surface. For dynamic problems, the six components of the stress tensor for an infinitesimal body element are related by the *three equations of motion*, which contain second order time derivatives of the displacements, see Eq. (2.20).

The second set of equations are the *strain-displacement* relations. They are *six equations of kinematics* that express the six components of the strain tensor in terms of the three components of the displacement tensor, see Eq. (2.10).

Since the first two sets of equations are independent of materials specific elastic properties, this material influence is contained in a third set of equations, the *constitutive* equations. They relate the components of the stress tensor to the components of the strain tensor and are known as HOOKE'S LAW in the linear case. This will be presented in the next section.

Altogether, there are 15 unknown quantities, six stress components, six strain components and three displacement components, which are given by 15 elastic equations. Of course, it has to be ensured that the appropriate number of boundary conditions are given for the elastic problem to be well defined.

### 2.1.5. Relation Between Strain and Stress: Hooke's Law

The necessary relation between strains and stresses to solve for the equilibrium condition when deforming forces are acting on a body are given by a constitutive law that is known as Hooke's law. Starting from the question how the internal energy density  $W$  depends on the strain, a Taylor expansion of  $W$  in  $\underline{\underline{\epsilon}}$  leads to

$$W(\underline{\underline{\epsilon}}) = A + B_{ij}\epsilon_{ij} + \frac{1}{2}C_{ijkl}\epsilon_{ij}\epsilon_{kl} + \dots \quad (2.22)$$

If the body is in equilibrium and no displacement is present, neither are strains and the energy density should be minimal. This means that the coefficients  $A$  and  $B_{ij}$  in Eq. (2.22) must vanish. Therefore, the first nonvanishing term is the one quadratic in  $\epsilon$ , resulting in the fundamental equation of linear theory of elasticity, Hooke's law:

$$\sigma_{ij} = \frac{\partial W}{\partial \epsilon_{ij}} = \frac{\partial}{\partial \epsilon_{ij}} \frac{1}{2} C_{klmn} \epsilon_{kl} \epsilon_{mn} = C_{ijkl} \epsilon_{kl} , \quad (2.23)$$

with  $i, j, k, l, m, n \in 1, 2, 3$ . The proportionality coefficient  $C_{ijkl}$  is a tensor of fourth order and has 81 components in three dimensions, and it is sometimes called HOOKE TENSOR or STIFFNESS TENSOR. One should remember that before restricting to a linear constitutive law, we also used a geometrical linearisation. Therefore, Eq. (2.23) does not pose a serious restriction to the applicability of the presented theory. Keeping higher order terms is normally not helpful, since most materials cease to be elastic if the strain  $\epsilon$  is very large.

One should keep in mind that due to the sum convention, this is a very compact notation of a system of equations, one for each component of  $\sigma$ , as in

$$\sigma_{11} = C_{1111}\epsilon_{11} + C_{1122}\epsilon_{22} + C_{1133}\epsilon_{33} + C_{1123}\epsilon_{23} + C_{1113}\epsilon_{13} + C_{1112}\epsilon_{12} . \quad (2.24)$$

However, due to symmetry arguments, the number of independent constants in  $C_{ijkl}$  is reduced substantially. Since the free energy is given by Eq. (2.22), and the strain tensor  $\epsilon$  is symmetric, the value of the product  $\epsilon_{ij} \cdot \epsilon_{kl}$  is invariant under the index permutations

$$C_{ijkl} = C_{jikl} = C_{ijlk} = C_{klij} , \quad (2.25)$$

reducing the number of independent components to 21. Depending on the underlying crystal's symmetry properties, this number is reduced even further: for an orthorhombic system, there are nine independent values in  $C_{ijkl}$ ; in hexagonal crystals, there are five; in cubic crystals three; and for isotropic materials, there are only two remaining independent components. The COMPLIANCE TENSOR describes the inverse relation to the stiffness tensor,

$$\epsilon_{ij} = S_{ijkl}\sigma_{kl} \quad (2.26)$$

and has the same symmetry properties. Even though it is counterintuitive to denote the stiffness tensor by  $C$  and the compliance tensor by  $S$ , we adhere to the common convention.

With only so few non-vanishing components in the Hooke tensor, it is very common for practical applications to write  $C_{ijkl}$  using the VOIGT NOTATION, where the symmetric tensors  $\underline{\underline{\epsilon}}$  and  $\underline{\underline{\sigma}}$  are written as 6-dimensional vectors according to the following rule:

$$11 \rightarrow 1, 22 \rightarrow 2, 33 \rightarrow 3, 23 \rightarrow 4, 31 \rightarrow 5, 12 \rightarrow 6. \quad (2.27)$$

The tensor  $C_{ijkl}$  is transformed into  $C_{KL}$  by applying the same index conversion. Hooke's law is then written as

$$\sigma_K = C_{KL}\epsilon_L \quad (2.28)$$

It is important to note that neither the vectors  $\epsilon_K, \sigma_K$  nor the matrix  $C_{KL}$  behave like tensors under transformations of coordinates. The tensor  $C_{ijkl} = C_{KL}$  contains all elastic material properties; in tables, values are always given in terms of  $C_{KL}$ . We will make use of this notation in chapter 6.

In the following, we will mainly consider isotropic materials. The assumption of isotropy is especially well fulfilled in polycrystalline materials, where the crystallites are oriented randomly and the extend of the structures is large in comparison to the crystallites, and for amorphous materials like glasses. While for isotropic materials, there are only two independent constants in  $C_{ijkl}$ , there are, unfortunately, various equivalent ways to choose them, all of which are frequently encountered in the literature.

One commonly used way is to define them as

$$C_{1122} =: \lambda, \quad C_{1212} = \frac{1}{2}(C_{1111} - C_{1122}) =: \mu, \quad C_{1111} = \lambda + 2\mu. \quad (2.29)$$

$\lambda$  is called LAMÉ-constant and  $\mu$  is the SHEAR MODULUS (sometimes also denoted with  $G$ ). Hooke's law written in these terms becomes:

$$\sigma_{ij} = \lambda\delta_{ij}\epsilon_{ll} + 2\mu\epsilon_{ij} \quad (2.30)$$

and the inverse relation is

$$\epsilon_{ij} = \frac{-\lambda}{2\mu(3\lambda + 2\mu)}\sigma_{ll}\delta_{ij} + \frac{1}{2\mu}\sigma_{ij} \quad (2.31)$$

respectively.

The other commonly used technical constants have their origin in simple loading situations. From the situation of a pure pull comes the choice of writing Hooke's law in terms of the YOUNG'S MODULUS  $E$  and the POISSON NUMBER  $\nu$ . If a long small rod is pulled in  $x$ -direction, all stresses except for  $\sigma_{xx}$  vanish, and we obtain

$$\sigma_{xx} = \frac{\mu(3\lambda + 2\mu)}{\lambda + \mu}\epsilon_{xx} \equiv E\epsilon_{xx} \quad (2.32)$$

$$\epsilon_{yy} = \epsilon_{zz} = \frac{-\lambda}{2\mu(3\lambda + 2\mu)}\sigma_{xx} \quad (2.33)$$

$$\epsilon_{xy} = \epsilon_{yx} = \dots = 0, \quad (2.34)$$



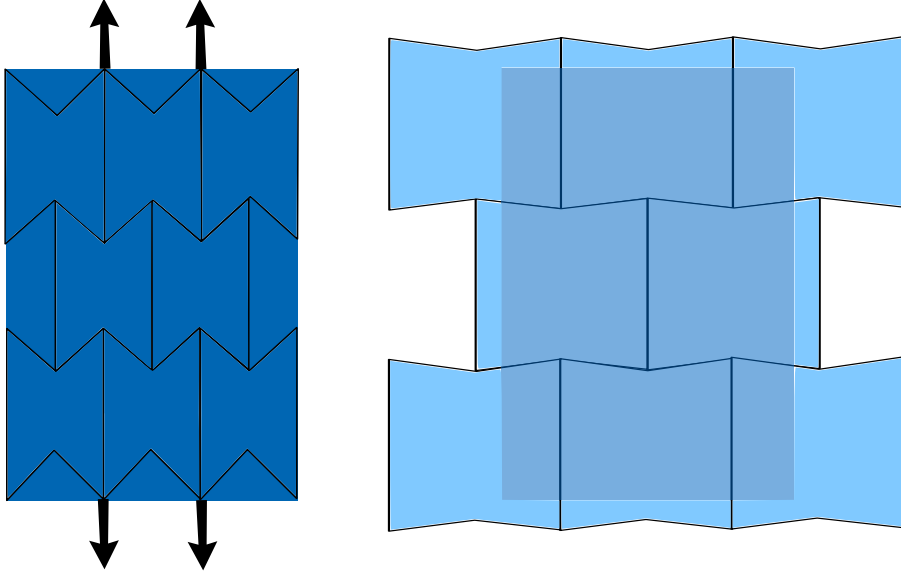


Figure 2.2.: Schematics of the microstructure of an auxetic material. If tensile external loading is applied, the material expands laterally, which corresponds to a negative Poisson ratio.

so we can define the Young's modulus  $E$  and the Poisson number  $\nu$  as

$$E = \frac{\sigma_{xx}}{\epsilon_{xx}} = \frac{\mu(3\lambda + 2\mu)}{\lambda + \mu} \quad (2.35)$$

$$\nu = -\frac{\epsilon_{yy}}{\epsilon_{xx}} = \frac{\lambda}{2(\lambda + \mu)}. \quad (2.36)$$

The Young's modulus  $E$  describes the relation between stress and dilatation and the Poisson number  $\nu$  the ratio of the dilatation and the contraction perpendicular to the direction of the pull.  $E$  is always strictly positive, and values for  $\nu$  have to fall in the range of  $-1 < \nu < 1/2$ . In most metals,  $\nu$  has a value between  $1/4$  and  $1/3$ ; rubber has a Poisson number close to  $0.5$ , making it almost incompressible. On the other hand, cork has a Poisson ratio close to zero, making it very suitable as a bottle stopper, since it does not expand laterally during the uniaxial compression when it is inserted into or pulled out of the bottle. Materials with negative Poisson ratio, which become thicker perpendicularly to the applied force, are called AUXETICS, see Fig. 2.2. For foam structures, even negative poisson ratios up to  $-0.8$  have been observed experimentally [72]. Hooke's law written in this representation has the form

$$\sigma_{ij} = \frac{E}{1 + \nu} \left( \epsilon_{ij} + \frac{\nu}{1 - 2\nu} \delta_{ij} \epsilon_{kk} \right) \quad (2.37)$$

and the inverse relation reads

$$\epsilon_{ij} = \frac{-\nu}{E} \delta_{ij} \sigma_{kk} + \frac{1 + \nu}{E} \sigma_{ij}. \quad (2.38)$$

	$\mu, \lambda$	$K, \mu$	$E, \nu$
$\mu$	$\mu$	$\mu$	$\frac{E}{2(1+\nu)}$
$\lambda$	$\lambda$	$K - \frac{2\mu}{3}$	$\frac{\nu E}{(1+\nu)(1-2\nu)}$
$K$	$\lambda + \frac{2\mu}{3}$	$K$	$\frac{E}{3(1-2\nu)}$
$E$	$\frac{\mu(3\lambda+2\mu)}{\lambda+\mu}$	$\frac{9K\mu}{3K+\mu}$	$E$
$\nu$	$\frac{\lambda}{2(\lambda+\mu)}$	$\frac{3K-2\mu}{2(3K+\mu)}$	$\nu$

Table 2.1.: Conversion rules for commonly used elastic constants

One advantage of using  $E$  and  $\nu$  lies in the fact that  $\nu$  is a dimensionless number, a property that will be particularly exploited in chapter 6 in the context of effective medium theories.

Another common choice consists of writing down Hooke's law in terms of a COMPRESSION MODULUS  $K$  and a TORSION or SHEAR MODULUS  $\mu$ , since the forces leading to compression with volume change and the forces leading to a torsion without volume change are different (see Eq. (2.11)). Since we assume a linear relationship between stress and strain, it seems reasonable to introduce two independent elastic constants that correspond to the two different required forces. By this decomposition, one obtains

$$\sigma_{ij} = K\delta_{ij}\epsilon_{kk} + 2\mu\left(\epsilon_{ij} - \frac{1}{3}\delta_{ij}\epsilon_{kk}\right) \quad (2.39)$$

for Hooke's law.

The elastic energy density for an isotropic medium is therefore given by

$$U = \frac{1}{2}\sigma_{ij}\epsilon_{ij} \quad (2.40)$$

$$= \frac{E}{2(1+\nu)}\left(\epsilon_{ij}^2 + \frac{\nu}{1-2\nu}\delta_{ij}\epsilon_{kk}^2\right) \quad (2.41)$$

There is no general rule for which set of elastic constants should be used; rather, the loading situation or other considerations determine the most convenient choice. For quick reference, all the relations between the technical constants used in this thesis are given in Tab. 2.1.

The constants  $K$ ,  $\lambda$ ,  $\mu$ ,  $E$  all have the same unit, which is PRESSURE. Only the Poisson ratio  $\nu$ , defined as the ratio of lateral and axial strain, is a dimensionless quantity.

### 2.1.6. Plane Strain Loading

One very important loading situation that we will use frequently is called PLANE STRAIN and it effectively reduces an original three-dimensional problem to two dimensions. A

body is said to be in plane strain parallel to the  $xz$  plane if the perpendicular displacement component vanishes,  $u_y = 0$ , and the other two components  $u_x$  and  $u_z$  depend only on  $x$  and  $z$ . The plane strain situation is therefore defined by

$$\begin{aligned} u_y &= 0 \\ u_x &= u_x(x, z), \quad u_z = u_z(x, z) \\ \epsilon_{xy} &= \epsilon_{yz} = \epsilon_{yy} = 0, \end{aligned} \quad (2.42)$$

which implies

$$\begin{aligned} \sigma_{xy} &= \sigma_{yx} = \sigma_{yz} = \sigma_{zy} = 0 \\ \sigma_{yy} &= \nu(\sigma_{xx} + \sigma_{zz}). \end{aligned} \quad (2.43)$$

The corresponding strains can be obtained by the inverted version of Hooke's law Eq. (2.38) and read

$$\epsilon_{xx} = \frac{1}{E} \left( (1 - \nu^2)\sigma_{xx} - \nu(1 + \nu)\sigma_{zz} \right) \quad (2.44)$$

$$\epsilon_{xz} = \frac{1 + \nu}{E} \sigma_{xz} \quad (2.45)$$

$$\epsilon_{zz} = \frac{1}{E} \left( (1 - \nu^2)\sigma_{zz} - \nu(1 + \nu)\sigma_{xx} \right). \quad (2.46)$$

One of the main problems in solving elastic problems is that we are required to solve up to six coupled partial differential equations. The AIRY STRESS FUNCTION [73] reduces the coupled partial differential equations to a single partial differential equation for a scalar valued function from which later stresses and strains can be deduced. This is not possible for general three dimensional problems, but in the special case of plane stress or plane strain problems: If no volume forces act on the body, Newton's equation provides us with the equilibrium condition Eq. (2.21). This condition is equivalent to the statement that the stresses can be derived from a generalized potential  $U$ , the Airy Function,

$$\sigma_{xx} = \frac{\partial^2 U}{\partial z^2}, \quad \sigma_{xz} = -\frac{\partial^2 U}{\partial x \partial z}, \quad \sigma_{zz} = \frac{\partial^2 U}{\partial x^2}. \quad (2.47)$$

for which the Saint-Venant compatibility condition Eq. (2.10) leads to the biharmonic equation

$$\Delta \Delta U = \frac{\partial^4 U}{\partial x^4} + 2 \frac{\partial^4 U}{\partial x^2 \partial z^2} + \frac{\partial^4 U}{\partial z^4} = 0. \quad (2.48)$$

We will only treat plane strain cases since the plane stress case can be deduced simply by altering the value of the Poisson ratio of the material. This concludes our introduction of linear theory of elasticity.

## 2.2. Continuum Fracture Mechanics

The dynamics of fast fracture processes are still posing a great challenge to both experimental and theoretical physics. One of the reasons is that very different scales are coupled:

by cracking, the material releases the stored large scale elastic energy, but processes at the vicinity of the moving crack tip determine energy dissipation and stress conditions. These processes finally determine the crack shape, speed and its direction. The exact processes at the crack tip are extremely complicated, largely unknown and strongly dependent on the material [50]; they range from rupture and disentangling of intertwined polymer strands in amorphous polymers to dislocation formation, emission of acoustic waves and fracture in crystalline materials, and there are typically no first principle descriptions available. But whatever the process: for a single moving crack, the crack tip provides the only energy sink in the system [37, 61].

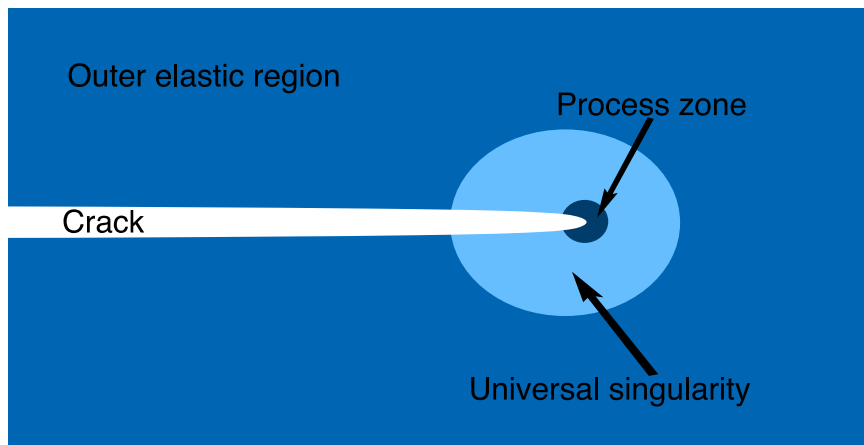


Figure 2.3.: The three regions around the tip of a propagating crack.

By a proposition of Irwin and Orowan [58, 88], the medium around a crack can be divided in three regions.

- All microscopic details (of how the material actually breaks) are lumped together and hidden in a **PROCESS ZONE**. Then, the crack tip behavior is only described via a phenomenological fracture energy release rate  $\Gamma$ , which is the energy needed to form one unit area of fracture surface.
- In the region just outside the process zone, called the **UNIVERSAL ELASTIC REGION**, the stress and strain fields have a universal singular form which depends only on the symmetry of the applied external loading. This singular form is given by the so-called **STRESS INTENSITY FACTORS**.
- Everywhere outside the process zone, the material behaves according to continuum linear theory of elasticity. In the region far from the tip, called the **OUTER ELASTIC REGION**, the elastic fields just depend on the shape of the body and on location and strength of the external loading. In special cases, even analytical solutions are available.

The size of both the process zone and the universal elastic region depends on numerous factors like the form and the propagation velocity of the crack, the loading and also the

material. For brittle materials, the process zone is in the nanometer range, while for ductile materials like steel, it can be of the order of several micrometer [37].

This macroscopic description, where linear elasticity is valid almost everywhere except for the very crack tip is sometimes also called SMALL-SCALE YIELDING.

### 2.2.1. Modes of External Loading

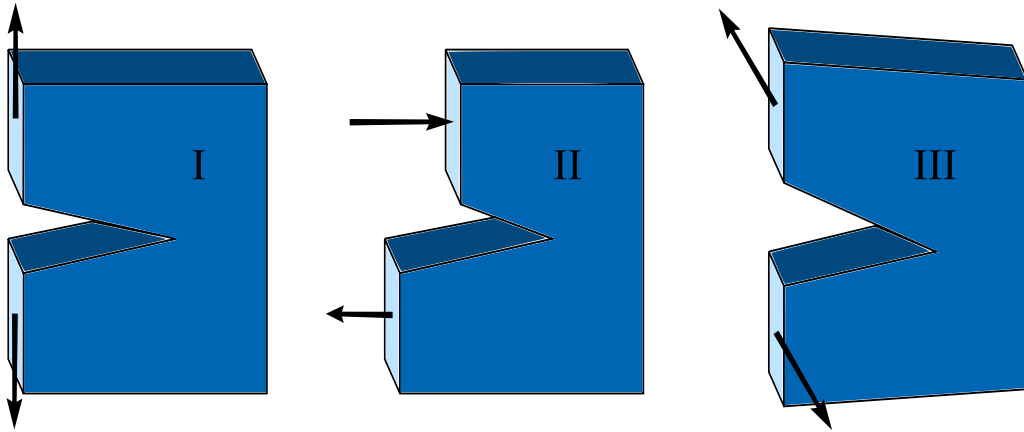


Figure 2.4.: The different crackmodes

There are three different modes of loading, depicted in Fig. 2.4, which are usually referred to simply by Roman literals I, II and III. Mode I is sometimes also called *OPENING MODE*, mode II is called *IN-PLANE shear mode* and mode III is named *OUT-OF-PLANE shear mode* or *TEARING MODE*. It turns out that the crack-tip stress equations are very similar for each of the modes, their format being exactly the same. Consequently, the fracture and crack growth analysis for each of the modes are identical, only the occurring numerical prefactors differ. If one knows how to deal with mode I, one knows essentially how to analyse modes II and III.

Additionally, by far the majority of cracks result from mode I loading. Practice has shown that in the cases of mixed mode loading, the cracks prefer to choose a direction of growth in which they are subjected to mode I [54]. Experimentally, it is easiest to control mode I loading, since the surfaces of mode II and III are not pulled away from each other, and contact of the surfaces is unavoidable [36]. This additional friction affects the crack, but quantitative assessment of this influence is hard to obtain. This is the reason why we concentrate primarily on mode I cracks in this thesis. One should note, however, that a true mixed mode analysis can be more difficult analytically and numerically and can also lead to physically different phenomena [107].

### 2.2.2. The Griffith-Criterion: Scaling Analysis

In the 1920s, Griffith formulated the idea that is commonly acknowledged as the start of equilibrium fracture mechanics as a quantitative science of material behavior. He recognized that the macroscopic potential energy of a system, consisting of the internal stored elastic energy and the external potential energy of the applied loads, varies with the size of the crack. By a propagating crack, the elastically stressed material around the crack relaxes. He also realized that by advancing of the crack, work needs to be done to create the two crack surfaces. If the elastic energy decrease is larger than the energy needed to form new crack surfaces, the material breaks. Fracture mechanics then consists of writing down the appropriate energy balance for the motion of the crack. This kind of scaling argument is based on a quasi-static approximation, where the cracks propagate only slowly and the kinetic energy of the material that is moved out of the way by opening the crack is neglected, but it is still useful to illustrate the general strategy.

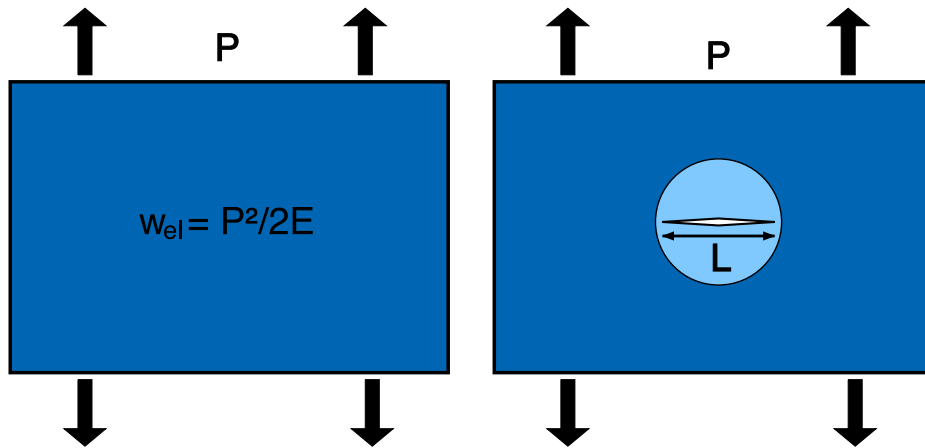


Figure 2.5.: A crack of length  $L$  reduces the elastic energy stored in a solid with elastic modulus  $E$  that is subjected to an external loading  $P$ .

A simple scaling analysis highlights this idea: if an external loading  $P$  is applied to an infinite two-dimensional isotropic homogeneous solid, the elastic energy density stored in the material is

$$w_{el} \sim \frac{P^2}{E}, \quad (2.49)$$

with  $E$  being the elastic modulus. Comparing this situation with a solid that contains a (static) crack of length  $L$ , we see that the crack opening leads to a reduction of elastic energy in the area  $A \sim L^2$  of

$$W_{el} \sim w_{el}A \sim \frac{P^2 L^2}{E}, \quad (2.50)$$

see Fig. 2.2.2.

The increase of surface energy scales of course linearly with the crack length,

$$W_s \sim \gamma L \quad (2.51)$$

## 2.2. CONTINUUM FRACTURE MECHANICS

---

where  $\gamma$  denotes the surface energy density. Thus, the total energy balance  $W = W_s - W_{el}$  has a linearly increasing, but quadratically decreasing term, meaning that for sufficiently long cracks, crack growth is energetically favorable, see Fig. 2.6. The critical length scales as

$$L_G \sim \frac{\gamma E}{P^2}, \quad (2.52)$$

Cracks that are longer than this critical value will continue to grow, shorter cracks shrink. Typically, shrinking does not occur since it is not possible due to other processes, like surface oxidation. The exact form for the Griffith length  $L_G$  depends also on the crack shape. Griffith's energy criterion is particularly attractive as it avoids the need to examine the actual process at the crack tip in detail.

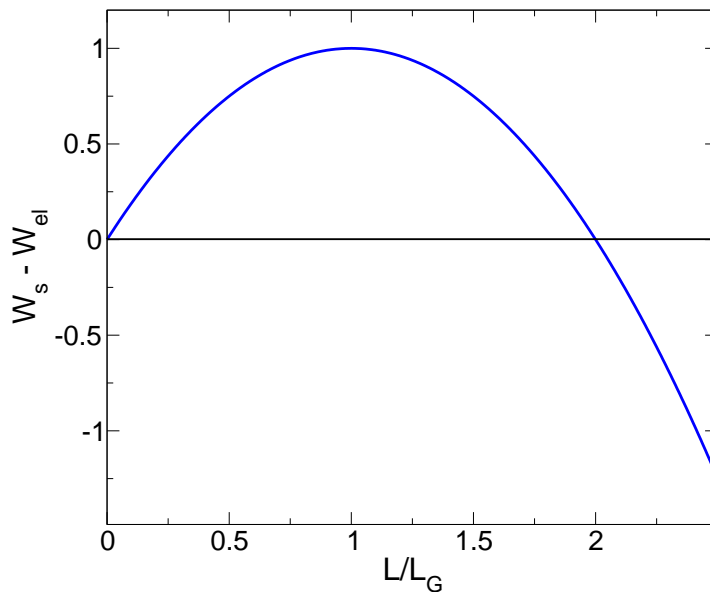


Figure 2.6.: The total energy of the cracked system has a maximum at the Griffith length  $L_G$ . Cracks that are longer will grow, providing an efficient mechanism to reduce the total energy of the system.

The simplest linear response law one can assume for the crack length is

$$\frac{dL}{dt} = -D \frac{dW}{dL}, \quad (2.53)$$

which already shows a serious problem: for an infinite solid, the crack continues to accelerate and reaches arbitrarily large velocities after a finite time. It turns out that static linear theory of elasticity does not provide a selection mechanism for the tip propagation velocity that could serve as a cutoff. This also implies that a steady growth regime with constant tip velocity is not possible in the quasistatic approximation.

### 2.2.3. Near-Tip Behavior: The Square Root Singularity

The problem of both static and propagating cracks has been tackled with various analytical approaches. One of the most important results is that the stress field surrounding the crack tip exhibits a square root singularity for all cases that can be worked out explicitly, independent of the loading mode [61, 37, 36]. With the crack line corresponding to  $\theta = 0$ , the stress field  $\sigma$  at the crack tip, measured in polar coordinates, takes the form

$$\sigma_{ij} = \frac{K_m}{\sqrt{2\pi r}} f_{ij}^m(v, \theta), \quad (2.54)$$

with the stress intensity factor  $K$ ,  $m$  an index indicating the loading mode I-III,  $(r, \theta)$  giving the location in polar coordinates and  $v$  the tip velocity. Eq. (2.54) has two important implications: first, for arbitrary loading configurations, the resulting stress field at the tip can be decomposed into the linear combinations of the pure loading mode stress fields with three stress intensity factors  $K_m$ .

The second implication is that a single scalar quantity, the STRESS INTENSITY FACTOR, contains all detailed information about the samples history and present loading situation. This factor is of course determined by the elastic fields in the entire medium, but the stress present at the very crack tip is ultimately the local quantity that drives the crack. This means that for two systems with the same stress intensity factor, the crack will behave the same way, regardless of loading history or other external conditions.

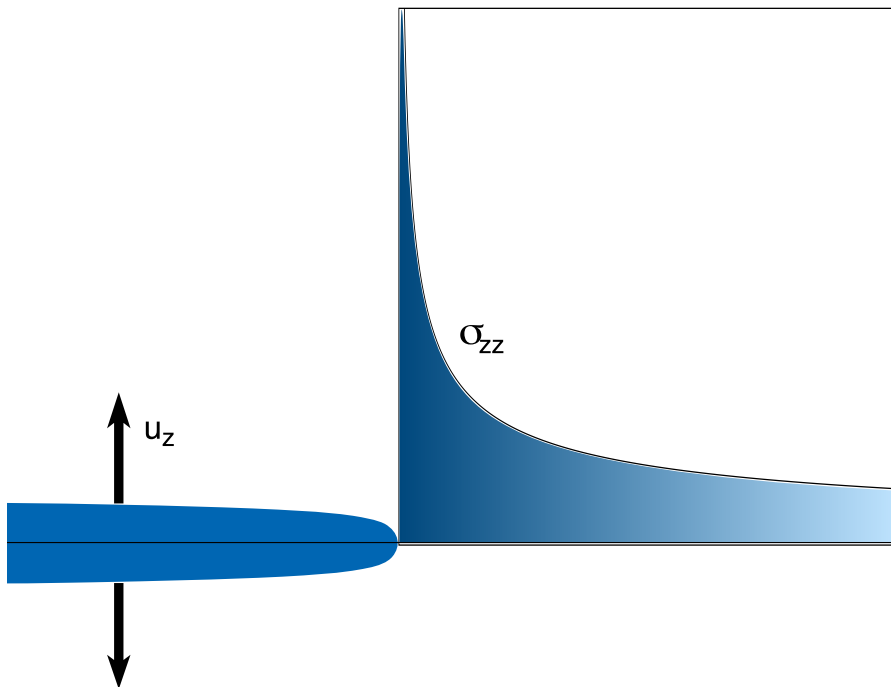


Figure 2.7.: The stresses display a singular behavior at the crack tip.

Since crack propagation is a mechanism to dissipate elastic energy stored in the system, the crack tip's behavior must be influenced by the energy flowing into it. The energy



release rate  $G$  is given by

$$G = \frac{1 - \nu^2}{E} A_m(v) K_m^2 \quad (2.55)$$

with the Poisson ratio  $\nu$ , the elastic modulus  $E$ ,  $m$  denoting the crack loading modes, and  $A_m(v)$  three functions that depend only on the crack velocity and the corresponding stress intensity factors  $K_m$ . The energy release rate  $G$  is defined as the quantity of energy flowing into the crack per unit fracture surface formed. Because of the universal form of the stress intensity factor, it is possible to describe the crack tip behavior with macroscopic quantities, even though the analysis is only carried out within the universal elastic region.

Still, the square root singularity provides a fundamental problem for all macroscopic models that assume sharp tips, since the stresses at the crack tip diverge. Therefore, a mechanism that regularizes the fields around the crack tip is needed. While it is also conceivable that plastic processes can play an important role for the crack tip behavior, it is a different and much disputed matter how to model these processes. There have been attempts by Falk and Langer [33] that have later been extended by Procaccia et al. [12]. The idea is that plastic deformations tame the stress fields near the tip and remain close to the yield stress of the material. With these velocity-dependent plastic terms, a scale selection is possible. Since this approach yields also “apparently unphysical” solutions and the numerical solution based on quasistatic linear elasticity violates compatibility, the authors point out that their model cannot be seen as the final theory of viscoplasticity. Because their model still lacks a rigorous coupling to elasticity and a consistent description of the crack wake, they emphasize the importance of treating of the crack as a free moving boundary problem.

#### 2.2.4. Dynamic Effects

As we pointed out in section 2.2.2, static theory of elasticity does not provide an upper limit for the propagation velocity of cracks. It is conceivable that, if the processes are very fast, inertial effects have to be taken into account. Therefore, we go beyond the quasistatic approximation by using the fully dynamic version of Newton’s law as given in Eq. (2.20), but neglect external volume forces:

$$\frac{\partial \sigma_{ij}}{\partial x_j} = \rho \frac{\partial^2 u_i}{\partial t^2} \quad (2.56)$$

with the mass density  $\rho$ . With the knowledge of the previous section, we can make an estimate of the scale at which kinetic effects become relevant. The square root singularity states that at a distance  $r$  from the tip of a crack that propagates with velocity  $v$ , stresses scale like

$$\sigma_{ij} \sim \frac{K}{\sqrt{r}} \quad (2.57)$$

and the corresponding displacements like

$$u_i \sim \frac{K\sqrt{r}}{E}. \quad (2.58)$$

Therefore, the scale of the characteristic accelerations is

$$\frac{\partial^2 u_i}{\partial t^2} \sim \frac{Kv^2}{Er^{3/2}}. \quad (2.59)$$

Comparing both sides of Eq. (2.56), we see that the right hand side becomes comparable to the left hand side if the velocity is of the order of

$$v_R \sim \sqrt{\frac{E}{\rho}}. \quad (2.60)$$

In fact, expressing the stresses in Eq. (2.56) with strains and plugging in the definition of the strain tensor Eq. (2.9), we obtain for an isotropic material [73]

$$\rho \frac{\partial^2 u_i}{\partial t^2} = \frac{E}{2(1+\nu)} \frac{\partial^2 u_i}{\partial x_j^2} + \frac{E}{2(1+\nu)(1-2\nu)} \frac{\partial^2 x_k}{\partial x_i \partial x_k} \quad (2.61)$$

Assuming that the deformation  $\underline{u}$  in an infinite system depends only on one coordinate,  $x$ , and on time, then all derivatives with regard to the other two directions vanish, and we obtain the well known wave equations

$$\frac{\partial^2 u_x}{\partial x^2} = \frac{1}{c_d} \frac{\partial^2 u_x}{\partial t^2} \quad (2.62)$$

$$\frac{\partial^2 u_y}{\partial x^2} = \frac{1}{c_s} \frac{\partial^2 u_y}{\partial t^2} \quad (2.63)$$

$$\frac{\partial^2 u_z}{\partial x^2} = \frac{1}{c_s} \frac{\partial^2 u_z}{\partial t^2} \quad (2.64)$$

$$(2.65)$$

with the DILATATIONAL wave speed  $c_d$  and the SHEAR wave speed  $c_s$  given by

$$c_d = \sqrt{\frac{E(1-\nu)}{(1+\nu)(1-2\nu)\rho}} \quad (2.66)$$

$$c_s = \sqrt{\frac{E}{2(1+\nu)\rho}} \quad (2.67)$$

The wave speeds define the maximal speed at which information about the elastic state of a body can travel through the system. A more careful analysis [113] reveals that the maximal speed at which a crack can propagate is given by the RAYLEIGH SPEED  $v_R$ , which is the speed at which sound waves travel along a free surface. The Rayleigh speed cannot be expressed in closed form, but a good approximation is given by [37]

$$v_R \approx c_s \frac{0.862 + 1.14\nu}{1 + \nu}. \quad (2.68)$$

The wave speeds always fulfill the hierarchy relation  $v_R < c_s < c_d$ . The upshot of these considerations is that the maximal velocity at which a crack can propagate in a material is given by the Rayleigh speed, which is a quantity that depends only on the material parameters  $E$ ,  $\nu$  and the density  $\rho$ . Therefore, the Rayleigh speed is a central quantity in fracture theory.

## 2.3. Transport Mechanisms

The classical continuum theories [37] of crack propagation are based on an integral energy balance criterion and on linear theory of elasticity, see sec. 2.1, in the vicinity of an infinitely sharp crack tip. However, if the displacement is large, cracks cease to resemble mathematical cuts, having “blunt” tips and a considerable opening in their further run. Including a finite curvature of the crack tip as a relevant dynamical variable could avoid the stress singularities. But in order to describe cracks with a finite tip radius and opening with a continuum theory, a mass transport mechanism is necessary. We will focus on two different possible processes, the first one being SURFACE DIFFUSION, the second being a PHASE TRANSFORMATION process.

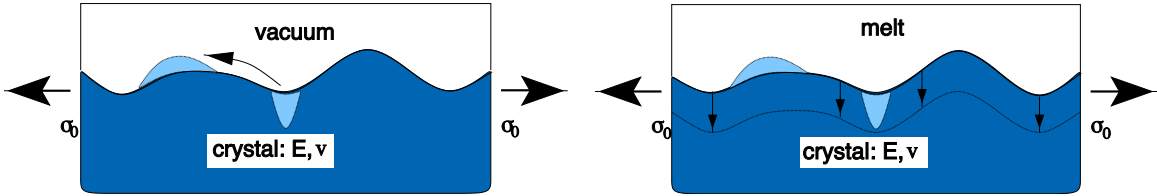


Figure 2.8.: Schematics of the morphological surface changes under stress. Left: the shape change is driven by surface diffusion processes, which obey material conservation. Right: The shape change is driven by phase transition processes (melting and crystallisation). The four arrows and the dashed line indicate the surface at a later time.

Surface diffusion was always considered the important mass transport process in the context of movement of liquid filled pores and voids [57, 29] and thin film deposition. Soon, the connection to interface dynamics in the presence of elastic stresses has been made, now known as the Asaro-Tiller-Grinfeld instability [3, 43], which we will discuss in section 2.4. Being well understood in the context of interfacial pattern formation, the possible relevance of surface diffusion processes for crack propagation been investigated later [118, 115, 16]. Assigning a chemical potential  $\mu$  to each phase, nonhydrostatic stresses lead to a surface flux proportional to the gradient of  $\mu$  along the interface. Since the material is conserved, the normal velocity at each point of the interface equals the divergence of this flux,

$$v_n = M_s \Delta_s \mu = M_s \frac{\partial^2 \mu}{\partial s^2}, \quad (2.69)$$

where  $M_s$  is a mobility coefficient, and  $\Delta_s$  is the Laplace-Beltrami operator on the surface.

At first, it seems to be counterintuitive that any fast interface propagation could be due to surface diffusion, since this process is normally considered to be relatively slow. This is of course true for flat interfaces in equilibrium, where the energetic barrier to remove particles from the bulk is extremely high. However, the processes we are considering differ notably: the surface is already corrugated, lowering the energetic barrier. Also, it is known that the temperature fast propagating points and crack tips is very high, often close to the melting temperature. This heat is then transported by convection away from the tip towards the tail region. Since the particles have to be moved only over very small

distances, typically some atomic spacings, it can be concluded that for small tips, the surface diffusion process can be sufficiently fast [16].

Another possible process for interface propagation is a first order phase transition, like evaporation-condensation or melting-crystallisation. One phase serves as a particle reservoir for the other, and the normal velocity  $v_n$  is proportional to the difference of the chemical potential in each phase [67]:

$$v_n = -k_p \mu, \quad (2.70)$$

where  $k_p$  denotes a kinetic coefficient that is dimensionally different to the mobility coefficient  $M_s$ . This mechanism is typically encountered in pattern formation processes driven by temperature, like the growth of snowflakes, of solid dendrites in metallic melts and of melt fingers in overheated solids. It also occurs in solid-solid transformations, where elastic stresses can drive a change in the crystal structure of the material. In contrast to surface diffusion, where the amount of material of each phase is conserved, this is not the case for phase transformation.

We want to emphasize that neither the word "diffusion" nor "evaporation" should be taken too literally. As we already emphasized in section 2.2, the physics in the small process zone around a crack tip is largely unknown. Many processes may play a role, including plastic flow. While plastic deformations could be relevant at the tip, dynamical theories of plasticity still lack the same general verification as linear theory of elasticity. If the active zone is sufficiently small, all processes can be modeled *effectively* by surface diffusion or even a melting process in the sense of a lubrication approximation. Hence, all details about the actual physical processes can be hidden in the effective surface coefficient to obtain well defined, effective macroscopic equations of motion for the interface.

We want to emphasize that the models we will present in the later sections are based solely on the *dynamical theory of elasticity* and the two different mass transport mechanisms mentioned in this section, namely surface diffusion and phase transformation.

## 2.4. Asaro-Tiller-Grinfeld-Instability

The Asaro-Tiller-Grinfeld-Instability sets in when a body with an originally flat interface is subjected to nonhydrostatic loading. If the elastic energy put into the body is big enough, it is preferable to form corrugations with a wave length  $\omega$  larger than a critical wave length, which *increases* the surface energy, but decreases the elastic energy. The maximally unstable mode depends weakly on the material transport mechanism, like surface diffusion or evaporation/condensation and the mode of loading [7]. This unstable behavior was first reported by Asaro and Tiller [3] and Grinfeld [43] and has also been confirmed experimentally [8].

### 2.4.1. Interface Kinetics

In this section, we will give some quantitative results about the interface dynamics in the early stage of the Grinfeld instability. The motion of the interface is locally driven by a chemical potential  $\mu$  at the surface, which ultimately leads to an advancement of the

interface by either phase transformation processes or redistribution of matter in the case of surface diffusion. Since surface energy does not couple to elastic terms, the chemical potential has two parts:

$$\mu = \mu_s + \mu_{el}, \quad (2.71)$$

where the surface energy contributes the term

$$\mu_s = -\frac{\gamma\kappa}{\rho_s}, \quad (2.72)$$

with the surface energy density  $\gamma$ , the curvature  $\kappa$  and the particle density  $\rho_s$ . The elastic energy density given by

$$w_{el} = \frac{1}{2}\sigma_{ij}\epsilon_{ij} \quad (2.73)$$

We consider a uniaxially strained system, see Fig. 2.4.1, which corresponds to a plane strain situation, see sec. 2.1.6.

We assume the external loading to be in direction  $z$ , perpendicular to the interface normal vector  $x$ , leading to  $z = \tau$ ,  $x = n$ . The boundary conditions at the interface read  $\sigma_{nn} = \sigma_{n\tau} = 0$ , which leads to an elastic energy density of

$$w_{el} = \frac{1 - \nu^2}{2E}\sigma_{\tau\tau}^2 \quad (2.74)$$

at the surface. The chemical potential is then

$$\mu = \frac{1}{\rho_s} \left( \frac{1 - \nu^2}{2E}\sigma_{\tau\tau}^2 - \gamma\kappa \right). \quad (2.75)$$

We assume now that the surface is not flat but periodically perturbed, so it can be modeled as

$$x(z) = A_0 \sin(kz), \quad (2.76)$$

where  $A_0$  is the initial amplitude and the wave vector  $k$  is assumed to be positive. Starting from an Airy function (see Sec. 2.1.6)

$$U = \frac{\sigma_0 x^2}{2} + cx e^{kx} \sin(kz), \quad (2.77)$$

where the expansion coefficient  $c$  is comparable to the initial amplitude,  $c \sim A_0$ . From the Airy function, it is easy to obtain the stresses via

$$\sigma_{xx} = \frac{\partial^2 U}{\partial z^2}, \quad \sigma_{zz} = \frac{\partial^2 U}{\partial x^2}, \quad \sigma_{xz} = -\frac{\partial^2 U}{\partial z \partial x}. \quad (2.78)$$

The transformation to the appropriate local coordinate system with normal  $n$  and tangential  $\tau$  is done by a rotation of the cartesian system by the angle  $\theta = \arctan x'(z)$ . The first order expansion in the initial amplitude  $A_0$  provides us with the stress relations

$$\sigma_{nn} = 0 \quad (2.79)$$

$$\sigma_{n\tau} = -(A_0\sigma_0 + c)k \cos(kz) \quad (2.80)$$

$$\sigma_{\tau\tau} = \sigma_0 + ck(2 + kx)e^{kx} \sin(kz), \quad (2.81)$$

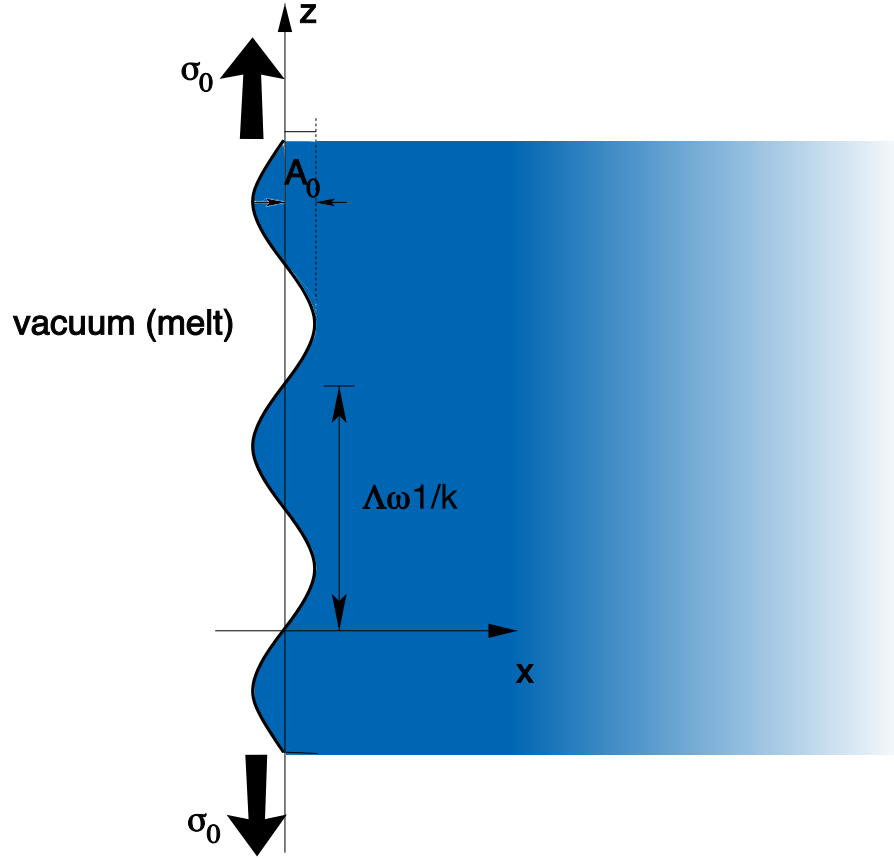


Figure 2.9.: A solid with an initially flat interface at  $x(z) = 0$  has a sinusoidal perturbation. The amplitude can grow or shrink, depending on the strength of the loading  $\sigma_0$ .

Vanishing normal and shear stresses impose the condition

$$c = -A_0\sigma_0 ; \quad (2.82)$$

which, after inserting the interface function Eq.(2.76), leads to the tangential stresses

$$\sigma_{\tau\tau} = \sigma_0 - 2A_0\sigma_0k \sin(kz) \quad (2.83)$$

at the interface. The resulting chemical potential is therefore given by

$$\mu = A_0 \left( \frac{-2(1-\nu^2)}{E} \sigma_0^2 k + \gamma k^2 \right) \sin(kz) \quad (2.84)$$

Depending on the underlying transport mechanism, the dynamic evolution of the interface differs. If the underlying transport mechanism is supposed to be *surface diffusion*, the equation of motion eq. (2.86) reads

$$\frac{\partial x}{\partial t} = M_s \frac{\partial^2 \mu}{\partial z^2} = \frac{M\rho_s}{\gamma} \frac{\partial^2 \mu}{\partial z^2} . \quad (2.85)$$

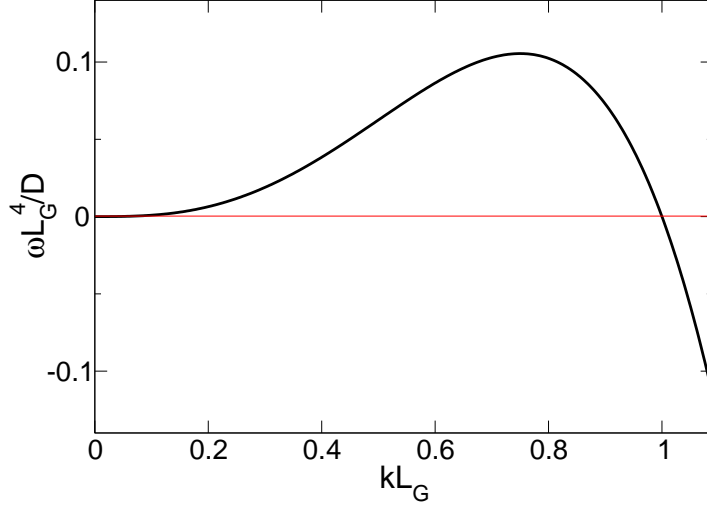


Figure 2.10.: Spectrum of the Grinfeld instability for surface diffusion. Long wave perturbations are unstable.

In the case of a phase transformation process, discussed in detail in chapter 5, the local normal interface velocity is directly proportional to the chemical potential, and Eq. (2.85) is replaced by

$$\frac{\partial x}{\partial t} = \frac{D\rho_s}{\gamma}\mu \quad (2.86)$$

with a kinetic coefficient  $D$ .

The time evolution of the perturbation's amplitude is given by

$$A(t) = A_0 e^{\omega t} \quad (2.87)$$

Depending on which transport process is assumed,  $\omega$  has either the form

$$\omega_s = Mk^2 \left( \frac{2(1-\nu^2)}{E\gamma} \sigma_0^2 k - k^2 \right) \quad (2.88)$$

in the case of surface diffusion, or

$$\omega_p = D \left( \frac{2(1-\nu^2)}{E\gamma} \sigma_0^2 k - k^2 \right) \quad (2.89)$$

for phase transformation kinetics. Introducing the Grinfeld length

$$L_G = \frac{E\gamma}{2(1-\nu^2)\sigma_0^2}, \quad (2.90)$$

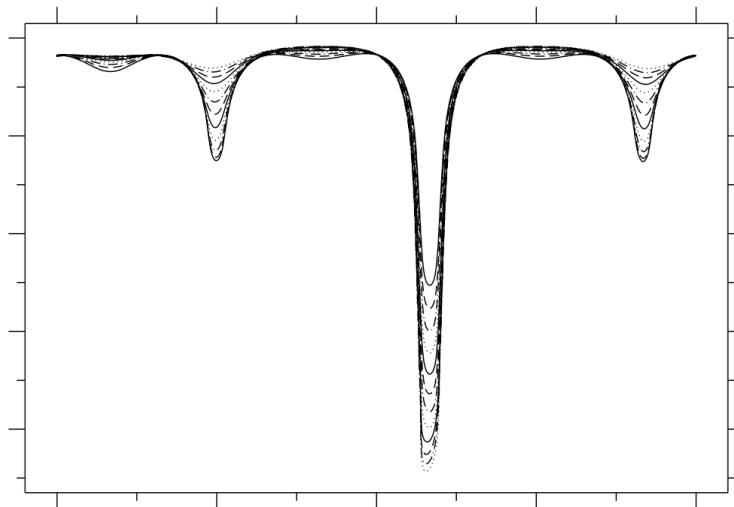


Figure 2.11.: Formation of deep grooves in the late stage of the Grinfeld instability [69]. The different interface profiles correspond to different times. In the framework of static elasticity, the tip radius of the winning groove approaches zero while the propagation velocity diverges after a finite time.

we can express the spectrum as

$$\omega_s L_G^4 / M_s = (kL_G)^3 (1 - kL_G) \quad (2.91)$$

$$\omega_p L_G^4 / k_p = (kL_G)(1 - kL_G) . \quad (2.92)$$

The spectrum for surface diffusion is plotted in Fig. 2.10. We see that short-wave perturbations are suppressed by the surface energy, but long wave distortions lead to an unstable surface. Note that the scaling behavior is identical to that of the Griffith length, see Eq. (2.52), which constitutes the deeper link between the Grinfeld instability and fracture mechanics.

### 2.4.2. The Time Cusp Singularity

This analysis is of course only correct in the quasi-static case of slow interface velocities, since the time-dependence of the elastic problem is not included. The long-time behavior of the Grinfeld instability shows an interesting feature: leaving the validity regime of the linear stability analysis of a planar interface subjected to nonhydrostatic stress, one finds that by long-wave perturbations with a wave-length larger than a critical value, deep grooves, similar to cracks, can form in time, see e.g. [117, 67, 69]. The different grooves compete with each other in advancing, and the winner's tip can advance with considerable speed. These propagating notches look and behave very much like cracks, which lead to the idea that crack propagation can be studied with the macroscopic equations that are well established in pattern formation processes [67]. However, it turns out that in the



framework of static elasticity, the propagation velocity increases to infinity and the tip radius goes to zero, leading to a breakdown of the theory. Therefore, any attempt to describe a steady state growth of the crack-like notches is impossible, and the system collapses into the so-called finite time cusp singularity of the Grinfeld instability.

## 2.5. The Phase-Field Method

Treating cracks in the spirit of a pattern formation approach poses the challenge of solving a free moving boundary problem. The motion of an interface is driven by external fields, but the fields themselves are affected by the a priori unknown and evolving interface. In the so called sharp-interface approach, the respective partial differential equations describing the bulk behavior have to be solved. The surfaces are treated as those evolving points in space and time that satisfy certain, different boundary conditions (e.g. the normal velocity of a moving front can be proportional to the jump in the gradient of the temperature field), which necessitates tracking the interface at each time step.

The general idea of the phase-field method is to avoid explicit interface tracking by introducing a so called PHASE-FIELD  $\phi$  instead; this phase-field encodes to which phase a given point at a given time belongs, similar to an order parameter. In the simplest case of a two-phase material, which can consist for example of a hard and a soft solid phase, the value  $\phi = 1$  is assigned to the hard and  $\phi = 0$  to the soft phase. The explicit treatment of the interfaces can then be avoided by “smearing out” the transition between the phases on a small numerical length scale  $\xi$  instead of a sharp discontinuous jump from  $\phi = 0$  to  $\phi = 1$ . The equations of motion for this phase-field contain a coupling to the physical fields which can be derived from an appropriate functional [91, 92]. Now, the motion of interfaces are effectively mapped to a partial differential equation for the phase field on the entire domain. In particular, the boundary conditions at the interfaces are automatically satisfied. This results in a self-consistent description of processes on different length and time scales via coupled partial differential equations.

A major field of application for the phase-field method are solidification problems, where diffuse-interface models were developed early on [74, 24], and they have seen renewed interest since computational power increased enough to render their simulation feasible. The concept was extended to anisotropic interface properties [78], and first qualitative numerical calculations of dendritic growth [70, 71] were followed by theoretical improvement of the asymptotics permitting quantitative simulations [64, 65], at least for intermediate to large undercoolings. Non-dendritic growth morphologies were also simulated, even in three dimensions [1]. Generalizations included the description of the coexistence of more than two phases [116, 38]. Additional examples of successful application of the tool phase field include the modeling of step-flow growth [94, 90] and of the elastically induced morphological instability [81, 68, 69, 63], often labeled Grinfeld [43] or Asaro-Tiller-Grinfeld instability [3]. Recently, it has also been making its way in other areas where the dynamics of interfaces are important, like biology, medicine [35] and computer graphics [9].

Since the information about the interface position is encoded implicitly in the phase-field, the method constitutes a special case of level-set approaches [89, 103]. It differs from the general case by having a level-set function that satisfies particular bulk equations of motion that renders the computation of an extension of the interface velocity to the bulk

unnecessary. This way, the interface does not need to be captured at each time step, which is normally required in level-set methods.

There is one important drawback in comparison with other level-set methods, however: the phase-field does not constitute an exact representation of the interface continuum problem, reducing to its dynamics only asymptotically, since the additionally introduced interface width  $\xi$  was not present in the original problem and introduces an additional lengthscale that has to be resolved [23, 31, 69]. The importance of this statement will accompany us for much of the remainder of the thesis.

### 2.5.1. Constructing a Phase-Field Model

We will explain the basic strategy in constructing a phase-field model with well defined sharp-interface equations for a simple model. We assume that we have a system consisting of two different phases, denoted with 1 and 2, separated by a possibly moving interface. A very general example is given by the chemical potential

$$\mu = -\frac{\gamma\kappa}{\rho_s} - \mu_{ext} \quad (2.93)$$

with surface energy density  $\gamma$ , curvature  $\kappa$  and some additional chemical potential  $\mu_{ext}$  that we do not specify further for the moment. The next ingredient of the sharp interface formulation is the relation for the local normal velocity  $v_n$  at each point:

$$v_n = \frac{D\rho_s}{\gamma}\mu \quad (2.94)$$

with some kinetic coefficient  $D$ . This interface velocity equation depends on the underlying physical transport process that is supposed to be modeled; in the case of surface diffusion, Eq. (2.94) is replaced by

$$v_n = \frac{M\rho_s}{\gamma}\Delta_s\mu \quad (2.95)$$

with a mobility  $M$  and the surface Laplacian operator  $\Delta_s$ .

The basic idea for solving the above interface equations is to construct a CAHN-HILLIARD or GINZBURG-LANDAU free energy functional  $\mathcal{F}(\phi)$ , where the so-called phase-field  $\phi(\underline{r}, t)$  serves as an order parameter that can either be conserved or nonconserved. In chapters 3 and 4, we will deal with a conserved parameter, in chapter 5 with a nonconserved one. This phase-field is assumed to *not* have a discontinuous jump at the interface, but instead, it varies *smoothly* over a finite interface width  $\xi$ .

This is achieved in the following way: each functional  $\mathcal{F}$  contains three terms as standard ingredients, which we explain individually below. The first term is the so-called DOUBLE WELL POTENTIAL. Since there are two stable homogeneous states,  $\mathcal{F}$  has a part that depends only on a so-called double-well potential  $w(\phi)$  that has two local minima at  $\phi^{(1)}$  and  $\phi^{(2)}$ . Those minima can be chosen without loss of generality to be at  $\phi^{(1)} = 1$  for one phase and  $\phi^{(2)} = 0$  for the other phase, like in

$$w(\phi) = a\phi^2(1 - \phi)^2 \quad (2.96)$$

with the positive coefficient  $a = 6\gamma/\xi$ , see Fig. 2.12.

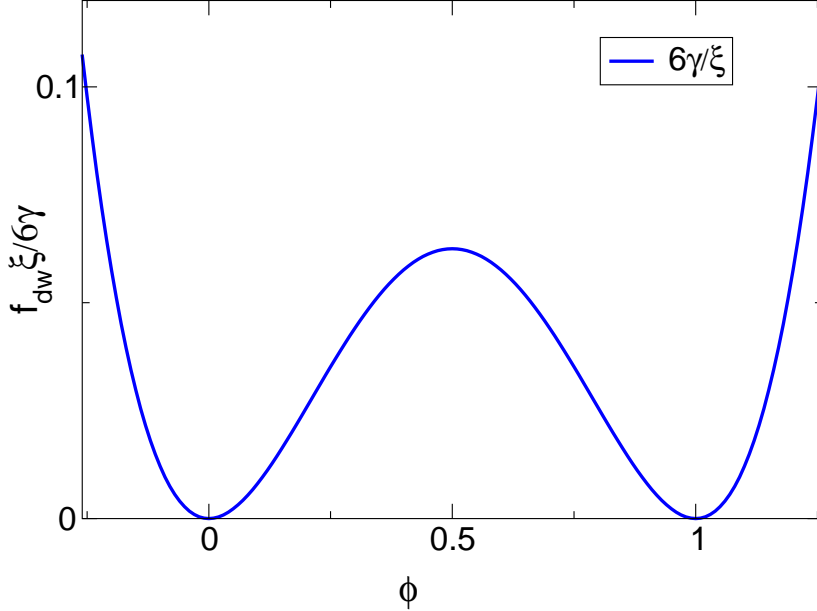


Figure 2.12.: Plot of the double well potential. The minima correspond to the preferred bulk values of the system.

This way,  $\phi$  describes to which phase a given point  $\underline{r}$  at a given time  $t$  belongs. There is a considerable degree of freedom in choosing the position of the minima and the form of the double-well potential term. In [11, 10], a non-smooth "double obstacle" potential of the form

$$w(\phi) = f(\phi) + I_{[-1,1]}, \quad f(\phi) = \frac{a}{2}(1 - \phi)^2 \quad (2.97)$$

$$I_{[-1,1]} = \begin{cases} \infty, & |\phi| > 1 \\ 0, & |\phi| \leq 1 \end{cases} \quad (2.98)$$

is used. It has the minima at  $\phi = \pm 1$  and the smooth potential is truncated by the indicator function  $I_{[-1,1]}$ . The point is that the specific choice of minima is not important, as long as the model is constructed in such a way that the chosen minima correspond to the desired values that denote different phases.

In the region between those two minima, which is  $0 < \phi < 1$  in our case, the phase-field parameter varies smoothly, so we have to take care of the inhomogeneous phase mixture at the interface. For that reason, the energetic influence of variations is incorporated by adding a GRADIENT TERM. The idea is that a strongly fluctuating order parameter is energetically less favorable than an order parameter with little variations. The only terms meeting the requirements of symmetry are  $\phi \Delta \phi$  and  $(\nabla \phi)^2$ . Since for the volume integrations required for  $\mathcal{F}$ , both terms differ only in an unimportant boundary integral,

which vanishes if the interface under investigation is completely inside the integration volume, it is sufficient to include only one of the terms. Therefore, a reasonable ansatz for the phase-field functional has the form

$$\mathcal{F}(\phi) = \int_V (a\phi^2(1-\phi)^2 + b|\nabla\phi|^2) d^3r \quad (2.99)$$

with the coefficient  $b = 3\gamma\xi/2$ .

The gradient term has the tendency to enlarge the transition region, since large gradients (corresponding to sharp phasefield transitions) are energetically unfavorable, whereas the double well potential keeps the interface region narrow. The interplay of the gradient term and the double-well potential term keeps the phasefield width constant and the transition between the two phases is not sharp, but smeared out over a characteristic interface width  $\xi$ . After the interplay of the gradient energy density and the double-well potential have established a stable diffuse interface region, those terms cooperate to minimize the surface if neither the gradient nor the potential vanishes. This way, the curvature effect of the sharp interface model is accounted for.

If the chemical potential term  $\mu_{ext}$  is zero, the sharp interface equations describe an equilibrium situation with an arbitrary stationary interface position. In the phase-field formulation, this stationary state is described by

$$\frac{\delta\mathcal{F}}{\delta\phi} = 0, \quad (2.100)$$

where  $\delta\mathcal{F}/\delta\phi$  denotes taking the functional derivative with respect to  $\phi$ . In one dimension, the solution of this given by

$$\phi(x) = \frac{1}{2} \left( 1 - \tanh \left( \frac{x - x_0}{\xi} \right) \right), \quad (2.101)$$

so the smooth transition of the interface profile is given by a hyperbolic tangens, see Fig. 2.13

Of course, neither the sharp interface nor the phase-field model included any interesting physical effects. Coupling of external fields can be done by specifying a non-vanishing contribution of  $\mu_{ext}$ , which can be due to temperature fields, concentration fields or, as will be the case in our models, elastic fields. Regardless of the source of the field, the system is no longer in equilibrium.

To illustrate this, we assume a *constant* contribution. The phase-field functional then has the form

$$\mathcal{F} = \int_V (a\phi^2(1-\phi)^2 + b|\nabla\phi|^2 + \mu_{ext}h(\phi)) d^3r, \quad (2.102)$$

where we introduced the interpolating function  $h(\phi)$  to restrict phase transition processes to the interface region. It varies smoothly from the bulk values of the hard phase to the bulk values of the soft phase. There is also a large degree of freedom in how to choose the interpolating function, as it has to satisfy only the conditions

$$h(0) = 0 \quad (2.103)$$

$$h(1) = 1. \quad (2.104)$$

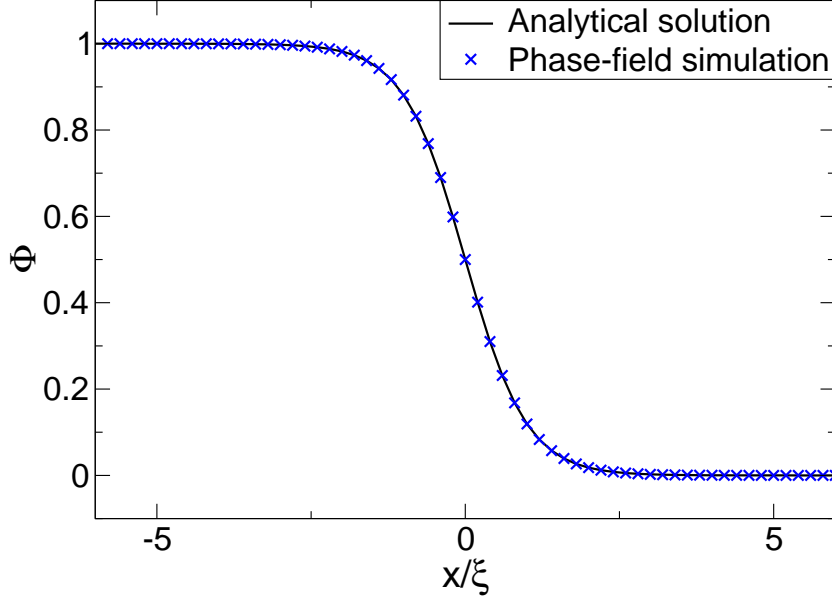


Figure 2.13.: Comparison of the analytic solution for the one-dimensional phase-field equation with the one obtained via phase-field simulations. The interface varies smoothly between  $-\xi$  and  $\xi$ .

If the chosen function has the additional feature  $h'(0) = h'(1) = 0$ , the bulk states  $\phi = 0$  and  $\phi = 1$  are not shifted, which improves the numerical stability. The actual results do not depend on the chosen function, and a common choice is

$$h(\phi) = \phi^2(3 - 2\phi). \quad (2.105)$$

If external fields are present, the solution of a reaction-diffusion-equation for the temporal and spatial evolution of the phasefield, the so-called PHASE-FIELD EQUATION is necessary. It is given by the functional derivative

$$\begin{aligned} \frac{\partial \phi}{\partial t} &= -\frac{D}{3\gamma\xi} \frac{\delta F}{\delta \phi} \\ &= D \left( \nabla^2 \phi - \frac{4}{\xi^2} \phi(2\phi^2 - 3\phi + 1) - \frac{\mu_{ext}}{3\gamma\xi} \frac{\partial h}{\partial \phi} \right). \end{aligned} \quad (2.106)$$

and ensures that the motion of the interface obeys the required physical laws [55]. In the simple case of a constant contribution  $\mu_{ext}$ , in one dimension, this can still be solved analytically

$$\phi(x) = \frac{1}{2} \left( 1 - \tanh \left( \frac{x - vt}{\xi} \right) \right), \quad (2.107)$$

with a constant propagation velocity of

$$v = \frac{D\mu_{ext}}{\gamma}. \quad (2.108)$$

Generally, the external coupling  $\mu_{ext}$  is not constant but depends on the phase-field as well. We will see this in chapter 4 and chapter 5, when we consider elastic fields. Then, the phase-field equation has to be evaluated numerically.

A phase-field functional of that form corresponds exactly to the “model C” in the classification of dynamical universality classes of Hohenberg and Halperin [55].

## 2.6. Conclusion

In this chapter, we introduced the macroscopic theory of linear elasticity and the basic ideas of classical continuum fracture mechanics. We pointed out that the actual physical processes at the crack tip are unknown and lumped together in the process zone. Being based on Griffith’s energy balance criterion provides the idea that cracks can be described by global quantities, and the importance of the stress intensity factor for the description of a crack’s behavior was explained. A major problem of fracture mechanics with sharp crack tip descriptions is that the stresses at the tips diverge, which is known as the square root singularity. It is therefore highly desirable to find a theory that can regularize the fields around the tip. A macroscopic crack description as a free boundary requires some kind of mass transport. We explained the two mass transport mechanisms we will deal with in this thesis and pointed out the connection of conventional fracture mechanics to the Grinfeld instability, which is a morphological instability due to external stress that can lead to very rapidly advancing grooves. In short, the connection consists in the fact that in both cases, interface movement is due to a competition between elastic energy and surface energy. Finally, we explain the main idea behind the phase-field method.



## 3. Phase-Field Models for Surface Diffusion

In this chapter, we concentrate on mass transport by surface diffusion. We first specify the sharp-interface model to be approximated by the phase-field equations. Then, we present the standard approach that was previously supposed to correctly describe the dynamical interface evolution and reduce to the correct sharp-limit. We show that this is not the case and pinpoint the oversight in existing asymptotic analyses. For pedagogical reasons, we present an alternative approach in Sec. 3.4 that fails for complementary reasons. By the insight gained about the failing mechanisms of both approaches and by appropriate combination of underlying ideas, two phase-field models will be deduced that do produce the correct asymptotic behavior.

Parts of this chapter have been published in [44].

### 3.1. Phase-Field Modeling for Surface Diffusion

As we pointed out in section 2.4, the Asaro-Tiller-Grinfeld instability, which is a morphological instability of a uniaxially stressed surface or interface, is strongly related to crack propagation, since the system diminishes its stored elastic energy by increasing its surface area. This counterplay between releasing elastic energy and increasing surface energy also provides the basic mechanism of interface movement during crack propagation. In case of the Grinfeld instability, the system can decrease its total energy if the wavelength of the perturbation exceeds a critical macroscopic lengthscale, which depends on the external applied stress.

It is important to emphasize that any macroscopic description of interfacial pattern movement requires some kind of transportation process. Initially, the treatment of the aforementioned Asaro-Tiller-Grinfeld instability [3, 43, 81, 68, 69], where elastic energy drives the instability with respect to material transport, focused on transport by surface diffusion. This was not only the case in the first article by Asaro and Tiller [3], but also in the first numerical simulations by sharp-interface continuum models [117] and preceding computations of the instability under transport by melting-crystallization [67]. The important point here is that mass transport by surface diffusion leads to *conserved* dynamics.

It is known that in the late stage of the Grinfeld instability, deep grooves form which become increasingly sharp at the tips and advance very rapidly, very similar to cracks. It is known that surface diffusion can support such a fast interface propagation [16] for small tips, when particles have to be transferred only over small distances; we refer to section 2.3 for a detailed discussion.

Here, we would like to point out another common feature of our understanding of cracks and the interfacial movement in the Grinfeld instability: in both cases, the elastic fields



determine the motion of every point of the interface, but the elastic fields are also strongly dependent on the given shape and movement of the interface. This interaction between the external fields and the interface movement belongs to the group of FREE MOVING BOUNDARY PROBLEMS, which are notoriously hard to solve. During the last decades, phase-field models have been established as powerful tools to tackle this kind of problem. There is an early article by Caginalp [22], in which he studies the modifications introduced into a solidification model by making the phase-field a conserved order parameter; this model is not intended to describe surface diffusion, however. Only recently has surface diffusion been considered in phase-field models treating elastically stressed materials [25, 77, 11, 99, 119].

In the following, we will show explicitly the fundamental problem that plagues the conventional phase-field models for surface diffusion that are based on a scalar Cahn-Hilliard functional, which is that it can not be used to reliably describe the desired non-equilibrium interface dynamics as given by the sharp-interface equations. The deeper reason, as we will point out, is that the isotropic modeling of a scalar phase-field model is not well suited to model the anisotropic process of surface diffusion, where matter travels only *along* the interface. We will then present two new models that incorporate this new insight and show the correct behavior. These two new and an existing model from the literature [99] that does not suffer from this problem are introduced and compared analytically. Since these three models all have the correct asymptotics, numerical simulations are necessary to assess their respective virtues and drawbacks. These numerical investigations will be shown in chapter 4. The numerical studies will deal with both, the free model, where the surface diffusion process is solely driven by curvature effects, and an extended model, where elastic effects are also incorporated.

### 3.2. Sharp-Interface Model for Motion Induced by Curvature

We start by considering a curved interface between two phases without any elastic stresses. In this simple case, the motion of the interface is only driven by curvature, as the system tries to reduce its surface energy by flattening out the interface. The local chemical potential difference between the solid and the second phase (vacuum, vapor or liquid) can be written as

$$\mu = \frac{1}{\rho_s} \gamma \kappa, \quad (3.1)$$

where  $\rho_s$  is the density of the solid phase,  $\gamma$  the (isotropic) surface tension and  $\kappa$  the curvature. A positive curvature corresponds to a locally convex solid phase, a negative one to a locally concave solid and the normal points from the solid into the second phase, see Fig. 3.1, where  $V^{(1)}$  denotes volume of the solid phase. For the unstable state with a perturbed interface, however, some dynamical law governing the motion of the interface must be stated.

For material transport by surface diffusion, the driving force is the gradient of the chemical potential along the surface, producing a surface current  $j \propto -\nabla_s \mu$  ( $\nabla_s$  is the surface gradient), which leads to a dynamical law of the form [53, 83, 84]

$$v_n = M_s \Delta_s \mu, \quad (3.2)$$

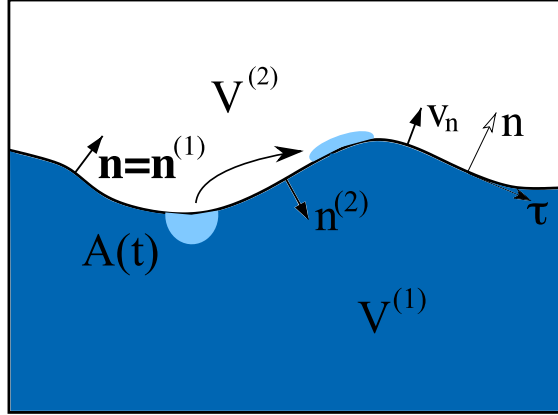


Figure 3.1.: Geometry of the general setup.  $V^{(1)}$  denotes the volume of the solid phase. Matter diffuses along the interface, which leads to an interface motion with local normal velocity  $v_n$ . The interface  $A(t)$  is therefore time-dependent.

where  $M_s$  is a mobility coefficient, assumed constant here, and  $\Delta_s$  is the Laplace-Beltrami operator on the surface. This operator used on a scalar function  $f$  in a local coordinate system is defined as

$$\Delta_s = \frac{1}{\sqrt{|g|}} \partial_i \sqrt{|g|} \partial^i f \quad (3.3)$$

with  $g$  being the determinant of the inverse metric tensor  $\underline{g}$ . For a Euklidian space, it has the form  $g_{ij} = \delta_{ij}$  with the Kronecker symbol  $\delta$ , so having  $|g| = 1$ , it reduces to  $\Delta_s = \partial^2$ . In two dimensions, the Laplace-Beltrami tensor reduces to a double derivative with respect to the arc length for a one-dimensional interface, leading to

$$v_n = M_s \frac{\partial^2 \mu}{\partial s^2}, \quad (3.4)$$

From (3.1), we can see immediately that a planar interface is energetically stable: a solid protrusion leads to growth of the liquid phase because the bump is convex. A liquid protrusion leads to a concave bump and consequently, the solid phase grows.

The surface diffusion process has the physically desirable property that it leads to *conservative* dynamics in that the amount of solid material is constant. Actually, any model that can be written in the form

$$\frac{\partial \phi}{\partial t} = \nabla \cdot \underline{j} \quad (3.5)$$

is conservative, no matter how  $\underline{j}$  is chosen. But the main point of our investigations is *not* whether the dynamics are conservative, but rather whether the corresponding phase-field model produces the correct sharp interface equations.

Eqs. (3.1) and (3.4) constitute the continuum model for the conserved model for transport by surface diffusion. These are the sharp interface equations to which a phase-field

model should converge in the limit of asymptotically small interface width, eventually also with couplings to other fields.

While it is quite straightforward to set up a conservative phase-field model, it is considerably more difficult to obtain the correct asymptotics describing surface diffusion as given by the desired sharp-interface limit. Past models such as the ones presented in [25, 77, 11, 119] produce asymptotically a set of equations *containing* the desired limit equations; however, they include an *additional restriction*, i.e., they have one equation too many, leading to the undesirable statement that strictly, they are only applicable if the curvature vanishes. Only the model given in [99] does not contain this restriction, but the authors state that their improvement is only a stabilizing element that does not change the asymptotics. However, our analysis shows that they have in fact proposed a model that has in reality superior asymptotic behavior. This might have been the reason why the additional constraint seems to have been overlooked before. We will see that the flaw of the faulty models is subtle, but it leads to an effectively uncontrolled approximation of the dynamics and no a priori estimation of how strong the results will be affected can be given.

### 3.3. Scalar-Mobility Phase-Field Model

#### 3.3.1. The Traditional Approach

Starting from a Cahn-Hilliard equation with a concentration dependent mobility, Cahn et al. [25] obtained an interface equation with the normal velocity proportional to the Laplacian of the mean curvature. It then appears as if an analogous derivation would lead to a phase-field model for surface diffusion, and indeed, comparable models have been applied in the simulation of electromigration and voiding in thin metal films [77, 11]. These two models are slightly different, but the difference is not crucial and all previous models except the one given in [99] seem to suffer from the same problem, to be discussed in the following.

We will concentrate on two dimensions but it should be emphasized our findings are equally valid in three dimensions [66].

The standard approach to a phase-field description of surface diffusion, as proposed in [119, 25, 77, 11], is to write the evolution of the phase-field  $\phi$  in the following form

$$\begin{aligned} \frac{\partial \phi}{\partial t} &= -\nabla \cdot \underline{j}, \\ \underline{j} &= -\tilde{M} \nabla \frac{1}{\xi^2} \tilde{\mu}(\nabla^2 \phi, \phi), \\ \tilde{\mu}(\nabla^2 \phi, \phi) &\equiv -\xi^2 \nabla^2 \phi + 2w'(\phi), \end{aligned} \tag{3.6}$$

where  $\tilde{M}$  is a scalar function of either  $\phi$  [119, 25, 11] or  $\xi \nabla \phi$  [77], chosen such that the mobility tends to zero far from the interface:  $\tilde{M}(\phi, \xi \nabla \phi) \rightarrow 0$  for  $\phi \rightarrow 0$  and  $\phi \rightarrow 1$ .  $\tilde{\mu}$  is a nondimensionalized chemical potential difference, and  $w' = (\phi^2(1-\phi)^2)' = 2\phi(1-\phi)(1-2\phi)$  is the derivative of the double-well potential. We will refer to the model described by Eqs. (3.6) as the SCALAR-MOBILITY MODEL or briefly SM MODEL in the following.

As we already mentioned before, the field  $\phi$  is the density of a conserved quantity by construction, since it can be written as the divergence of a vector field (namely the one defined in Eq. (3.6)). This is true for any (nonsingular) form of the mobility function  $\tilde{M}$ . As we mentioned before, the issue with the model is not so much whether the dynamics is conservative but whether it does reduce to the sharp-interface model of Sec. 3.2 in the limit of an asymptotically vanishing interface thickness,  $\xi \rightarrow 0$ .

Actually, very few restrictions on the mobility function  $\tilde{M}$  have to be imposed, mainly positivity (for almost all values of  $\phi$  or  $\nabla\phi$ ) and boundedness. The asymptotic results depend very little on the form of  $\tilde{M}$ , as the conservation law plus the absence of diffusion in the bulk, ensured by  $\tilde{\mu}$  becoming zero for  $\phi \rightarrow 0$  and  $\phi \rightarrow 1$ , restrict transport to diffusion along the interface. If the model has not reached its asymptotic state yet, a restriction imposed by the asymptotics can be not fully effective or not yet satisfied in the temporal evolution of the system. Only then,  $\tilde{M}$  has to decay sufficiently fast inside the bulk for the limit to make sense.

To investigate the asymptotic behavior, we have to explicitly carry out the asymptotic analysis. The basic idea of such an analysis is to expand all dynamical quantities in terms of the small parameter  $\xi$  describing the interface thickness, to solve for the phase field  $\phi$  and to use the obtained solution to eliminate its explicit appearance from the equations.

To this end, the domain of definition of the field is divided into an outer and an inner region. The outer expansion describes the fields far away from the interface and gradients of the fields can be considered to be of order one. The inner region describes the field close to the interface where the gradients are of order  $1/\xi$ . After finding solutions for the inner and outer region expansions, one has to do an asymptotic matching to obtain a smooth global solution for the fields. In the following, we will denote inner quantities by uppercase letters and correspondingly the outer quantities by lowercase letters whenever this is meaningful.

### 3.3.2. Local Coordinate System

Before we start the expansion of the inner phase, it is useful to introduce a local coordinate system that is well suited for the boundary's geometry. To these means, we define locally orthogonal coordinates  $r$  and  $s$ , where  $r$  is orthogonal to the interface; it is the signed distance from the interface, which is determined by the level set corresponding to  $\phi(x, z, t) = 1/2$ . This coordinate is then rescaled by a stretching transformation  $r = \xi\rho$  to point out explicitly the dependence on  $\xi$  for the following expansion. The coordinate  $s$  is the arc length of the interface curve and denotes the tangential to  $r$ .

Inner and outer solutions must satisfy certain matching conditions, see Appendix A.2 due to the requirement that they agree in the combined limit  $\xi \rightarrow 0$ ,  $\rho \rightarrow \pm\infty$ ,  $r \rightarrow 0$ .

Defining the coordinates is straightforward: if  $\underline{R}$  is the position of the interface and  $\underline{n}$  the normal vector on it (oriented the same way as in the sharp-interface model, i.e., pointing out of the solid), we assign a point near the interface by the position vector

$$\underline{r} = \underline{R}(s) + r \underline{n}(s), \tag{3.7}$$

### 3.3. SCALAR-MOBILITY PHASE-FIELD MODEL

---

An orthogonal basis is then given by

$$\begin{aligned}\underline{\mathcal{E}}_r &\equiv \frac{\partial \underline{r}}{\partial r} = \underline{n}(s), \\ \underline{\mathcal{E}}_s &\equiv \frac{\partial \underline{r}}{\partial s} = \frac{\partial \underline{R}}{\partial s} + r \frac{\partial \underline{n}}{\partial s} = (1 + r\kappa) \underline{\tau},\end{aligned}\tag{3.8}$$

where  $\underline{\tau} = \partial \underline{R} / \partial s$  is the unit tangent vector to the interface, and  $\partial \underline{n} / \partial s = \kappa \underline{\tau}$  is the two-dimensional version of one of the Frenet formulas [112].

Eq. (3.8) determines the metric coefficients  $g_{\alpha\beta} = \underline{\mathcal{E}}_\alpha \underline{\mathcal{E}}_\beta$  for this coordinate system with  $\alpha, \beta \in \{r, s\}$ . Accordingly, the metric tensor reads

$$\underline{\underline{g}} = (g_{\alpha\beta}) = \begin{pmatrix} 1 & 0 \\ 0 & (1 + r\kappa)^2 \end{pmatrix},\tag{3.9}$$

and its determinant is

$$g \equiv \det \underline{\underline{g}} = (1 + r\kappa)^2,\tag{3.10}$$

so that  $\sqrt{g} = 1 + r\kappa$ . Basic vector analysis then tells us that the contravariant components of the metric tensor are obtained as

$$\underline{\underline{g}}^{-1} = (g^{\alpha\beta}) = \begin{pmatrix} 1 & 0 \\ 0 & (1 + r\kappa)^{-2} \end{pmatrix}.\tag{3.11}$$

From now on, we use the Einstein summation convention for pairs of covariant and contravariant indices. The vectors of the reciprocal basis are obtained from  $\underline{\mathcal{E}}^\alpha = g^{\alpha\beta} \underline{\mathcal{E}}_\beta$ :

$$\begin{aligned}\underline{\mathcal{E}}^r &= \nabla r = \underline{n}(s), \\ \underline{\mathcal{E}}^s &= \nabla s = \frac{1}{\sqrt{g}} \underline{\tau},\end{aligned}\tag{3.12}$$

The last quantities needed in these coordinates are the general expressions for gradient and divergence, which read

$$\nabla = \underline{\mathcal{E}}^\alpha \partial_\alpha,\tag{3.13}$$

$$\nabla \cdot \underline{A} = \frac{1}{\sqrt{g}} \partial_\alpha \left( \sqrt{g} g^{\alpha\beta} A_\beta \right).\tag{3.14}$$

One should note that at the interface, the covariant component  $A_r$  is equal to the normal component  $A_n$ . Because  $\underline{\mathcal{E}}^s$  is not normalized to one,  $A_s$  is related to the tangential component  $A_t$  by  $A_s = \sqrt{g} A_t$ . In order to see how the operators scale in this context, we write Eqs. (3.13) and (3.14) in the form

$$\nabla = \frac{1}{\xi} \underline{n} \partial_\rho + \frac{1}{\sqrt{g}} \underline{\tau} \partial_s,\tag{3.15}$$

$$\nabla \cdot \underline{A} = \frac{1}{\sqrt{g}} \left( \frac{1}{\xi} \partial_\rho \sqrt{g} A_r + \partial_s \frac{1}{\sqrt{g}} A_s \right),\tag{3.16}$$

$$\sqrt{g} = 1 + \xi \rho \kappa.\tag{3.17}$$

The time derivative has to be transformed as well, because the interface, on which the definitions of the coordinates  $r$  and  $s$  are based, can itself be moving. If  $\underline{v}(s, t)$  is the interface velocity, we obtain

$$\frac{\partial f(x, z, t)}{\partial t} = \frac{\partial F(r, s, t)}{\partial t} - \underline{v} \cdot \nabla F(r, s, t), \quad (3.18)$$

which has the form of a material derivative in the comoving frame of reference.

### 3.3.3. Inner Equations

Using the above definition Eqs. (3.15)–(3.17), we obtain for the differential operator part of Eq. (3.6):

$$\nabla \cdot \tilde{M} \nabla = \frac{1}{\xi^2} \frac{1}{\sqrt{g}} \partial_\rho \sqrt{g} \tilde{M} \partial_\rho + \frac{1}{\sqrt{g}} \partial_s \frac{1}{\sqrt{g}} \tilde{M} \partial_s. \quad (3.19)$$

The chemical potential has the form

$$\tilde{\mu}(\nabla^2 \Phi, \Phi) = -\frac{1}{\sqrt{g}} \partial_\rho \sqrt{g} \partial_\rho \Phi - \xi^2 \frac{1}{\sqrt{g}} \partial_s \frac{1}{\sqrt{g}} \partial_s \Phi + 2w'(\Phi) \quad (3.20)$$

Without loss of generality, we can assume that the tangential velocity of the interface vanishes and Eq. (3.6) takes the following form

$$\partial_t \Phi - \frac{1}{\xi} v_n \partial_\rho \Phi = \nabla \cdot \tilde{M} \nabla \frac{1}{\xi^2} \tilde{\mu}(\nabla^2 \Phi, \Phi) \quad (3.21)$$

We see that the leading term of the inner equation (3.21) with the differential operator given by (3.19) is of order  $\xi^{-4}$ .

### 3.3.4. Expansions, Matched Asymptotic Analysis

We denote the inner fields with  $\Phi$  and the outer fields with  $\phi$ . To solve the outer and inner equations successively, we have to expand the phase-field in both the outer and inner domains in powers of the interface width  $\xi$ .

We start with the expansion in the outer domain, which is straightforward, taking Eq. (3.6) as our starting point. We obtain

$$\phi(x, z, t) = \phi^{(0)}(x, z, t) + \xi \phi^{(1)}(x, z, t) + \xi^2 \phi^{(2)}(x, z, t) \dots \quad (3.22)$$

and the inner equation becomes

$$\Phi(r, s, t) = \Phi^{(0)}(r, s, t) + \xi \Phi^{(1)}(r, s, t) + \xi^2 \Phi^{(2)}(r, s, t) \dots \quad (3.23)$$

The next step in the procedure is to solve the outer and inner equations order by order.

### Leading Order, Outer Equation

The leading-order outer equation for  $\phi$ , which follows immediately from Eq. (3.6), is

$$\nabla \cdot \tilde{M} \nabla w'(\phi^{(0)}) = 0. \quad (3.24)$$

Additionally, boundary conditions for the respective bulk regions at infinity, where the system is either solid or non-solid, have to be applied. We set them to be  $\phi^{(0)} = 1$  for the solid and  $\phi^{(0)} = 0$  for the non-solid phase.

Eq. (3.24) can be understood as a partial differential equation for the function  $w'(\phi^{(0)})$  instead of  $\phi^{(0)}$ , which in turn translates the above boundary conditions into  $w'(\phi^{(0)}) \rightarrow 0$  as  $|r| \rightarrow \infty$ . The new boundary condition is valid everywhere at infinity. For general  $\tilde{M}(\phi, \xi \nabla \phi)$ , the partial differential equation (3.24) is of course nonlinear. Nevertheless, under certain mild conditions (if  $\tilde{M}$  is positive almost everywhere, i.e. except possibly on a set of measure zero), it can be shown to have the unique solution

$$w'(\phi^{(0)}) = 0 \quad (3.25)$$

This is of course the solution we expected, as in the sharp interface limit, the system must be in one of the stable states  $\phi^{(0)} = 0$  or  $\phi^{(0)} = 1$ . The solution Eq. (3.25) has the very convenient property that it does not only solve the outer equation to first order, but to *all* orders. Therefore, we have  $\phi^{(1)} \equiv 0$ ,  $\phi^{(2)} \equiv 0$ , which provides us with partial boundary conditions for the inner solutions  $\Phi^{(1)}$ ,  $\Phi^{(2)}$ , and so on, see Appendix A.2.

Moreover, only the inner problem needs to be considered beyond the leading order. For the analytical treatment, we only consider a “free” model without coupling to external fields, like mechanical or electrical degrees of freedom; however, this statement remains true for the fully coupled phase-field model when the coupling is modeled along the usual lines of [68, 77].

### Leading Order, Inner Equation

We now need to find the solution for the inner equation in leading order. Because the metric tensor scales as  $g = 1 + O(\xi)$ , Eqs. (3.19) - (3.21) give us

$$\partial_\rho \tilde{M}(\Phi^{(0)}) \partial_\rho \left[ \partial_{\rho\rho} \Phi^{(0)} - 2w'(\Phi^{(0)}) \right] = 0 \quad (3.26)$$

for the leading-order inner problem, where  $\partial_{\rho\rho} = \partial_\rho^2$ . Since there are no curvature terms in Eq. (3.26), it corresponds to the usual one-dimensional phase-field equation and will provide us with the expected solution  $\Phi^{(0)} = \frac{1}{2}(1 - \tanh \rho)$ .

However, we will employ a more detailed reasoning, since an accurate treatment of the boundary conditions will also be necessary when dealing with the higher order equations. We start with integrating the above equation once and obtain

$$\partial_\rho \left[ \partial_{\rho\rho} \Phi^{(0)} - 2w'(\Phi^{(0)}) \right] = \frac{c_1(s)}{\tilde{M}(\Phi^{(0)})}, \quad (3.27)$$

where  $c_1(s)$  is a function of integration. Depending on the assumption of the behavior of  $\tilde{M}$ , different arguments have to be used:

- If  $\tilde{M}$  is just a bounded (and possibly constant) function of  $\phi$ , we obtain the same result by integrating (3.27) again and then make use of the boundary conditions:

$$\partial_{\rho\rho}\Phi^{(0)} - 2w'(\Phi^{(0)}) = c_1(s) \int_0^\rho \frac{1}{\tilde{M}} d\rho + c_2(s). \quad (3.28)$$

From this, we can conclude that  $c_1$  and  $c_2$  must be equal to zero: we use that  $\tilde{M}$  is bounded from above and positive, so that the integral will be larger in magnitude than  $\int_0^\rho 1/(\sup_\rho \tilde{M})d\rho = \rho/\sup_\rho \tilde{M}$ . Since the left hand side approaches zero for  $\rho \rightarrow \pm\infty$  and the two factors multiplying  $c_1$  and  $c_2$  are linearly independent, we can draw that conclusion.

- If  $\tilde{M}$  approaches zero for  $\rho \rightarrow \pm\infty$ , which is the case for the mobilities assumed in [119, 25, 11], we may immediately conclude  $c_1 = 0$ , because the right hand side of (3.27) must not diverge.

To summarize, the leading-order inner equation leads to

$$\partial_{\rho\rho}\Phi^{(0)} - 2w'(\Phi^{(0)}) = 0, \quad (3.29)$$

and this provides us with the well-known solution

$$\Phi^{(0)} = \frac{1}{2} (1 - \tanh \rho). \quad (3.30)$$

### Next-to-Leading Order

Looking at Eq. (3.21), we see that the next-to-leading order is the order  $\xi^{-3}$ . Since the differential operator in front of the chemical potential is of order  $\xi^{-2}$  and the chemical potential is multiplied by another factor  $\xi^{-2}$ , the expansion of  $\tilde{\mu}$  must be done up to order  $\xi$ . From Eq. (3.29), we can already read off  $\tilde{\mu}^{(0)} = 0$ . The next order is then

$$\partial_\rho \tilde{M}(\Phi^{(0)}) \partial_\rho \tilde{\mu}^{(1)} = 0. \quad (3.31)$$

Treating it in a similar fashion as before, it leads us to

$$\partial_\rho \tilde{\mu}^{(1)} = \frac{d_1(s)}{\tilde{M}(\Phi^{(0)})}. \quad (3.32)$$

Similar arguments as before apply: for arbitrary but bounded  $\tilde{M}$ , employing the matching conditions (see Appendix A.2) gives us

$$\lim_{\rho \rightarrow \pm\infty} \partial_\rho \tilde{\mu}^{(1)} = \partial_r \tilde{\mu}_{\text{out}}^{(0)}|_{\pm 0} = 0, \quad (3.33)$$

and we obtain the same result (where for once we have denoted an outer quantity by a subscript "out"). In the other case of  $\tilde{M}(\Phi^{(0)}) \rightarrow 0$  for  $\Phi^{(0)} \rightarrow 0$  or  $\Phi^{(0)} \rightarrow 1$ , the boundary conditions give us immediately  $d_1 = 0$ .



### 3.3. SCALAR-MOBILITY PHASE-FIELD MODEL

---

Integrating once more with respect to  $\rho$  and writing out  $\tilde{\mu}^{(1)}$ , we obtain for the chemical potential

$$\begin{aligned}\tilde{\mu}^{(1)} &= -\partial_{\rho\rho}\Phi^{(1)} - \kappa\partial_{\rho}\Phi^{(0)} + 2w''(\Phi^{(0)})\Phi^{(1)} \\ &= d_2(s).\end{aligned}\tag{3.34}$$

The first two terms on the right hand side resemble the ones we would obtain for a Laplacian in polar coordinates. While the first order expansion provides us with the equation for a planar interface, the next order includes the first correction due to the curvature. We would like to point out that these results are in full accordance with the ones obtained in [77], were a similar asymptotic analysis was carried out.

As we will demonstrate, there are two justified, totally independent ways of determining the function of integration  $d_2(s)$ . We start with the conventional method: if we interpret Eq. (3.34) as a linear inhomogeneous differential equation for  $\Phi^{(1)}$ , we can multiply it by  $\partial_{\rho}\Phi^{(0)}$  and integrate it by parts to show that the terms containing  $\Phi^{(1)}$  disappear. This way, we obtain from (3.34)

$$-\int_{-\infty}^{\infty}\kappa\left(\partial_{\rho}\Phi^{(0)}\right)^2d\rho = \int_{-\infty}^{\infty}\partial_{\rho}\Phi^{(0)}d_2(s)d\rho = -d_2(s),\tag{3.35}$$

from which we get, using the tanh solution for  $\Phi^{(0)}$ ,

$$d_2(s) = \frac{1}{3}\kappa.\tag{3.36}$$

While this looks like the desired result, the story does not end here, unfortunately.

Since the procedure we used before has proven to be successful and there is no reason to use a different one, we could also have chosen to continue analysing the asymptotic behavior. Inspecting the right hand side of (3.34), we already know the limiting behavior for  $\rho \rightarrow \pm\infty$  for two of the four terms. The first is of course  $\lim_{\rho \rightarrow \pm\infty} d_2(s) = d_2(s)$ , since  $d_2$  is independent of  $\rho$ . Then, by using the matching conditions or by using the solution (3.30), we see that:

$$\lim_{\rho \rightarrow \pm\infty} \partial_{\rho}\Phi^{(0)} = 0.\tag{3.37}$$

Moreover, the matching conditions provide one additional limit, the one for  $\Phi^{(1)}$ :

$$\begin{aligned}\Phi^{(1)} \sim \rho\phi^{(0)}(\pm 0) + \phi^{(1)}(\pm 0) &= \phi^{(1)}(\pm 0) = 0 \\ &(\rho \rightarrow \pm\infty),\end{aligned}\tag{3.38}$$

where we use fact that  $\phi^{(0)} = 0$  or  $\phi^{(0)} = 1$ , therefore its derivative with respect to  $r$  vanishes on both sides of the interface; the third equality is a consequence of the fact that  $\phi^{(0)}$  solves the outer equation to all orders and hence  $\phi^{(1)} \equiv 0$ . Additional terms that include mechanical degrees of freedom do not change this picture, since they will also lead to terms that vanish in the limit  $\rho \rightarrow \pm\infty$  [66].

With three of the four terms in (3.34) having a definite limit, we can conclude this is the case for the fourth term as well and obtain

$$\lim_{\rho \rightarrow \pm\infty} -\partial_{\rho\rho}\Phi^{(1)} = d_2(s).\tag{3.39}$$

Finding that limit is slightly more involved: We introduce the variable  $\chi = 1/\rho$  to see that

$$\begin{aligned} \partial_{\rho\rho}\Phi^{(1)} &= (\chi^2\partial_\chi)^2\Phi^{(1)} \\ \Rightarrow \Phi^{(1)} &\sim \frac{-d_2}{2\chi^2} \end{aligned} \tag{3.40}$$

Taking the limit of  $\chi \rightarrow 0$  implies that  $\Phi^{(1)}$  would diverge as  $-d_2\rho^2/2$  if  $d_2$  was not zero. One should note even though the matching conditions do not provide a direct expression for  $\lim_{\rho \rightarrow \pm\infty} \partial_{\rho\rho}\Phi^{(0)}$ , the same reasoning could be used to show that the left hand side of Eq. (3.28) goes to zero.

So we obtained by two *independent, valid* methods two *contradictory* results,

$$d_2(s) = \tilde{\mu}^{(1)} = 0. \tag{3.41}$$

on the one hand and Eq. (3.36) on the other hand, and they both should hold true. However, the method of integration is only an *additional* condition to Eq. (3.41). Therefore, Eq. (3.41) can be plugged into Eq. (3.36), which then means that the curvature has to be zero in lowest order. Since in phase-field modeling with additional interaction, be it elastic like in [66] or electric like in [77], there is always the restriction  $\kappa = O(\xi)$ , this means that the phase-field cannot be asymptotic as long as the curvature cannot be neglected.

In a phase-field model for the Asaro-Tiller-Grinfeld instability [66], the same kind of reasoning imposes a relationship between the elastic state of the material and the curvature. In models where the interaction term is quadratic in  $\xi$  [77], it again imposes the restriction  $\kappa = O(\xi)$ .

To summarize: we obtain a restriction on the curvature at lowest order in all cases, which means that the phase-field model will not be asymptotic as long as the deviation from this imposed value is not small.

The implications of this statement are quite dramatic from an analytical point of view: from Eq. (3.36) alone, one can derive

$$v_n = M\partial_{ss}\kappa, \tag{3.42}$$

which reproduces the desired sharp interface limit (3.4). But since we have Eq. (3.41), it follows directly that

$$v_n = 0. \tag{3.43}$$

While the initial stage of any phase-field modeling does not have to be governed by the models asymptotic properties, asymptotics determine the long time behavior. Even in the conceivable case that higher order terms might lead to a nonvanishing interface velocity, Eq. (3.43) however implies the curvature has to be very small compared to all other inverse lengthscales of the system, so that the quantitative validity of the model would be restricted to the near-equilibrium situations. However, the main point of phase-field models is to simulate far-from-equilibrium situations, and our analysis shows that the scalar mobility model can only provide an uncontrolled approximation, since there is no theoretical estimate on the error in the fully asymptotic state. This is the reason that the scalar mobility surface diffusion model applies only to the equilibrium limit. It may

possibly reproduce far from equilibrium dynamics qualitatively, but one cannot expect it to faithfully capture it quantitatively. For a more detailed reasoning of the higher order behavior, see [44].

To conclude our findings so far: The problem with the scalar mobility is that in the asymptotic limit, the differential operator  $\nabla \cdot \tilde{M}\nabla$  is different from the surface Laplacian  $\Delta_s$ , as can be seen in Eq. (3.19). The chemical potential and the operator do not converge both to the sharp interface limit, since the first term in Eq. (3.19) dominates the behavior with its factor of  $1/\xi^2$ .

### 3.4. Tensorial Mobility

If the scalar mobility cannot produce the correct asymptotic behavior, the next level of sophistication is to modify the differential operator  $\nabla \cdot M\nabla$  with an essentially tensorial mobility

$$\frac{\partial\phi}{\partial t} = M\nabla \cdot \underline{\underline{P}}\nabla \frac{1}{\xi^2}\tilde{\mu}(\nabla^2\phi, \phi). \quad (3.44)$$

$M$  is now a constant scalar mobility. We denote the normal vector to the equipotential lines  $\phi = \text{const}$  with  $\underline{n}$  and introduce the operator  $\underline{\underline{P}}$ , which has the form

$$\underline{\underline{P}} = 1 - \hat{n} : \hat{n} \quad (3.45)$$

with

$$\hat{n} = \frac{\nabla\phi}{|\nabla\phi|} = (n_x, n_y)^T, \quad (3.46)$$

and

$$\hat{n} : \hat{n} = \begin{pmatrix} n_x n_x & n_y n_x \\ n_x n_y & n_y n_y \end{pmatrix} \quad (3.47)$$

is the tensor or dyadic product of the normal vectors. Since the operator  $\nabla \cdot \underline{\underline{P}}\nabla$  is a projection operator that projects on the tangential plane of the equipotential line or level set, it should reduce to the surface Laplacian. This idea is conceptually similar to level set approaches, where this kind of projection operator has been used to obtain the surface Laplacian with static [9] and dynamically evolving interfaces [21].

First, one notices that the next-to-leading order already contains the velocity in the form

$$v_n \partial_\rho \Phi^{(0)} = M \partial_{ss} \left\{ \partial_{\rho\rho} \Phi^{(1)} + \kappa \partial_\rho \Phi^{(0)} - 2w''(\Phi^{(0)}) \Phi^{(1)} \right\}. \quad (3.48)$$

Now, we use the fact that the partial derivative  $\partial_{ss}$  commutes with the term  $\partial_{\rho\rho} - 2w''(\Phi^{(0)})$ . By that operation,  $\Phi^{(1)}$  is eliminated from the equation and we seem to obtain the correct sharp-interface limit.

Unfortunately, this model fails for complimentary reasons to the SM-model: the zeroth order solution is not unique, and any (differentiable) function that satisfies the boundary conditions can serve as a phase-field function. Starting from the relation

$$\nabla w'(\phi^{(0)}) = w''(\phi^{(0)}) \nabla \phi^{(0)}, \quad (3.49)$$

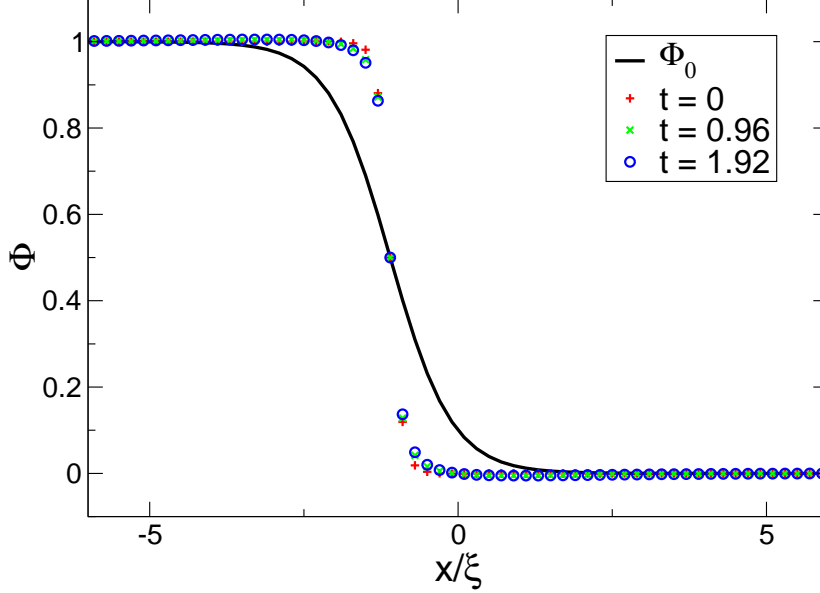


Figure 3.2.: Time evolution of the the phase-field for the unmodified tensorial model if it has been initialized with a narrow interface. The initial interface width is  $0.25 \xi$ , the time  $t$  is given in units of  $\xi^4/M$ . The fact that the profile does not converge to the analytic solution shows the failure of the model.

and plugging that in the leading order outer equation

$$\nabla \cdot \left( 1 - \hat{n}^{(0)} : \hat{n}^{(0)} \right) \nabla w'(\phi^{(0)}) = 0, \quad (3.50)$$

we see that

$$\begin{aligned} \hat{n}^{(0)} : \hat{n}^{(0)} \nabla w'(\phi^{(0)}) &= -\hat{n}^{(0)} w''(\phi^{(0)}) |\nabla \phi^{(0)}| \\ &= w''(\phi^{(0)}) \nabla \phi^{(0)} = \nabla w'(\phi^{(0)}). \end{aligned} \quad (3.51)$$

Eq. (3.51), however, implies that Eq. (3.50) is solved by any function. This particular feature of the model can be seen in Fig. 3.2 and Fig. 3.3: a planar interface is initialized with the wrong interface profile. Since the solution to the equation for Eq. (3.50) is not unique and for a planar interface, the equation of motion contains only terms parallel to the interface, there is no force acting in perpendicular direction to stabilize the phase-field, which would eventually be destroyed by any dynamics.

So, we obtain another unsatisfactory result: in comparison to the SM-model, where we had one constraint too many, there is one constraint missing in the tensorial model, leaving  $\Phi^{(0)}$  undetermined. If this flaw could be remedied by fixing  $\Phi^{(0)}$ , the tensorial model

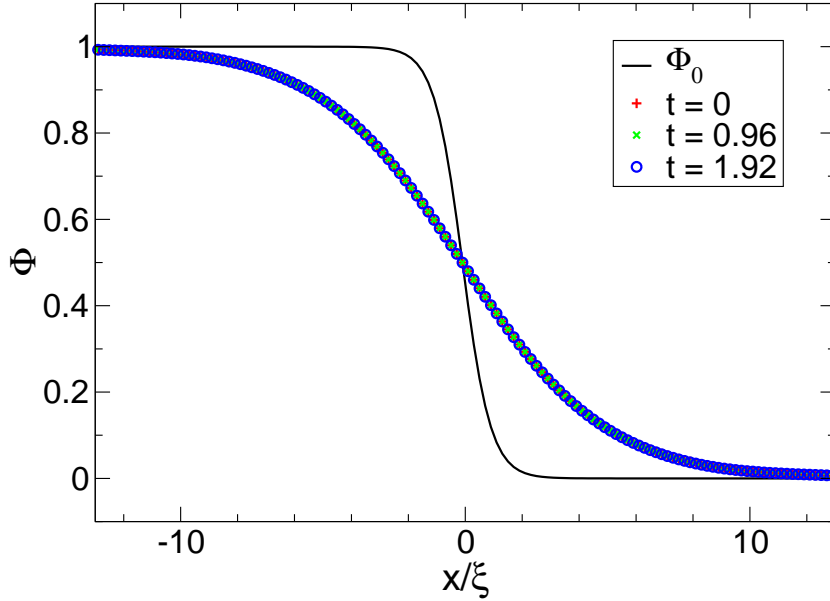


Figure 3.3.: Time evolution of the the phase-field for the unmodified tensorial model if it has been initialized with a too wide interface. The initial interface width is  $0.25 \xi$ , the time  $t$  is given in units of  $\xi^4/M$ . The fact that the profile does not converge to the analytic solution shows the failure of the model.

would show the desired asymptotic behavior. So, the main point of our investigations is to introduce terms that do not destroy the asymptotic behavior of the tensorial model but stabilize the phase-field in such a way that the correct interface form is maintained. We pursue two different approaches to deal with the unstable phase-field of the pure tensorial model.

We call the first approach the **LOCALLY CONSERVED TENSORIAL** model (LCT), and its central idea is to include higher order terms in the projection operator  $\underline{Q}$ .

The other idea leads to a model that we call the **GLOBALY CONSERVED TENSORIAL MODEL** (GCT). In contrast to the LCT-model, the GCT-model adds a small, locally nonconservative term that serves to stabilize the phase-field and restores conservation on a global level.

### 3.5. Modified Tensorial Mobility Models with Correct Asymptotics

In order to overcome the tensorial model's problem of having not enough constraints, we start by modifying the projection operator  $\underline{P} = \underline{1} - \hat{n} : \hat{n}$  into

$$\underline{Q} \equiv 1 - \xi^2 \frac{\nabla\phi : \nabla\phi}{4f(\phi)} = 1 - \frac{\xi^2(\nabla\phi)^2}{4f(\phi)} \hat{n} : \hat{n}. \quad (3.52)$$

If we use this modified operator  $\underline{Q}$  in Eq. (3.44) instead of the projection operator  $\underline{P}$ , then the outer equation exhibits the pleasant property of having the same differential operator at leading order as the scalar model with constant mobility  $M$ .

However,  $\underline{Q}$  is an approximation to  $1 - \hat{n} : \hat{n}$  that is only accurate up to  $O(\xi)$ . This correction would still be present in the higher order inner equation, so we use an even better approximation: since we have  $\underline{Q} = 1 - \hat{n} : \hat{n} + O(\xi) \hat{n} : \hat{n}$  and  $1 - \hat{n} : \hat{n}$  and  $\hat{n} : \hat{n}$  are orthogonal projection operators by construction, taking  $\underline{Q}$  to an integer power leads to

$$\underline{Q}^m = 1 - \hat{n} : \hat{n} + O(\xi^m) \hat{n} : \hat{n}. \quad (3.53)$$

The specific form is

$$\underline{Q}^m = \begin{pmatrix} 1 - (1 - b_0^m)n_x^2 & -(1 - b_0^m)n_x n_y \\ -(1 - b_0^m)n_x n_y & 1 - (1 - b_0^m)n_y^2 \end{pmatrix}$$

with

$$b_0 = 1 - \frac{\xi^2(\nabla\phi)^2}{4f(\phi)}.$$

Combining all those ideas, the phase-field equations then take their final form:

$$\begin{aligned} \frac{\partial\phi}{\partial t} &= -M\nabla \cdot \underline{j} \\ \underline{j} &= -Q^m \nabla \frac{1}{\xi^2} \tilde{\mu}(\nabla^2\phi, \phi), \\ \tilde{\mu}(\nabla^2\phi, \phi) &= -\xi^2 \nabla^2\phi + 2f'(\phi). \end{aligned} \quad (3.54)$$

where the asymptotic analysis provides us with the result that the most suitable choice for  $m$  is  $m = 4$  or a larger even value. The sharp-interface analysis goes along the lines of the SM-Model and has been carried out in detail in our publication [44].

### 3.6. Globally Conservative Model

Another way to overcome the problems that plague the tensorial model and to stabilize the interface is the following: In order to preserve the interface, a small nonconservative term  $N\delta U/\delta\phi$  is added to Eq. (3.44). The derivation of this model is mainly driven by pragmatic considerations, as similar concepts have been successfully used for phase-field modeling in hydrodynamics [82]. While one sacrifices the strict local conservation property of the phase-field equations, and conservation is only fulfilled in the asymptotic limit,

### 3.6. GLOBALLY CONSERVATIVE MODEL

---

the obtained model proves to be numerically very stable and versatile. By introducing a Lagrange-Multiplier, it is possible to restore *global* conservation of the phase-field. Due to this characteristic, we call the model GLOBALLY CONSERVATIVE MODEL; it will be explained below in more detail.

We start again from Eq. (3.44), but instead of altering the projection tensor  $\underline{\underline{P}} = 1 - \underline{\underline{\hat{n}}} : \underline{\underline{\hat{n}}}$  itself, we add a nonconserved term

$$(\underline{\underline{\hat{n}}} \cdot \nabla)^2 \phi - \frac{2}{\xi^2} w'(\phi)$$

to obtain

$$\begin{aligned} \frac{\partial \phi}{\partial t} &= M \nabla \cdot P \nabla \frac{1}{\xi^2} \tilde{\mu} + N \left[ (\underline{\underline{\hat{n}}} \cdot \nabla)^2 \phi - \frac{2}{\xi^2} w'(\phi) \right] \\ \tilde{\mu} &= -\xi^2 \nabla^2 \phi + 2w'(\phi) \end{aligned} \quad (3.55)$$

where both  $M$  and  $N$  are positive constants. A similar asymptotic analysis as in Sec. 3.3.4 reveals that the leading-order outer solution for  $\tilde{\mu}$  is unique with solutions  $\phi = 0$ , given as boundary condition at infinity for the soft phase, and  $\phi = 1$ , which is the respective boundary condition for the hard phase.

Moreover, the leading-order inner solution with boundary conditions  $\lim_{\rho \rightarrow -\infty} \Phi^{(0)} = 0$ ,  $\lim_{\rho \rightarrow \infty} \Phi^{(0)} = 1$  can be shown to be unique up to translations along  $\rho$  and is given by (3.30) after requiring  $\rho = 0$  to correspond to the value  $\frac{1}{2}$  of the phase-field.

The role of the  $N$  term is only to fix the profile of the phase field at leading order, otherwise it is constructed so as to not affect the normal velocity of the interface. Obviously, this model reduces to the tensorial model of Sec. 3.4 in the limit  $N \rightarrow 0$ .

Solving for the outer equation at lowest order goes along the following lines: We write  $\xi = \varepsilon \xi_0$ , and for simplicity and without loss of generality, we set  $\xi_0 = 1$ . Now, we look at the outer solution at lowest order:

$$0 = M \nabla \cdot \left( \underline{\underline{Q}} \nabla \frac{2w'(\phi)}{\varepsilon^2} \right) - 2N \frac{w'(\phi)}{\varepsilon^2} \quad (3.56)$$

This expression is definitely solved by  $w(\phi_0) = 0$ , meaning that the minima of the double well potential will be the preferred states of the system. As for the uniqueness of the solution, we look at the integral

$$\int \left( M w'(\phi) \nabla \underline{\underline{Q}} \nabla w'(\phi) - N w'(\phi)^2 \right) d^3 x = 0 \quad (3.57)$$

If  $w'(\phi) = 0$  on the boundary, we obtain

$$-M \int \nabla w'(\phi) (1 - \underline{\underline{n}} : \underline{\underline{n}}) \nabla w'(\phi) d^3 x - N \int w'(\phi)^2 d^3 x = 0 \quad (3.58)$$

Since both terms have the same sign, the solution is unique for positive  $M$ .

Once  $\Phi^{(0)}$  is set, the next-to-leading order inner equation reads:

$$(M \partial_{ss} - N) \left( \partial_{\rho\rho} - 2w''(\Phi^{(0)}) \right) \Phi^{(1)} = v_n \partial_\rho \Phi^{(0)} - M \partial_{ss} \kappa \partial_\rho \Phi^{(0)}, \quad (3.59)$$

and since  $M\partial_{ss} - N$  commutes with  $\partial_{\rho\rho} - 2w''(\Phi^{(0)})$ , we obtain the desired sharp-interface limit again.

This analytic result actually transfers well to our numerical simulations which showed that the results are largely independent on the choice of the parameter  $N$ . We varied  $N$  over two orders of magnitude, from  $N \leq 2.5M/\xi^2$  to  $N = 1.25 \times 10^{-2}M/\xi^2$ , and find only small differences in the behavior of the system.

### 3.6.1. Restoring Global Conservation

Even though the model as given in Eq. (3.55) is asymptotically conservative and could be already useful as it is, any real long time calculation in a finite system may still be influenced weakly by the non-conserved term. Therefore, we want to restore global conservation in the sense that the total volume integral of  $\phi$  should remain constant (whenever we apply boundary conditions that do not imply fluxes into or out of the system). This can of course be achieved through the means of a Lagrange parameter

$$\frac{\partial\phi}{\partial t} = M\nabla \cdot P\nabla \frac{1}{\xi^2}\delta\tilde{\mu} + N \left[ (\hat{n} \cdot \nabla)^2 \phi - \frac{2}{\xi^2}w'(\phi) \right] - \Lambda(\underline{r}, t), \quad (3.60)$$

where the desired conservation serves as a side condition.

Note that we can still not write the time derivative of  $\phi$  as the divergence of a current

$$\frac{\partial\phi}{\partial t} \neq \nabla \cdot \underline{j}. \quad (3.61)$$

If  $\Lambda$  were restricted to being a simple number, it would have to have the value

$$\begin{aligned} \Lambda &= \frac{1}{V} \int_V dV \frac{\partial\phi_{\text{old}}}{\partial t} \\ &= \frac{N}{V} \int_V dV \left[ (\hat{n} \cdot \nabla)^2 \phi - \frac{2}{W^2}w'(\phi) \right], \end{aligned} \quad (3.62)$$

where  $\partial\phi_{\text{old}}/\partial t$  is the time derivative of the phase field according to (3.55) and  $V$  is the volume (or area, in 2D) of the system. Since the first term of the right hand side of (3.60) is conservative anyway, it drops out of the calculation of  $\Lambda$ , if no fluxes through the system boundary are present. An undesired side effect of the formulation (3.62) is that it would lead to a modification of the phase field values in the bulk; these would lift the phase-field from the equilibrium values 0 and 1 as soon as the Lagrange multiplier became nonzero. This can be avoided by taking advantage of the liberty to make  $\Lambda$  vary in space (i.e., we consider a whole set of Lagrange multipliers, not just one). If we denote the material loss as  $\delta C$  and  $\hat{m} = \delta C/S_G$  as the relative value to be added (with  $S_G = \sum_{i,j} |\nabla\phi_{ij}|$ ) and take  $\Lambda$  of the form

$$\Lambda(\underline{r}, t) = \frac{|\nabla\phi|}{\int_V dV |\nabla\phi|} \int_V dV \left[ (\hat{n} \cdot \nabla)^2 \phi - \frac{2}{W^2}w'(\phi) \right], \quad (3.63)$$

the ‘‘lost’’ material is redistributed along the interface and the global conservation law is restored without any modification of the bulk solutions. Note that this effect comes only into play if the interface shows strong deviations to the correct form, which typically



happens only in the beginning of a simulation. We will call the model described by Eqs. (3.60) and (3.63) the *globally conservative tensorial* or *GCT model*.

Of course, we have to verify that the introduction of the Lagrange parameter does not destroy the valid asymptotic behavior of the model. Any Lagrangian parameter, regardless of its form, disappears from the leading order equation; however, it must still be chosen correctly, because  $\Lambda(\underline{r}, t)$  could contribute to the next-to-leading order equation. Clearly, the parameter disappears from the leading order of the equation; but the interface velocity is determined at next-to leading order, and in general one would expect  $\Lambda(\underline{r}, t)$  to contribute to the equation at that order. This turns out not to be the case and is due to the judicious choice of the form of the parameter, as we shall see now.

The next-to-leading order inner equation can be written

$$(M\partial_{ss} - N) \mathcal{L}\Phi^{(1)} + N \frac{\partial_\rho \Phi^{(0)}}{\int dV \partial_\rho \Phi^{(0)}} \int dV \mathcal{L}\Phi^{(1)} = v_n \partial_\rho \Phi^{(0)} - M\partial_{ss}\kappa \partial_\rho \Phi^{(0)},$$

where we introduced the linear operator  $\mathcal{L} = \partial_{\rho\rho} - 2w''(\Phi^{(0)})$ . The equation contains several terms  $\propto \partial_\rho \Phi^{(0)}$ ; letting  $\mathcal{L}$  act on it leads first to the much simpler equation

$$\mathcal{L}(N - M\partial_{ss}) \mathcal{L}\Phi^{(1)} = 0, \quad (3.64)$$

because  $\mathcal{L}\partial_\rho \Phi^{(0)} = 0$ . Since the the operator  $(N - M\partial_{ss})$  sandwiched by the two  $\mathcal{L}$  is strictly positive, and the operator acting on  $\Phi^{(1)}$  is semipositive, we can conclude that  $\mathcal{L}\Phi^{(1)} = 0$ . Looking at Eq. (3.64), we see that both terms on the left-hand side vanish, meaning that the linear equation is in fact homogeneous and the right-hand side has to vanish as well. This implies

$$v_n = M\partial_{ss}\kappa, \quad (3.65)$$

which is the desired asymptotic result for the interface velocity. It also implies that the Lagrange multiplier is  $O(1)$ , instead of  $O(\xi^{-1})$ , i.e., it is by a factor of the order of  $(\xi\kappa)^2$  smaller than the leading-order terms of the equation. This is the analytical support of what our numerical results already led us to suspect: if the length scales in a simulation are reasonably well separated, the influence of the Lagrange parameter is negligibly small.

### 3.7. The Rätz-Ribalta-Voigt-Model

The only phase-field model for surface diffusion that we found in the literature which does not have the wrong asymptotic behavior of the SM model is the one given by Rätz, Ribalta, and Voigt [99], which we will hence call *RRV model*. Let us briefly discuss the asymptotics of this model. In their simplest form, i.e., for isotropic surface tension and vanishing kinetic coefficient, the model equations read

$$\begin{aligned} \frac{\partial \phi}{\partial t} &= -\nabla \cdot \underline{j}, \\ \underline{j} &= -MB(\phi) \nabla \frac{1}{\xi^2} \tilde{\mu}(\nabla^2 \phi, \phi), \\ \tilde{\mu} &= \frac{1}{g(\phi)} (-\xi^2 \nabla^2 \phi + 2w'(\phi)), \end{aligned} \quad (3.66)$$

with a mobility function  $B(\phi) = 12\phi^2(1-\phi)^2$ , the double-well potential  $w(\phi) = \phi^2(1-\phi)^2$ , and the so-called stabilizing function  $g(\phi) = 10\phi^2(1-\phi)^2$ . Here, we have rescaled the equations from the original publication [99] in order to obtain the same zeroth-order interface profile as in the SM model (with the original equations, the interface would have one third of the width of our profile). The clue is here that the additional singular term  $1/g(\phi)$  in the chemical potential diverges exactly in the right way that in combination with the decay of the mobility function, the dreaded constraint in the spirit of Eq. (3.41) does not exist, and the leading-order inner problem becomes (3.29) again.

At next-to-leading order, we obtain  $\tilde{\mu}^{(1)} = d_2(s)$  (as before), but now the chemical potential function is defined differently – it has a prefactor that diverges in the bulk

$$\tilde{\mu}^{(1)} = \frac{1}{g(\Phi^{(0)})} \left( -\partial_{\rho\rho}\Phi^{(1)} - \kappa\partial_{\rho}\Phi^{(0)} + 2w''(\Phi^{(0)})\Phi^{(1)} \right). \quad (3.67)$$

The first-order term due to variation of the denominator vanishes, as it contains the differential expression from the left hand side of (3.29) as a factor. The numerator of the right hand side of (3.67) goes to zero in the limit  $\rho \rightarrow \pm\infty$  but so does the denominator  $g(\Phi^{(0)})$ ; as a result  $\tilde{\mu}^{(1)}$  remains indefinite, and the degree of freedom necessary for a nonzero value  $d_2(s)$  is introduced into the model. Multiplying the equation by  $g(\Phi^{(0)})\partial_{\rho}\Phi^{(0)}$  and integrating with respect to  $\rho$  over the whole domain, we arrive at  $d_2 = \kappa$ , which is the desired sharp-interface limit (3.4).

It is essential in this model that the mobility function goes to zero far from the interface to suppress diffusion in the bulk, since the chemical potential  $\tilde{\mu}$  varies in the bulk (it behaves as  $d_2(s)$  near the interface).

### 3.8. Conclusion

In this chapter, we have shown that the intuitive way to construct a phase-field model for surface diffusion fails in a subtle way. Just using the chemical potential known from the nonconservative model to define a current, involving its gradient and a mobility that vanishes in the bulk phases, and in taking the divergence of this current as the time derivative of the phase field reproduces only the equilibrium limit correctly. There is a simple argument why the SM model should not be expected to work properly: The chemical potential functional of the model is constructed in such a way that the chemical potential vanishes in the bulk phases. As its diffusion operator is essentially a scalar, diffusion can also act orthogonally to the interface; this effect is most pronounced close to the surface, since the slope of the phase field is largest in the direction perpendicular to the corresponding contour line. This diffusive effect constitutes a driving force for relaxation of the chemical potential towards zero also in the vicinity to the interface (asymptotically, the chemical potential is zero at next-to leading order). Surface diffusion of the chemical potential is then not the only effect contributing to the interface dynamics.

The RRV model introduces a stabilizing function that ensures the correct chemical potential in the interface region, but leads to a diverging chemical potential in the bulk. The absence of diffusion in the bulk is not guaranteed by the chemical potential but by the vanishing mobility. We would like to point out that even though the RRV model

### 3.8. CONCLUSION

---

avoids the mistake of imposing (3.41), it does so by a purely mathematical “trick”, which is the introduction of the stabilizing function  $g(\phi)$ . The models we present, namely the LCT and GCT model, are based on the physical consideration that surface diffusion is an anisotropic process which can be best described with tensorial quantities rather than scalar ones, which is implemented by changing the mobility into a tensor-type quantity. This concept seems naturally suited to the problem at hand, since surface diffusion may be interpreted as highly anisotropic three-dimensional diffusion with a diffusion tensor that has zero eigenvalue in one direction. However, the straightforward tensorial approach also fails, since it does not impose any functional dependence of  $\phi$  in the normal direction of the interface. Modifying the tensorial mobility, we obtain the LCT and GCT models, which both have the correct asymptotic behavior.

## 4. Phase-Field Simulations of Surface Diffusion

Out of the five models that were presented in chapter 3, namely the scalar mobility model (SM), the tensorial model, the locally conserved tensorial model (LCT), the globally conserved tensorial model (GCT) and the Rätz-Ribalta-Voigt model (RRV), only the last three possess the correct sharp-interface limit. Since the numerical impact of these findings is unclear, the next step must be to compare all models numerically. In order not to “compare apples with oranges”, we use the same code for all models, only the method solving the phase-field equation is swapped. Our aim is to compare model behavior, not software implementations, and we are aware of the fact that there might be implementations around that perform better in *absolute* terms, but the *relative* behavior of the models will be unaffected. In contrast to the analytical part, we also include elastic degrees of freedom in order to be able to compare both stable and unstable situations. Essentially, we make four types of comparison:

- First, we determine the maximal admissible time step size at which the algorithms are correct and stable for a given spatial discretization for all models.
- Second, we see how the models deal with a planar profile whose interface was initialized with a slight deviation from the correct profile. This can be important for realistic simulations, when analytical expressions for constant-width profiles at arbitrary curvature and geometric shapes are not readily available (it is already not trivial to give such an expression even for such a simple initial shape as an ellipse). Any simulation code should be robust against these local variations of the profile width and be able to relax the phase-field to the correct interface profile.
- Next, we look at the time evolution of an elliptical inclusion in a solid phase. Since the phase-field is a conserved quantity, the ellipse should morph to a circle with the same area.
- All the previously described situations deal only with a “free” model without any additional degrees of freedom and the time evolution of the interface is due to curvature driven surface diffusion alone. In the last part, we add elasticity as an external force and compare the time evolution of sinusoidal fronts (initialized with the correct width of the profile) for several imposed uniaxial stresses and obtain the linear stability spectrum numerically.

Parts of this chapter have been published in [44].

## 4.1. The Free Model

### 4.1.1. Numerical Stability

The discretization of the SM model is relatively straightforward and poses no particular problems. In the more sophisticated models, some care has to be taken to avoid division by zero. For the RRV model, it has to be ensured that the term  $g(\phi)$  is not set exactly to zero. In the GCT model, one has to compute the normed normal vectors  $\hat{n} = \nabla\phi/|\nabla\phi|$ . The denominator is always positive, but it vanishes far from the interface. It is therefore necessary to set it to be larger than a small positive cutoff number. This is only a question of stability, the numerical results are largely unaffected by the specific choice of the cutoff.

The LCT model poses the most problems, as one has to deal with the situation where  $f(\phi)$  becomes small, as will be discussed at the appropriate place in section 4.1.2.

The first characteristic of the different models to be determined is the relation between the time step size  $\Delta t$  and the grid spacing  $\Delta x$ . Since the model equations are fourth order in space and first order in time and we use straightforward explicit schemes for discretization, a von-Neumann analysis leads to an expected behavior as

$$\Delta t \sim \Delta x^4/M. \quad (4.1)$$

We determined the coefficient for each model numerically by altering the time step for a given grid spacing until oscillations appeared and the calculations broke down. The product of length of the grid  $L$  and lattice parameter  $\Delta x$  was kept constant, so the numerical grid sizes ranged from  $24 \times 24$  to  $600 \times 600$  grid points.

Fig. 4.1 confirms clearly our expectation Eq. (4.1), but it also includes an interesting additional piece of information: while the two scalar models (SM, RRV) allow for about the same maximal time step, the allowed time step size for the tensorial models is considerably larger, up to a factor of ten compared to the scalar models. We would like to point out explicitly that this is a characteristic of the chosen numerical algorithm, and we cannot compare different software implementations, of course. This is why we do not give a specific value for the coefficients, neither numerically nor analytical, as they depend mainly on the chosen discretization scheme which could be subject to change depending on the problem domain. By use of different numerical approaches like adaptive mesh techniques, spectral methods or implicit schemes, the overall running time can of course be reduced by more than this factor; however, the strong nonlinearity of the equations can also present problems for these methods and the increased stability of the tensorial models may persist in this context.

### 4.1.2. Interface Stability

We continue our numerical investigations by checking the interface stability for a planar interface. To do so, we initialize the interface with the wrong profile width and see how fast the interface approaches its correct width. While a planar interface is the worst case scenario for curvature driven surface diffusion, since the curvature simply vanishes, this test is important for realistic simulations. Slight deviations from the correct profile form occur typically when the initial conditions for a complex interface structure are given. Even for such a simple geometrical shape as an ellipse, an analytic expression with the

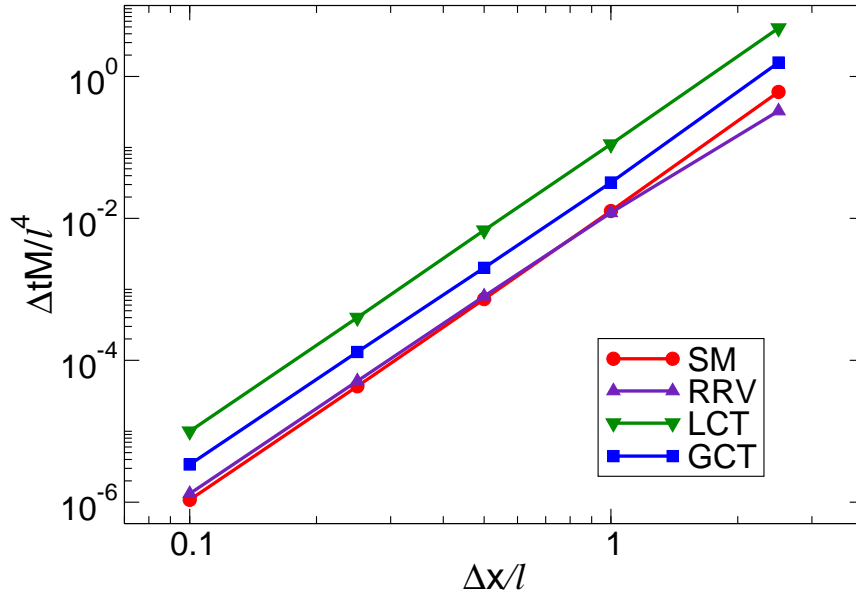


Figure 4.1.: Allowable maximal time step  $\Delta t$  as a function of mesh size, where  $l$  is an arbitrary length unit. Lines are a guide for the eyes only.

correct interface structure everywhere is not readily available. Any phase-field model should be able to deal with these local deviations of the interface and relax to the correct solution.

Since this is a one-dimensional problem, we use a geometry of strips with a length of 200 grid points with Dirichlet boundary conditions and a width of 11 grid points with periodic boundary conditions applied. The grid spacing is related to the interface width via  $\xi = 5\Delta x$ . The interface width  $\xi$  is defined by the stationary solution for the phase-field for the one-dimensional interface

$$\phi = \frac{1}{2} \left( 1 + \tanh \left( \frac{x}{\xi} \right) \right). \quad (4.2)$$

In all plots, only a small section about the interface is shown, and the time  $t$  is given in units of  $\xi^4/M$ . First, we verify that all the models remain in their equilibrium state when initialized with a tanh profile of the correct form. Next, we investigate how the models deal with too narrow interfaces. When comparing the two scalar models, we see that the RRV model (see Fig. 4.5) converges substantially faster to the correct interface profile for a narrow interface of initial width  $0.25\xi$  than the SM model (see Fig. 4.2). However, in our implementation and with the given sets of parameters, simulations with the RRV model broke down if the initial interface width was chosen to be smaller than  $0.23\xi$ . Looking at the results for the tensorial models, we note that the GCT model relaxes much quicker to the correct profile than the LCT model. Comparing the two fast relaxing models RRV and

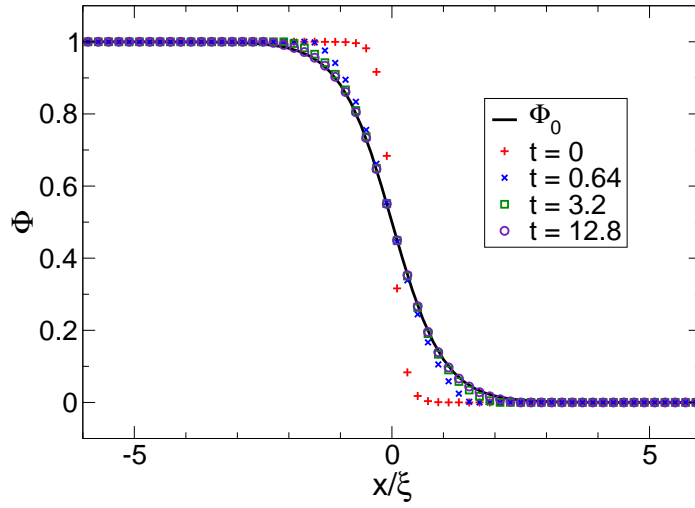


Figure 4.2.: Relaxation towards the correct interface profile for the SM model. The initial interface width is  $0.25 \xi$ , the time  $t$  is given in units of  $\xi^4/M$ .

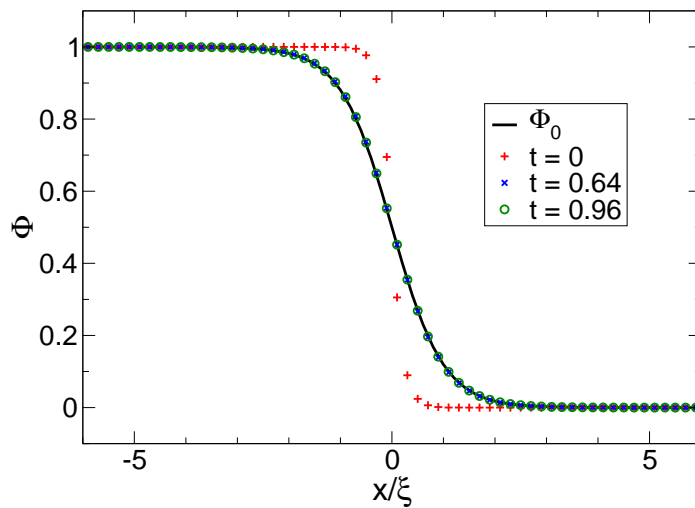


Figure 4.3.: Relaxation towards the correct interface profile for the RRV model. The initial interface width is  $0.25 \xi$ , the time  $t$  is given in units of  $\xi^4/M$ .

GCT, their physical relaxation time is similar, but since the maximal allowable timestep for the GCT model is bigger (see Fig. 4.1), its numerical running time is much shorter.

As we mentioned before, some care has to be taken in the discretization to make the LCT model deal efficiently with too thin interfaces. The reason for this is the underlying asymmetry of the correcting term  $b_0^4$  that was introduced in the model's derivation to enable the model to pick a unique solution. When  $b_0$  approaches zero, then the operator  $\underline{Q}$  reduces to the normal  $\underline{1} - \underline{n} : \underline{n}$  far from the interface. This of course yields the problem of not picking a unique solution for the phase-field, as described for the tensorial model. In fact, the operator  $\underline{Q}$  is constructed in such a way that *close* to the interface, it reduces to  $\underline{1} - \underline{n} : \underline{n}$ , which in turn makes  $\Delta_s \mu = d^2/ds^2 \mu$ . Far from the interface,  $\underline{Q}$  should retain a positive component proportional to  $\underline{n} : \underline{n}$  to keep  $\underline{Q}$  positive semidefinite. Because  $\phi$  is either 1 or 0, this term does not contribute to the surface diffusion. The asymptotic analysis shows that analytically, the term does what it should do *without* any regularisation.

However, numerical problems occur once  $Q^4 = 1 - \hat{n} : \hat{n} + b_0^4 \hat{n} : \hat{n}$  with

$$b_0 = 1 - \frac{\xi^2 (\nabla \phi)^2}{4f(\phi)} \quad (4.3)$$

becomes very large. This happens especially for interfaces that are too narrow, because  $b_0^4$  is then a strongly repulsive function, as can be seen in the following short calculation: we initialize the system with an ‘‘incorrect’’ interface width  $\epsilon$

$$\phi(x) = \frac{1}{2} \left( 1 + \tanh \left( \frac{x}{\epsilon} \right) \right), \quad (4.4)$$

whereas the ‘‘correct’’ interface width is denoted with  $\xi$ . Plugging this and the double-well potential  $f(\phi) = \phi^2(1 - \phi)^2$  into the equation for  $b_0^4$ , we obtain

$$b_0^4(\phi) = \left( 1 - \frac{\xi^2 (\nabla \phi)^2}{4f(\phi)} \right)^4 \approx \frac{(\xi^2 - \epsilon^2)^4}{\epsilon^8} = \frac{1 - \left( \frac{\epsilon}{\xi} \right)^2}{\left( \frac{\epsilon}{\xi} \right)^8}. \quad (4.5)$$

For our chosen parameter for the narrow interface, i.e.  $\epsilon/\xi = 0.25$ , we see that  $b_0^4(0.25) = 50625$ . This large value would impose a prohibitively small timestep (or accuracy in an implicit scheme) for stability if put into the equations of motion. This problem is not present if we initialize with a wider interface, since  $\epsilon/\xi > 1 \Rightarrow b_0^4 \rightarrow 1$ . Cutting off the values for  $b_0^4$  at about  $b_0^4 = 40$  solved the problem in this setup. For production runs, a mixed method, where we relaxed the phase-field with the GCT model first and then used a cutoff value of  $b_0^4 \approx 10$ , proved to be the most practical. The profile then has the correct form and the small cutoff value is sufficient to maintain the correct interface form.

The opposite case, when the initial interface is too wide, also shows some interesting features of the different models, as can be seen in Figs. 4.6 through 4.9. This case proves to be especially hard for the SM model (Figs. 4.6). The profile adapts very slowly to the correct interface form, showing some significant bumps in the phase-field that disappear only gradually. The signature of the wrong initial form remains present even at considerable distances from the interface and can rightfully be expected to affect possible dynamic behavior of the system.



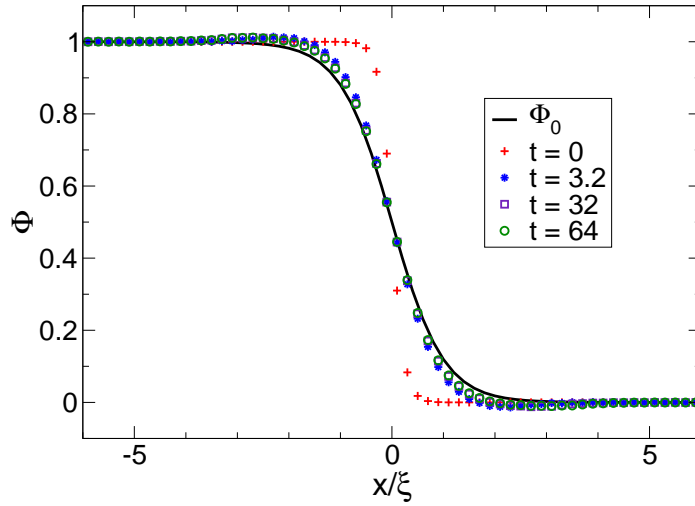


Figure 4.4.: Relaxation towards the correct interface profile for the LCT model. The initial interface width is  $0.25 \xi$ , the time  $t$  is given in units of  $\xi^4/M$ .

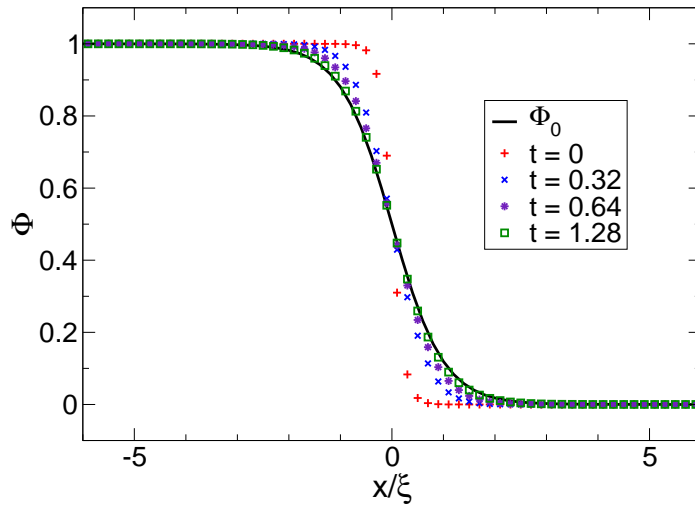


Figure 4.5.: Relaxation towards the correct interface profile for the GCT model. The initial interface width is  $0.25 \xi$ ,  $N = 1.25 M/\xi^2$ , the time  $t$  is given in units of  $\xi^4/M$ .

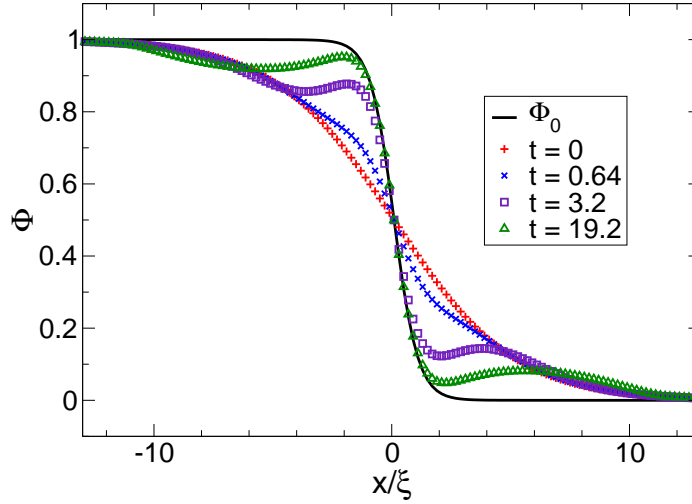


Figure 4.6.: Relaxation towards the correct interface profile for the SM model. The initial interface width is  $5\xi$ , the time  $t$  is given in units of  $\xi^4/M$ . The wide shoulder-like structures show that there is a significant contribution to the diffusion process even far away from the interface (see main text).

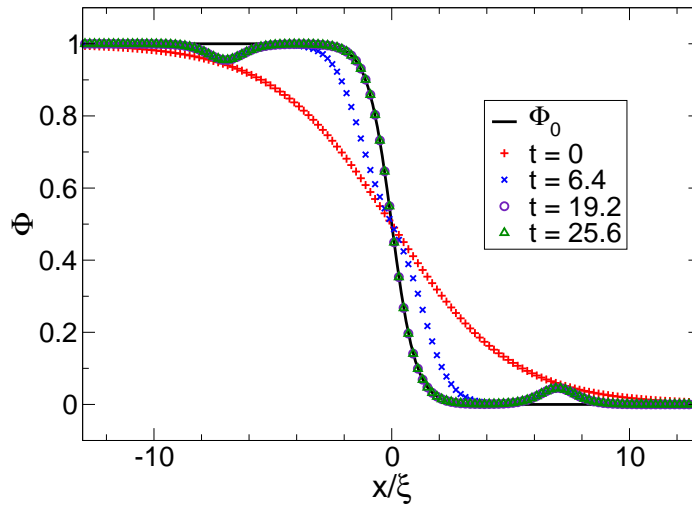


Figure 4.7.: Relaxation towards the correct interface profile for the RRV model. The initial interface width is  $5\xi$ , the time  $t$  is given in units of  $\xi^4/M$ . The small bumps away from the interface are unwanted remnants from the original configuration (see main text).

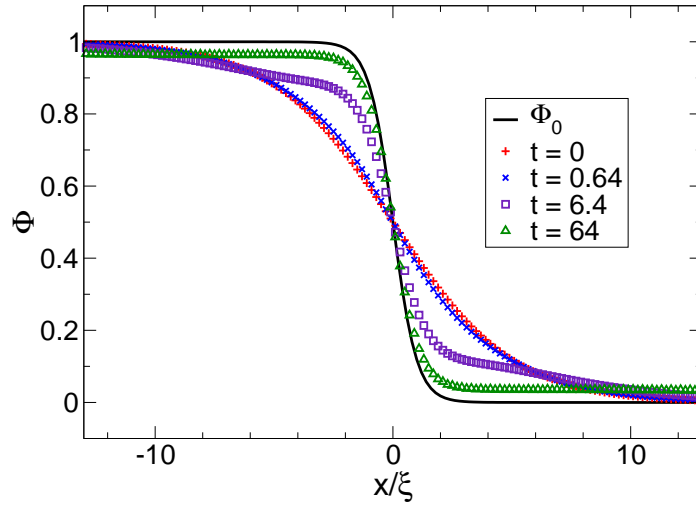


Figure 4.8.: Relaxation towards the correct interface profile for the LCT model. The initial interface width is  $5 \xi$ , the time  $t$  is given in units of  $\xi^4/M$ .

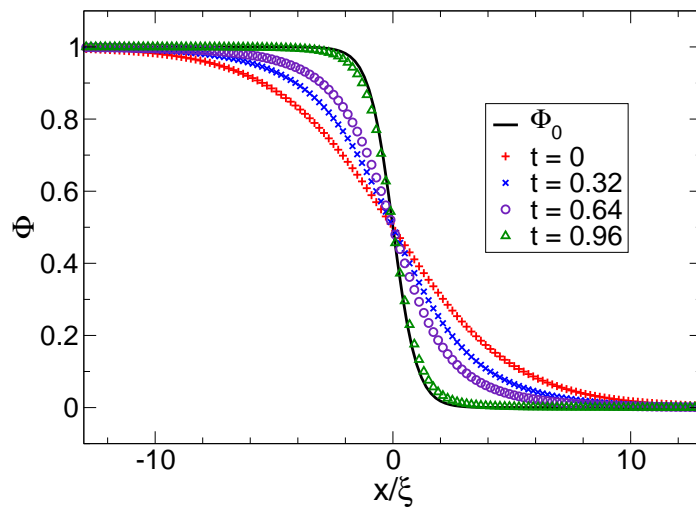


Figure 4.9.: Relaxation towards the correct interface profile for the GCT model. The initial interface width is  $5 \xi$ , the time  $t$  is given in units of  $\xi^4/M$ .

The RRV model goes through a series of transformations of the profile involving as an intermediate state a spatially varying slope in the vicinity of the contour line  $\phi = \frac{1}{2}$  that defines the interface position. These bumps are much more localized than in the SM model, but they are nearly immobile, while the phase-field has already taken its correct form everywhere else. Even after a time of  $t \approx 30 \xi^4/M$ , while near the interface position, the profile is well-behaved and has the right width, there are still indentations in it far from the interface, and these disappear only slowly.

A mixture between the behavior of the two scalar models is exhibited by the LCT model (Figs. 4.8). Convergence is also very slow, even though it always keeps a generally nicer profile. While the area around the contour line  $\phi = \frac{1}{2}$  assumes the correct profile form, the phase-field approaches the wrong bulk values if the boundary values of  $\phi$  are not fixed to be equal to zero or one. This can be seen by looking at Eq. (3.54): any constant value of  $\phi$  satisfies the bulk equations of motion. This incorrect behavior is cured if elastic degrees of freedom are added to the chemical potential. For all geometrical situations where a phase extends to the boundaries of the system, the value of the respective constant is determined by the boundary conditions. Therefore, the model should always be run with Dirichlet boundary conditions for the phase field. For inclusions of one phase in the other, the constant of the inner phase will be preserved by the conservation law if it is correctly initialized to zero or one. This is true for all inclusions with an inner volume much larger than that of the interface and remains true also when elasticity is added to the problem. The simulation from which Figs. 4.8 was obtained used Dirichlet boundary conditions on the right and left end, and we found relaxation to be comparably slow to the SM and RRV models but the interface profile to look more reasonable.

The reason that the models have such a problem with wide interfaces is due to the fact that correcting the profile width requires diffusion perpendicular to the interface which is suppressed in the asymptotic limit. The GCT model was designed to cope well with situations like these, since the additional term breaks conservation on the scale where the phase-field varies strongly. Therefore, for  $N = 1.25M/\xi$  it relaxes very quickly to the correct profile form, as can be seen in Fig. 4.9. Also, the results were not altered if run with or without the Lagrange parameter term for global conservation.

So we can draw the following conclusion: whenever interface thickness is expected to be an issue, the slight violation of conservation in the GCT model proves to be more of a virtue than a drawback. This is always the case when analytic formulas to initialize the desired geometry are not at hand or when surface tension anisotropy is included in the model. In these cases, diffusion perpendicular to the interface is required, a process that is very slow in the other models and asymptotically suppressed. For production runs, we often found it convenient to have a short relaxation phase using the GCT model before the actual dynamics with another model were started.

### 4.1.3. Elliptical Inclusions

The next, more "real-life" problem under investigation is the behavior of an elliptical inclusion.

Since the surface diffusion process is driven by curvature and the amount of each phase

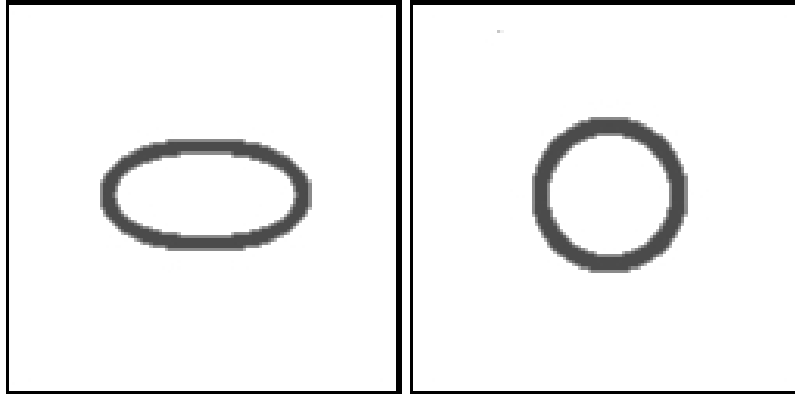


Figure 4.10.: Initial and final configuration of an elliptical inclusion. The surface diffusion process is solely driven by curvature. The initial ellipse and the final circle have the same area.

is conserved, material diffuses in such a way that the overall curvature is reduced: the ellipse morphs into a circle of the same area. In the shown simulations (see Fig. 4.10), we initialize the system with a sharp interface ellipse with a semimajor  $a_0$  and a semiminor  $a_0/2$ . This ellipse is then relaxed for a few steps with the GCT model to ensure a correct local interface profile everywhere. We then switch to the model we want to investigate and monitor the evolution of the semimajor and semiminor axis of the ellipse. The results for such a run are shown in Fig. 4.11.

The three models with correct asymptotic behavior all converge to a circle with the correct radius  $\sqrt{2}a_0/2$ . Only the SM model behaves differently: the radius of the circle is too small and decreases further. Since the phase-field conservation is fulfilled for our code, which we also checked numerically, this can only mean that the final shape is not a real circle. A slight level of anisotropy must be present in the system that distorts the circle. In order to understand this behavior better, we improved the scale separation by increasing the size of the system and the included ellipse while keeping the interface width constant. The increased scale separation improves the results in case of the SM model asymptotically, as can be seen in Fig. 4.12.

The results for the LCT model serve as comparison here. Performing an analogous scale separation for the other models, see Fig. 4.13, all curves collapse onto a single line; improved scale separation does not alter the behavior and the dynamics are quantitatively correct even for moderate system sizes.

## 4.2. Surface Diffusion with Elastic Effects

### 4.2.1. Elliptical Inclusions with Elasticity

Coupling elasticity to the model we treated so far can be achieved by replacing the "free" chemical potential  $\tilde{\mu}$  with one that includes the correct elastic energy contribution. In

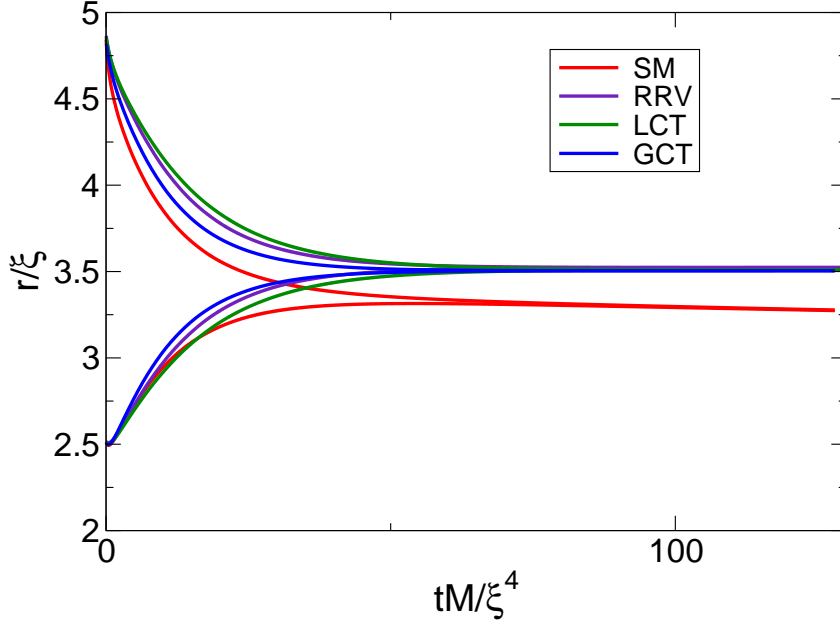


Figure 4.11.: Comparison of the time development of the size of an elliptical inclusion. The square system had the length  $L/\xi = 20$ . The initial ellipse had a semimajor of  $a_0 = L/4$  and a semiminor of  $L/8$ . All models except the SM-model converge to circles with the same radius  $r$ .

particular, we set

$$\tilde{\mu}(\nabla^2\phi, \phi) = -\xi^2\nabla^2\phi + 2w'(\phi) + \frac{\xi}{3\gamma}h'(\phi)V_{el}, \quad (4.6)$$

with an elastic energy of

$$V_{el} = G(\phi)\epsilon_{ij}^2 + \frac{1}{2}\lambda(\phi)\epsilon_{ii}^2, \quad (4.7)$$

with the phase-dependent shear modulus

$$G(\phi) = h(\phi)G^{(1)} + (1 - h(\phi))G^{(2)} \quad (4.8)$$

and Lamé constant

$$\lambda(\phi) = h(\phi)\lambda^{(1)} + (1 - h(\phi))\lambda^{(2)} \quad (4.9)$$

where the superscripts denote the bulk values of the phases 1 and 2 and the function  $h(\phi) = \phi^2(3 - 2\phi)$  interpolates between the phases.  $w(\phi) = \phi^2(1 - \phi)^2$  is the double well potential, and the strain tensor is  $\epsilon_{ij} = (\partial_i u_j + \partial_j u_i)/2$ , where  $u_i$  denotes the displacement field. The strain-stress relation is given by Hooke's law (2.30). In order to calculate the

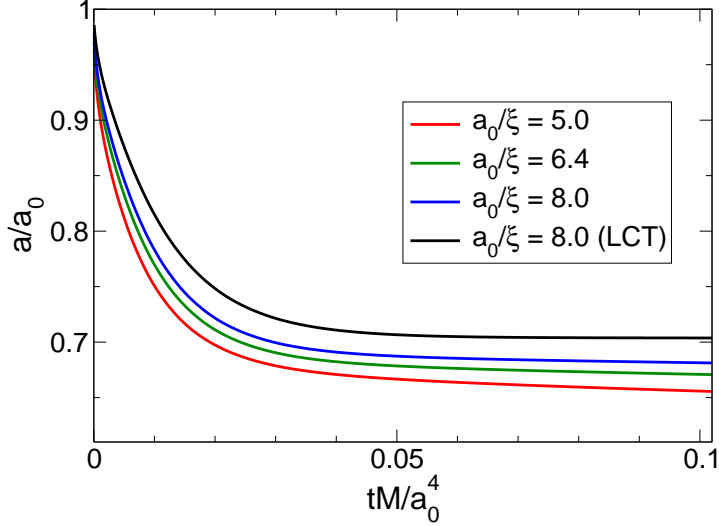


Figure 4.12.: Elliptical inclusion: comparison of the time development of the length of the semimajor  $a$ . The initial length is denoted by  $a_0$  and the different curves correspond to different scale separations  $a_0/\xi$ . The performance of the SM-model becomes asymptotically better for larger systems. Results for the LCT-model have been included as a reference.

stresses needed in Eq. (4.6), one has to solve the elastic equations, given by the mechanical equilibrium condition of a vanishing divergence of the stress tensor

$$\sum_j \frac{\partial \tilde{\sigma}_{ij}}{\partial x_j} = 0, \quad \tilde{\sigma}_{ij} = h(\phi) \sigma_{ij}^{(1)} + (1 - h(\phi)) \sigma_{ij}^{(2)}, \quad (4.10)$$

here in the static limit of elasticity. The dimensionless driving force is given by

$$F = \frac{\delta^2(\lambda + 2G)}{4\gamma L}. \quad (4.11)$$

The case of  $F = 0$  corresponds to the free model without elasticity, which we have treated in the previous sections. For driving forces  $F > 1$ , the elastic influence leads to a growth of the elliptical cavity, as is shown in Fig. 4.14.

Depending on how one chooses the elastic constants in the soft phase, different situations can be treated. Setting  $G^{(2)} = 0$  corresponds to modeling the inner phase as a liquid. Setting both  $G^{(2)}$  and  $\lambda^{(2)}$  to zero corresponds to effectively having an elastic vacuum as second phase, and we have diffusion along a free interface. That modeling a liquid or vacuum as a shear free solid does indeed capture the correct physics of the system has been shown in [69].

In general, the boundary conditions at the interface between the two phases are

$$\sigma_{in}^{(1)} = \sigma_{in}^{(2)} \quad (4.12)$$

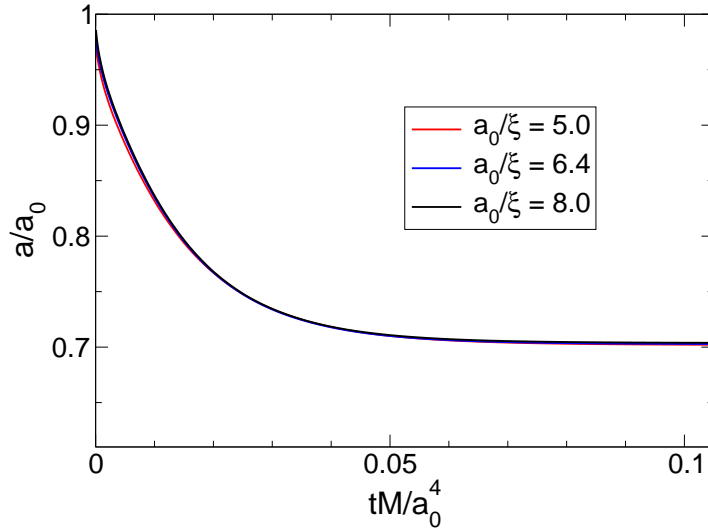


Figure 4.13.: Elliptical inclusion: comparison of the time development of the length of the semimajor  $a$  for the LCT-model. The initial length is denoted by  $a_0$  and the different curves correspond to different scale separations  $a_0/\xi$ . All curves collapse onto a single line.

(continuity of normal and shear stresses), but we choose them more specifically to be

$$\sigma_{nn} = -p = 0, \quad \sigma_{nt_1} = \sigma_{nt_2} = 0 \quad (4.13)$$

which means that the normal component of the stress is equal to the negative external pressure, while its shear components along two independent tangents  $\underline{t}_1$  and  $\underline{t}_2$  vanish.

The introduction of the elastic degrees of freedom motivates the introduction of a staggered grid where mass densities and elastic constants are defined on the grid points and the displacements between them. For simplicity, we use an explicit forward time algorithm on a homogeneous staggered grid for solving both the elastic and the phase field equations. For details, we refer to the appendix A.5. At each iteration, the following steps are performed:

- First, the elastic equation is solved, where the phase field values are given as parameters.
- The second step consists of calculating the chemical potential for each grid point, given the updated elastic values.
- Finally, the new values for the phase field are calculated and the next iteration starts.

This operator splitting approach enables us to use identical methods for the first two steps for all four models, while their difference appears only in the last step.



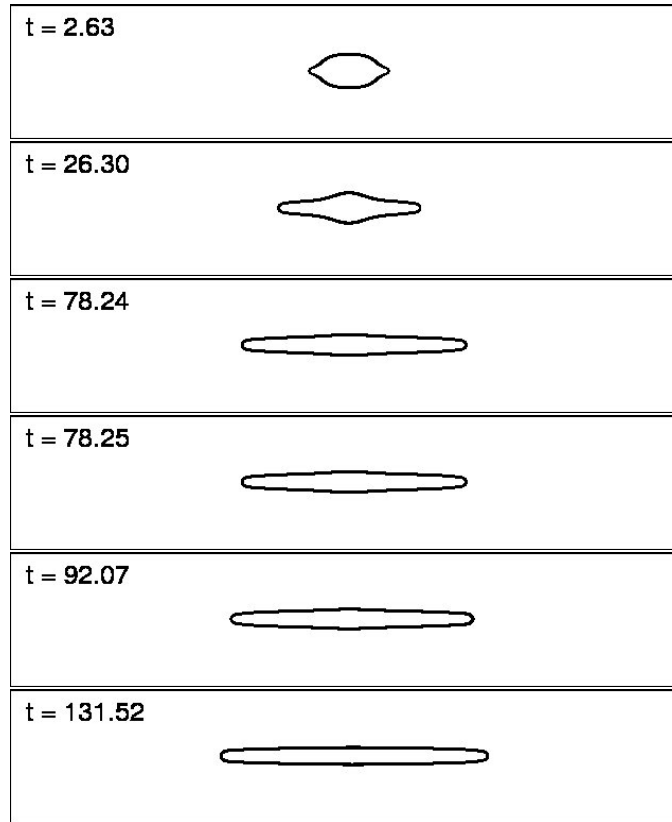


Figure 4.14.: Time evolution of an elliptical inclusion with external elastic loading. The simulations were performed with the GCT model. The shorter side of the system had the size  $L/\xi = 25.6$ , the aspect ratio of the system was 4 : 1, the elastic driving force  $F = 4$  and the initial aspect ratio of the ellipse was 2 : 1. The dimensionless time is given in the same units of  $M/\xi^4$  as before.

The code we developed includes the fully time-dependent dynamic elasticity as will be shown in chapter 5. But since we investigate the beginning of the Grinfeld instability, the observed interface velocities are very small in comparison to the speed of sound, and the equations effectively reduce to the static elastic case of Eq. (4.10).

#### 4.2.2. Quantitative Analysis of the Grinfeld Instability

After these investigations, which concentrated on the surface diffusion part alone, we now add elasticity to the game. The physical setup consists of a slightly perturbed planar phase boundary between a hard and a soft phase in a strip geometry. The perturbation is sinusoidal and the behavior of the system depends on the elastic influence. If no or only weak external elastic loading is applied, the curvature drives the diffusion process and the perturbation gradually disappears. If the external loading is larger than the critical loading, the Grinfeld instability sets in, because the system can reduce its stored elastic energy by forming deep groves and crack-like structures. This setup is particularly

interesting, since the Grinfeld instability is one of the few problems where an analytical solution is available that we can compare our numerical results against.

We look at a square system of length  $L$  with a uniform grid spacing  $\Delta x$ . The phase-field interface width is chosen to be  $\xi = 5\Delta x$ . Remember that this is a purely numerical parameter. The elastic loading is applied by stretching the top end of the strip by a fixed displacement  $\delta$  in direction perpendicular to the normal of the unperturbed interface.

The perturbed surface is given by  $\delta x(z) = A_0 \sin(kz)$  with the small amplitude  $A_0 k = \pi/20$  and a wave number of  $kL = 4\pi$ . Since the good separation of the length scale of the interface width  $\xi$  and the characteristic wavelength is paramount, we use  $k\xi = 0.16$ . The imposed uniaxial stress is given in the figure caption for each case. As we have already determined the maximum admissible time step, see section 4.1.1, we chose simulation time steps of  $\Delta t = 5 \cdot 10^{-4}(\Delta x)^4/M$  for the scalar models and  $\Delta t = 5 \cdot 10^{-3}(\Delta x)^4/M$  for the tensorial models, which are safely below the stability threshold. The Poisson ratio is chosen to be  $\nu = \lambda/[2(\lambda + G)] = 1/3$ . For the GCT model, the constant in front of the nonconserved term is  $N = 1.25M/\xi^2$ . For the SM model, the mobility is chosen to be the standard  $\tilde{M}(\phi) = 36M\phi^2(1 - \phi)^2$ . To minimize the influence of the boundaries, we use helical boundary conditions in the  $z$ -direction for the displacement fields at the upper boundary, i.e.  $u_z(x, L) = u_z(x, 0) + \delta$  and periodic boundary conditions  $u_x(x, L) = u_x(x, 0)$ , while the boundary conditions at the bottom are sufficiently determined by a vanishing derivative in  $z$ -direction. The left and right boundary conditions are given by  $u_z(0, z) = u_z(L, z) = z \cdot \delta/L$  and  $u_x(0, z) = u_x(L, z) = 0$ . Applying these boundary conditions, we obtain a homogeneously strained state for the flat interface in both phases.

The resulting strain is given by

$$\epsilon_0 = \frac{\delta}{L} \quad (4.14)$$

Using the condition for uniaxial stress  $\sigma_0 = \sigma_{zz}$  and Hooke's law, we obtain

$$\sigma_0 = \frac{E\delta}{(1 - \nu^2)L} \quad (4.15)$$

Starting from the definition of the Grinfeld length Eq. (2.90) and using Eq. (4.15), the Grinfeld length has the form

$$L_G = \frac{\gamma(1 - \nu^2)L^2}{2E\delta^2}. \quad (4.16)$$

We can now define a dimensionless driving force

$$F_G = \frac{1}{kL_G} \quad (4.17)$$

Please note that the definition of the driving force for the Grinfeld instability Eq. (4.17) differs from the driving force Eq. (4.11) defined for the elliptical case. This is due to the different geometrical setup and elastic state of the system. The conversion factor between the driving forces is given by

$$\frac{F_G}{F_C} = \frac{2(1 - 2\nu)}{\pi(1 - \nu)^2} \quad (4.18)$$

## 4.2. SURFACE DIFFUSION WITH ELASTIC EFFECTS

In Figs. 4.15 to 4.17, we show the temporal evolution of a sine profile starting with a prescribed amplitude for different values of the imposed uniaxial stress. The four models are compared directly with the sharp interface prediction resulting from Eq. (4.23). Fig. 4.15 corresponds to the stress-free case that we discussed analytically.

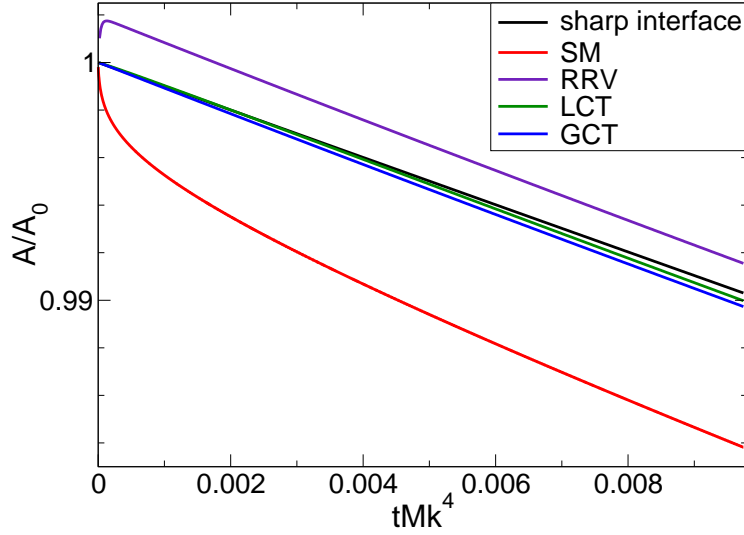


Figure 4.15.: Amplitude evolution for a uniaxial stress of  $F = 0$ , i.e., a Griffith length  $L_G = \infty$ .

All the situations considered correspond to either weak decay or weak growth of the amplitude, as the expected exponential behavior still appears linear on the considered time scale.

The dispersion relation for a system under uniaxial stress  $\sigma_0 = \sigma_{zz}$  parallel to the initially flat interface is [119]

$$\omega = \frac{M}{\gamma} \left( 2 \frac{1 - \nu^2}{E} \sigma_0^2 k^3 - \gamma k^4 \right), \quad (4.19)$$

i.e., it has an increasing cubic and a decreasing quartic piece.

Using the relations

$$\begin{aligned} \epsilon_{0,zz} &= 2 \sqrt{\frac{\gamma F}{(\lambda + 2\mu)}} L \\ \sigma_{0,zz} &= \frac{\epsilon_{0,zz} E}{1 - \nu^2}, \end{aligned} \quad (4.20)$$

expressing  $\mu$  and  $\lambda$  in terms of  $\nu$  and  $E$  and defining the Grinfeld-Length  $L_G$

$$L_G = \frac{L(1 - \nu)^2}{8F(1 - 2\nu)}, \quad (4.21)$$

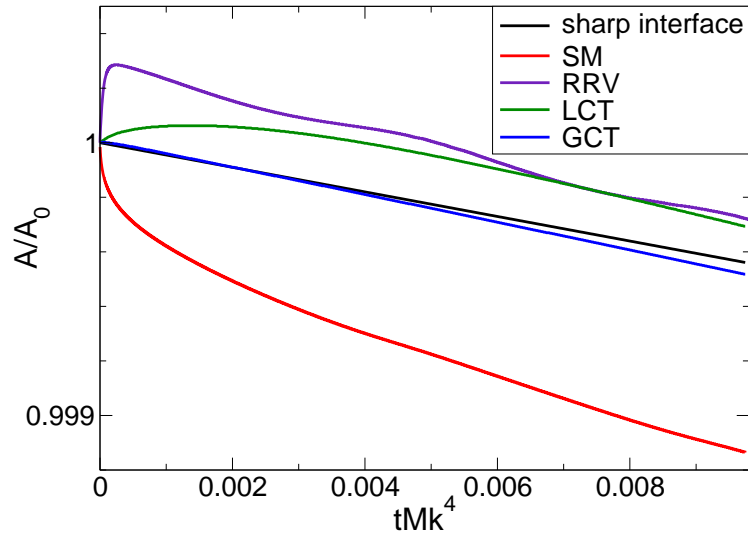


Figure 4.16.: Amplitude evolution for a uniaxial stress of  $F = 0.955$ .

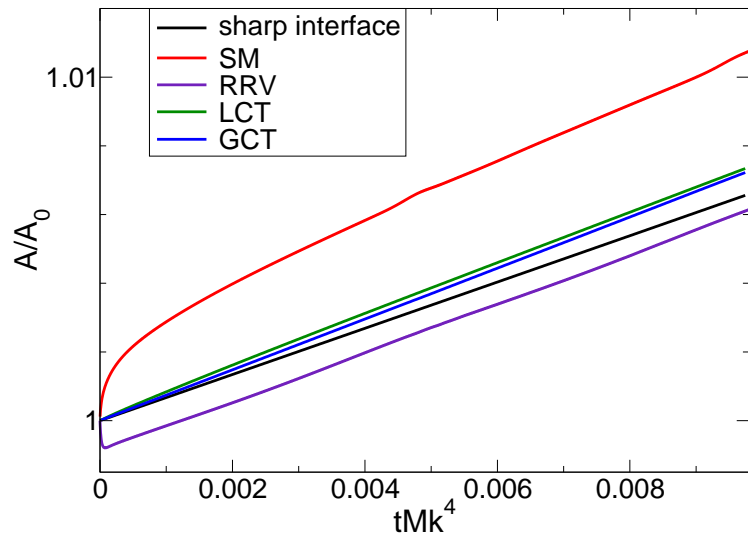


Figure 4.17.: Amplitude evolution for a uniaxial stress of  $F = 1.67$ .

we can write the dispersion relation, i.e., the spectrum of the linear stability operator, as follows

$$\omega = M \left( \frac{k^3}{L_G} - k^4 \right), \quad (4.22)$$

meaning that we have unstable modes at small  $k$  ( $k < 1/L_G$ ) and stable ones at large  $k$  ( $k > 1/L_G$ ). We typical way of plotting the spectrum is

$$\frac{\omega L_G^4}{M} = (kL_G)^3 - (kL_G)^4, \quad (4.23)$$

and the obtained spectrum for all four models can be seen in Fig. 4.19. To obtain the spectrum numerically, we vary the parameter  $L_G$  in the simulations.

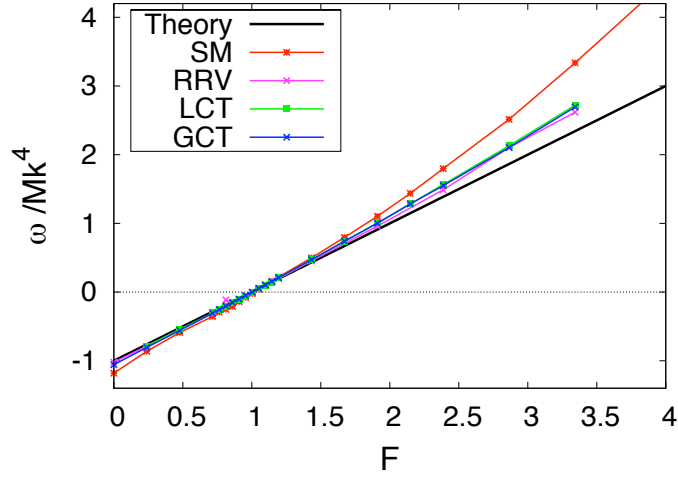


Figure 4.18.: Wave length as function of the driving force. The SM model shows the largest deviations from the theoretical expectation Eq. (4.22). The other models, while slightly deviating for large driving forces, show similar behavior.

We note that all the models agree with the predicted behavior of the sharp-interface limit to within better than one percent for our parameters and time span. While it may be observed unambiguously that the SM model displays the largest deviation from the desired result, one may find it surprising that it reproduces the limit so well after all, taking into account that it does not have the right asymptotics. This may be due to the fact that the equations of the asymptotic behavior to which the system can adjust locally act as an attractor for the dynamics even before the full set of equations, implying more global restrictions such as Eq. (3.43), becomes active. It is striking that this seems to work even in a growth situation, where interface velocities increase on average.

Fig. 4.19 gives a comparison of the linear stability spectra, obtained by simulation of the four models, with the analytical expression Eq. (4.23) of the sharp-interface model. It

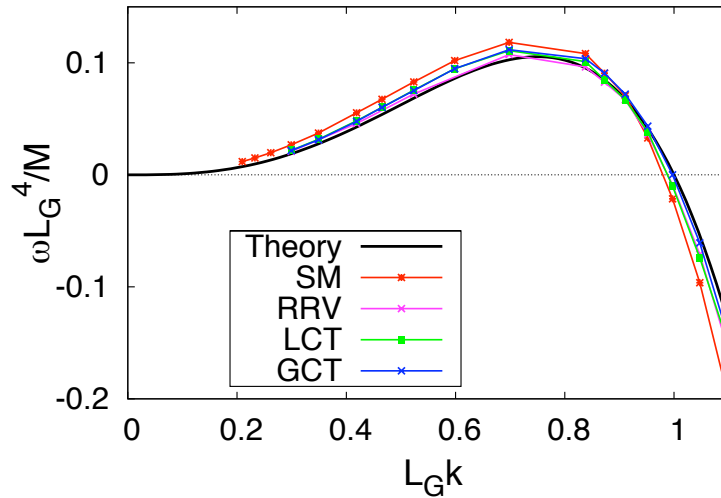


Figure 4.19.: Full spectrum of the ATG instability.

is pretty clear that the SM model is farthest off the correct value both below and above the fastest-growing wavenumber. The LCT model is good for wavenumbers above that of the fastest-growing mode but shows stronger deviations than both the RRV and GCT model below that mode. The latter two models are about equally close to the correct spectrum throughout the whole wavenumber domain.

### 4.3. Conclusion

In this chapter, we conducted a careful numerical study, comparing similar implementations of all models derived in chapter 3 for several different cases. The systems we simulated included both, the free models, where the surface diffusion process was driven by curvature alone, and the models coupled to elastic degrees of freedom.

Surprisingly enough, the SM models does not fail altogether numerically for dynamic cases, but produces visibly by far the least precise results. Since the SM model constitutes an uncontrolled approximation, we strongly advise against using it for quantitative analysis. The other models indeed faithfully capture the correct asymptotic behavior, while also being more efficient at the same time.

The tensorial models LCT and GCT allow for larger rougher discretization, since once the phase-field profile is represented with an error of order  $\xi$  or better, their effective leading order is only one order lower than the one determining the interface velocity. This means that the restriction on the grid spacings is weaker, scaling with  $\xi$  instead of  $\xi^2$ .

The LCT model is most efficient in suppressing diffusion perpendicular to the interface. In the course of well initialized simulations, variations of the interface profile width occur only gradually through curvature changes. In this case, one could expect that the surface diffusion process *along* the interface is efficient enough to maintain the correct interface

### 4.3. CONCLUSION

---

structure. Nevertheless, the numerical robustness of the LCT model is reduced by its strong preference for pure tangential material transport.

The GCT model, even though breaking strict local conservation, is very accurate and by its setup numerically extremely robust. Since it combines the favorable efficiency of a tensorial approach with accuracy, robustness and ease of implementation, it is our model of choice for most of the more complex cases. Since this model handles even sharp initializations well and relaxes the phase-field reliably and quickly to the correct form, we used it to prepare the phase-field for the other models in cases where no global analytic expression for the phase-field is available. Note that this is already the case for the elliptical inclusions.

The simulations of elliptical inclusion under elastic stress illustrate that crack propagation by surface diffusion is indeed possible. In order to gain quantitative insight into what numerical precision can be expected from all models for the dynamics of the interface with elastic effects, the early stage of the Grinfeld instability was analyzed. While again the SM model performed surprisingly well, it exhibited by far the largest deviation from the theoretical expectation. All other models perform show equally good precision.

So we conclude that despite the fact that strict local conservation is dropped in the GCT model, in contrast to the RRV and LCT model, which are strictly conservative, this is by far outweighed by the advantage of higher robustness, making it our preferred model for novel applications.

## 5. Fast Crack Propagation with Phase-Transformation Kinetics

In this chapter, we present a continuum model that describes crack propagation as the result of an elastically induced phase transition between two coherent phases. Like the models in chapter 3, this model is not build around any specific assumptions about cracks, but is based solely on well known and established concepts that proved to be successful in the context of pattern formation processes. The theory is based on the continuum description of solids, including linear theory of elasticity, that does not contain any atomic length-scales; the competition between the surface energy as a stabilizing force and the elastic energy as a driving force; and finally standard non-equilibrium kinetics. While also applicable to other situations like solid-solid-transformations, this model can be used to describe fracture on the basis of the late stage of the Asaro-Tiller-Grinfeld instability [3, 43], see section 2.4, if one of the phases is modeled to have vanishing elastic constants. We will see that the deep notches that form do look and behave like cracks in many aspects.

Experimental results show that many features of crack growth are rather generic [76, 36, 100, 104, 105]; among them is the saturation of the steady state velocity appreciably below the Rayleigh speed and a tip splitting for high applied tension and at speeds of roughly  $0.8v_R$ .

In our approach, we treat the propagating crack as a free moving boundary problem. The phase-field method has emerged as a powerful simulation tool to describe the complex dynamics of interfaces without having to track these interfaces explicitly. The price to be paid is that the phase-field formulation introduces an additional length scale  $\xi$  that is not present in the original sharp interface problem. If the sharp interface equations are known, as is the case for both the surface diffusion and the phase transition model, it has to be ensured that the used phase-field model converges to these desired sharp interface equations asymptotically. While the phase transition model is not plagued by the subtle, but fundamental problems that were encountered when modeling surface diffusion, the existence of the additional length scale  $\xi$  still has considerable impact on the results. One aim of this chapter is to show how quantitatively reliable results can be obtained which are not influenced by finite-size effects.

In chapters 3 and 4, we assumed that material diffused along the interface, leading to mass conservation of each phase. Of course, surface diffusion is not the only process that can be used to set up macroscopic descriptions of interface propagation, and many phase-field investigations of the elastically driven Grinfeld instability have considered a nonconserved phase-field [81, 68, 69, 45]. In these models, a particle reservoir is provided by either the melt that is in contact with the solid or the adatom phase on a vicinal surface. This predilection for phase-transition models, either on the basis of a sharp-interface model or using a phase-field, has different reasons: first, it is easier to write



down a nonconservative model than a conservative one, as will be shown in this chapter. Second, the equation of motion for the surface diffusion process Eq. (3.4) are of high order due to the appearance of the surface Laplacian, making the simulation computationally expensive, see also Fig. 4.1. In addition, no asymptotically correct phase-field models for surface diffusion were available until the publication of [99] and our work [44].

The choice of modeling crack propagation as a phase transition process is therefore also motivated by practical reasons: using a nonconserved phase-field parameter and having a local interface velocity that spares the derivatives simplifies the phase-field modeling and reduces computational time while the same selection principles apply as with surface diffusion.

Since we concentrated on the early stage of the Grinfeld instability in chapter 4, where tip velocities are still low, dynamical effects were not crucially important. This is no longer true for the results presented in this chapter, where we investigate fast crack propagation. As we explain in Section (5.2), including dynamic effects cures the unphysical finite time cusp singularity of the Grinfeld instability and allows for a fully self-consistent, simultaneous selection of both, crack shape with finite tip radius and the propagation velocity, which renders the free moving boundary approach possible.

We will proceed as follows: We start with presenting the sharp interface formulation of the model, containing the elastic equations and the dissipative interface kinetics. We then explain how dynamic elasticity provides a new the scale selection mechanism, which equally applies to phase transition and surface diffusion processes. Next, in Section 5.2.1, the multipole expansion method [97] will be shortly described, which can be used to solve the sharp interface equations in the specific parameter regime of steady state growth. Since the multipole expansion method cannot resolve the whole parameter regime and therefore leaves open questions, phase-field simulations with the same underlying sharp interface model are performed. They serve as an independent, complimentary approach that allows to investigate the hitherto inaccessible parameter ranges, because the phase-field model does not need to rely on the underlying analytical assumptions of the multipole expansion method. We point out that it is crucial to eliminate the inherent finite-size-effects of the phase-field calculations to obtain good quantitative results. To this end, large scale simulations and a careful extrapolation procedure are necessary. As we will show, the results of the two numerical techniques that are, apart from being based on the same sharp interface equations, totally independent methods to solve the free moving boundary problem at hand, agree very well in the overlapping parameter regime.

Parts of this chapter have been published in [96], [110] and [111].

## 5.1. Sharp Interface Equations

For any macroscopic description of free moving boundaries, like given by an advancing crack, some material transport mechanism is necessary. In contrast to the previous chapters 3 and 4, where we assumed that transport is due to surface diffusion, we concentrate on a phase transformation process as material transport mechanism.

The model description starts with the assumption that the crack shape is given by the boundary between two different phases, an outer solid matrix that breaks, and an inner,

already “broken” phase. Each of these phases is characterized by their respective effective material constants and a chemical potential  $\mu$ . Analog to the surface diffusion case, if the motion of the interface is only driven by curvature, the local chemical potential difference between the solid and the broken phase can be written as

$$\mu_{surf} = \frac{1}{\rho_s} \gamma \kappa, \quad (5.1)$$

where  $\rho_s$  is the density of the solid phase,  $\gamma$  the (isotropic) surface tension and  $\kappa$  the curvature. A positive curvature corresponds to a locally convex solid phase, a negative one to a locally concave solid. We now add elasticity to the description. Since the surface

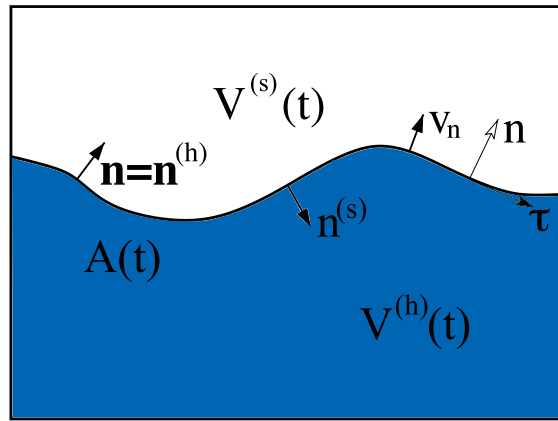


Figure 5.1.: Geometry of the phase transition scenario. Phase transitions between phases 1 and 2 are possible and lead to interface motion with local normal velocity  $v_n$ . The volumes of the two phases and the interface  $A(t)$  are therefore time-dependent.

energy does not couple to the elastic terms, the chemical potential consists of two parts,

$$\mu = -\mu_{surf} + (\mu_{el}^{(h)} - \mu_{el}^{(s)}) = -\mu_{surf} + \mu_{el} \quad (5.2)$$

where the second term (in brackets), which we will now call  $\mu_{el}$ , contains the elastic effects.

The influence of surface energy and the external elastic field lead to a non-equilibrium situation and consequently to interface movement. We interpret the fracture process as a first order phase transition now, where the outer solid phase turns into a “broken phase” due to elastic effects. If the phase that makes up the interior of the crack is assumed to have vanishing elastic constants, so it does not support any stresses, it behaves like an elastic vacuum and crack propagation can be studied. A central simplification of the theory consists of assuming that both phases have the same mass density  $\rho$ , so the inner phase resembles a dense gas.

The next needed ingredient in the formulation of a macroscopic sharp interface model is a dynamical law of motion that describes the local interface velocity as function of the chemical potential. In the phase transformation description, a particle reservoir is present, and for a rough interface, it is natural to assume linear nonequilibrium kinetics.

## 5.1. SHARP INTERFACE EQUATIONS

---

The driving force is then the chemical potential difference itself, and the normal velocity of the interface  $v_n$  will simply be proportional to it:

$$v_n = -\frac{D\rho_s}{\gamma}(\mu_{surf} - \mu_{el}), \quad (5.3)$$

where  $D$  is a kinetic coefficient with dimension  $[D] = \text{m}^2/\text{s}$ , and the interface normal points from the solid into the softer phase, as shown in Fig. 5.1. Eqs. (5.2) and (5.3) tell us that the planar interface is energetically stable as any solid protrusion leads to growth of the liquid phase and liquid protrusion leads to a concave bump and consequently, the solid phase grows while the liquid phase shrinks. Independent of whether the external loading is compressive or tensile, the elastic contribution to the chemical potential is always positive and favors growth of the vacuum phase. This model has *nonconservative* interface dynamics, and the solid part of the system serves as a particle reservoir for the crack. That this kind of modeling captures the essential relevant physics of the real system has been shown in [68].

All following relations can be obtained in a consistent way from variational principles, and this is described in detail in Appendix A.1. In the bulk, the elastic displacements have to fulfill Newton's equation of dynamic elasticity

$$\frac{\partial \sigma_{ik}^{(\alpha)}}{\partial x_k} = \rho \ddot{u}_i,$$

which applies in each phase  $\alpha$ . The elastic contribution to the chemical potential at a coherent interface for each phase is generally given by [108]

$$\mu_{el}^{(\alpha)} = \left( \frac{1}{2} \sigma_{\tau\tau}^{(\alpha)} \epsilon_{\tau\tau}^{(\alpha)} - \frac{1}{2} \sigma_{nn}^{(\alpha)} \epsilon_{nn}^{(\alpha)} - \sigma_{n\tau}^{(\alpha)} \epsilon_{n\tau}^{(\alpha)} \right). \quad (5.4)$$

The condition of coherency at the interface implies that the displacement field  $u_i$  is continuous across the phase boundary,

$$u_i^{(h)} = u_i^{(s)}. \quad (5.5)$$

Since the soft phase is modeled as an elastic vacuum, both normal and shear stresses are not only continuous across the interface, but due to the vanishing elastic constant in the soft phase, we have

$$\sigma_{nn}^\alpha = \sigma_{n\tau}^\alpha = 0, \quad (5.6)$$

where the indices  $n$  and  $\tau$  define a local orthogonal frame of reference with  $n$  denoting the normal direction of the interface and  $\tau$  the perpendicular tangential direction (see Fig. 5.1) and where the upper index indicates the phase.

The material in each phase is assumed to be homogeneous and isotropic and we concentrate on a two-dimensional plane-strain situation, so according to chapter 2.1.5, the relation between the strain tensor

$$\epsilon_{ik}^{(\alpha)} = \frac{1}{2} \left( \frac{\partial u_i^{(\alpha)}}{\partial x_k} + \frac{\partial u_k^{(\alpha)}}{\partial x_i} \right)$$

and the stress tensor is given by Hooke's law

$$\sigma_{ij}^{(\alpha)} = \frac{E^{(\alpha)}}{1 + \nu^{(\alpha)}} \left( \epsilon_{ij}^{(\alpha)} + \frac{\nu^{(\alpha)}}{1 - 2\nu^{(\alpha)}} \delta_{ij} \epsilon_{ll}^{(\alpha)} \right)$$

for each phase, where  $E$  and  $\nu$  denote elastic modulus and Poisson ratio, respectively. Here, we do not include eigenstrain contributions due to different unit cells of the phases, but they can easily be introduced [14].

At this point, the assumptions of equal mass density and coherency lead to a significant simplification, because if they are not fulfilled, the relations for momentum conservation are more complicated and also contain the normal velocity  $v_n$  of the interface [37]. Of course, it would be desirable to have a true vacuum inside the crack, but curing the problem of mass loss would require a strain dependent density  $\rho(\epsilon)$ . This is beyond the standard theory of linear elasticity, where such dependencies are not included.

The mass density equality of the two phases has another important implication: there are no kinetic energy contributions of the form  $\rho \dot{u}_i^2$  to the chemical potential, since such contributions are continuous across the interface. Such a term would cancel, since only the chemical potential difference  $\mu^{(h)} - \mu^{(s)}$  enters into the equation of motion Eq. (5.3) for the interface.

Eqs. (5.2)-(5.6) fully describe the dynamics of the system, leading to a complicated nonlinear free moving boundary problem, and if external forces are applied to the system, the arising interfacial patterns are selected self-consistently during this non-equilibrium process.

## 5.2. Fast Crack Propagation: Selection Principles

The underlying selection principles induced by incorporating dynamic elastic effects are rather generic and similarly valid for models with conserved order parameters. They allow the experimentally observed steady state crack growth with propagation velocities well below the Rayleigh speed [100], tip blunting and branching [105] for high driving forces. Stresses on the boundary of the crack tip with finite radius  $r_0$  scale as  $\sigma \sim K r_0^{-1/2}$ , and the curvature behaves as  $\kappa \sim 1/r_0$ . Therefore, all contributions to the chemical potentials scale like  $\mu \sim 1/r_0$ , and this is ultimately the reason for the cusp singularity of the Grinfeld instability and the impossibility of a steady-state crack growth, if only static elasticity is taken into account: Then, the equations of motion (5.3) or (3.4) can be rescaled to an arbitrary tip radius which is not selected by the dynamical process. The explanation is that the linear theory of elasticity and surface energy define only one lengthscale, the Griffith length, which is macroscopic, but do not provide a microscopic scale which allows the selection of a tip scale. Formally, the equations of motion depend only on the dimensionless combinations  $vr_0/D$  for the phase transition dynamics and  $vr_0^3/D^{(sd)}$  for surface diffusion; the radius  $r_0$  and the steady state velocity  $v$  therefore cannot be selected separately and any rescaling which maintains the value of the product would therefore describe another solution. The situation changes if inertial effects are taken into account, which is reasonable for fast crack propagation. The maximum speed at which a crack can travel is the Rayleigh wave speed  $v_R$ , which is the sound propagation speed along a

free surface [113]. Then additionally the ratio  $v/v_R$  ( $v_R$  is the Rayleigh speed) appears in the equations of motion, and therefore a rescaling is no longer possible. Instead,  $D/v_R$  for the phase transition dynamics and  $(D^{(sd)}/v_R)^{1/3}$  for surface diffusion set the tip scale. Thus, we conclude that fast steady state growth of cracks is possible if dynamic effects are taken into account.

More formal analyses also including rigorous selection mechanisms due to the suppression of growing crack openings far behind the tip are given in [109] for phase transition processes and in [16] for surface diffusion.

This analysis shows that the selection principles which allow a fast steady state growth of cracks are similar for the simple phase transition process studied in this chapter and surface diffusion, studied in chapters 3 and 4. The latter does not require the introduction of a dense gas phase inside the crack and obeys conservation of the solid mass itself. Even more, surface diffusion can be understood in a generalized sense as plastic flow in a thin region around the extended tip. This way, the tip can be effectively described in the spirit of a lubrication approximation. Therefore, many general statements obtained for the phase transition dynamics can also be used for crack growth propelled by surface diffusion.

### 5.2.1. Multipole Expansion Method

We will briefly review the multipole expansion method [97] here, because we will compare the results we obtain with our phase-field model to it later. The multipole expansion method is based directly on the sharp interface equations and it is designed particularly for resolving the regime of steady state growth. In contrast to the phase-field model that will be presented in section 5.3, the limit of fully separated length scales is performed analytically, leading to a very efficient numerical scheme.

The method is based on a series expansion technique, and the fulfillment of the elastic boundary conditions on the crack contour reduces to a linear matrix problem, whereas the bulk equations of dynamical elasticity are automatically satisfied. Nevertheless, finding the correct crack shape and speed remains a difficult nonlinear and nonlocal problem.

The basic idea is to transform the problem into a well suited functional representation that describe the crack shape in a co-moving frame of reference. To this end, one introduces two functions  $\Phi(x, z, t)$  and  $\Psi(x, z, t)$  that are related to the displacements according to

$$u_x = \frac{\partial \Phi}{\partial x} + \frac{\partial \Psi}{\partial z}, \quad u_z = \frac{\partial \Phi}{\partial z} - \frac{\partial \Psi}{\partial x}.$$

In this representation, the bulk equations of elasticity decouple to two wave equations

$$\frac{\partial^2 \Phi}{\partial t^2} = c_d^2 \nabla^2 \Phi, \quad \frac{\partial^2 \Psi}{\partial t^2} = c_s^2 \nabla^2 \Psi,$$

where the constants  $c_d$  and  $c_s$  denote the dilatational and shear wave speed.

Choosing the appropriate rescaled coordinates perpendicular to the crack propagation direction,

$$z_d = \alpha_d z \quad \text{with} \quad \alpha_d^2 = 1 - \frac{v^2}{c_d^2}, \quad z_s = \alpha_s z \quad \text{with} \quad \alpha_s^2 = 1 - \frac{v^2}{c_s^2}$$

the time derivative disappears in a co-moving frame of reference ( $x \rightarrow x - vt$ ), and one is left with two Laplace equations

$$\frac{\partial^2 \Phi}{\partial x^2} + \frac{\partial^2 \Phi}{\partial z_d^2} = 0 \quad (5.7)$$

$$\frac{\partial^2 \Psi}{\partial x^2} + \frac{\partial^2 \Psi}{\partial z_s^2} = 0 \quad (5.8)$$

For the mode I loading situation under investigation, the solution for the crack shape is symmetric and using rescaled polar coordinates

$$\begin{aligned} x &= r_d \cos(\theta_d) = r_s \cos(\theta_s) \\ z_d &= r_d \sin \theta_d, z_s = r_s \sin(\theta_s) \end{aligned}$$

together with usual square root behavior for the tip stresses  $\sigma \sim r^{-1/2}$  (see section 2.2.3 Eq. (2.54)), the solution for the functions  $\Phi$  and  $\Psi$  have the form

$$\Phi = A_0 r_d^{3/2} \cos\left(\frac{3\theta_d}{2}\right) \quad (5.9)$$

$$\Psi = -B_0 r_s^{3/2} \sin\left(\frac{3\theta_s}{2}\right). \quad (5.10)$$

The two coefficients  $A_0$  and  $B_0$  can then be determined by employing the boundary conditions for a straight cut and matching to the far-field behavior, resulting in

$$\begin{aligned} A_0 &= \frac{8(1+\nu)(1+\alpha_s^2)}{3E\sqrt{2\pi}(4\alpha_s\alpha_d - (1+\alpha_s^2)^2)} K_{dyn} \\ B_0 &= \frac{2\alpha_d}{1+\alpha_s^2} A_0, \end{aligned}$$

with the dynamical stress intensity factor  $K_{dyn}$  for mode I. So far, this calculation is based on a cut-like crack with a sharp tip; to solve for a crack with an extended crack tip radius  $r_0$ , the functions  $\Phi$  and  $\Psi$  are given by a multipole expansion in a series of trigonometric functions, similar to the standard multipole analysis in electrostatics. The far-field behavior must remain unchanged, so for large distances  $r$  from the tip,  $r \gg r_0$ , the crack still looks like the semi-infinite mathematical cut. Therefore, the lowest order coefficients must be given by Eqs. (5.9) and (5.10) and the higher orders must decay sufficiently fast in order to not contribute to the asymptotics. These requirements lead to an expansion of the form

$$\Phi = r_d^{3/2} \left[ A_0 \cos\left(\frac{3\theta_d}{2}\right) + \sum_{n=1}^{N=\infty} \frac{A_n}{r_d^n} \cos\left(\left(\frac{3}{2} - n\right)\theta_d\right) \right] \quad (5.11)$$

$$\Psi = r_s^{3/2} \left[ B_0 \sin\left(\frac{3\theta_s}{2}\right) + \sum_{n=1}^{N=\infty} \frac{B_n}{r_s^n} \sin\left(\left(\frac{3}{2} - n\right)\theta_s\right) \right]. \quad (5.12)$$

Each eigenmode satisfies the elastodynamic Laplace equations Eqs. (5.7) and (5.8). Using the propagation velocity dependent universal angular distributions  $f_{ij,d}^{(n)}(\theta_d, v)$  for the dilatational contribution and  $f_{ij,d}^{(n)}(\theta_s, v)$  for the shear contribution, the stress field expansion is formally given by

$$\sigma_{ij} = \frac{K_{dyn}}{\sqrt{2\pi r}} \left( f_{ij}^{(0)} + \sum_{n=1}^{N=\infty} \frac{A_n f_{ij,d}^{(n)} + B_n f_{ij,s}^{(n)}}{r^n} \right). \quad (5.13)$$

The unknown coefficients  $A_n$  and  $B_n$  can be found by imposing the boundary conditions for the stresses,  $\sigma_{nn} = \sigma_{n\tau} = 0$ , on the crack contour. The tangential stress  $\sigma_{\tau\tau}$  is determined only by the solution of the elastic problem and enters the equations through the equation of motion Eq. (5.2) and Eq. (5.3).

From this point on, there are two strategies for solving the problem. For the **STEADY STATE APPROACH**, a strip geometry with a width very large compared to tip radius is assumed and the dimensionless driving force

$$F = \frac{1 - \nu^2}{2E\gamma} K_{stat}^2 \quad (5.14)$$

can be defined. Eq. (5.14) connects the external loading to the static stress intensity factor, which then serves as a free parameter for the simulations. Energy considerations in the spirit of [36] then give the following relation:

$$K_{dyn} = K_{stat} \sqrt{\frac{(1 - \nu)4\alpha_s\alpha_d - (1 + \alpha_s^2)^2}{\alpha_d(1 - \alpha_s^2)}} \quad (5.15)$$

During steady state, the whole shape advances without changing its shape or tip velocity  $v$ , so one can employ the purely geometrical equation for the local interface velocity  $v_n$

$$v_n - \underline{v} \cdot \hat{n} = v_n - v \cos \eta = 0 \quad (5.16)$$

with  $\eta$  being the angle between the local normal vector and the  $x$ -axis. This is a nonlinear function for the crack shape and the tip velocity  $v$ . In [97], it was solved directly using a multidimensional Newton method together with Powell's hybrid approach [98, 28], where the fact that the minimum of the functional is also the root is utilized.

For the **QUASIDYNAMICAL** approach, the geometrical steady state condition is not exploited. Rather, since at each time step, the stress field is known and all other quantities like the chemical potential and the resulting normal velocities can be calculated, an iterative algorithm to solve the problem numerically can be formulated. For the quasidynamical approach, the assumption of a steady state propagation also enters the method in Eqs. (5.7) and (5.8). Even though the series in Eqs. (5.11) and (5.12) are infinite, the results depend only weakly on the number of kept modes, and for  $N \geq 12$ , both methods are in excellent agreement. The analysis of the given sharp interface equations with the multipole expansion approach revealed the following:

- For driving forces below the Griffith point,  $F < 1$ , the crack retracts without scale selection, in concordance with the analytic expectation. Steady state solutions exist for arbitrary openings  $h$ .

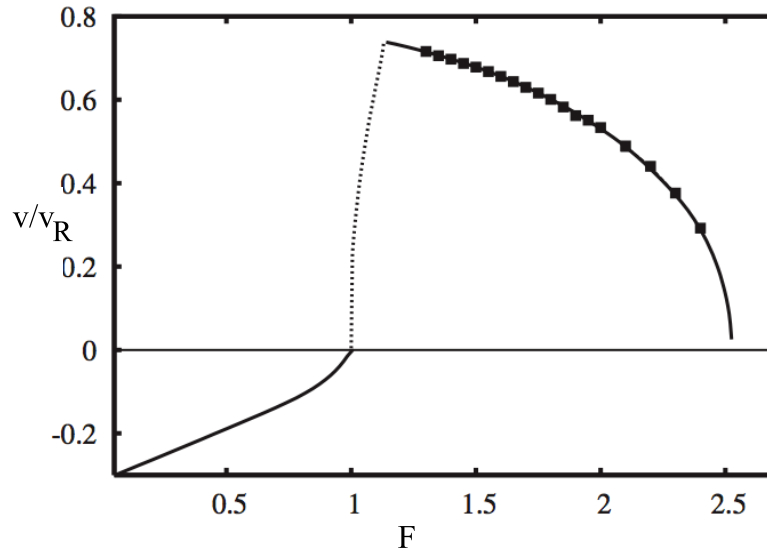


Figure 5.2.: Dimensionless steady state velocity as function of the dimensionless driving force  $\Delta$  as obtained by the multipole expansion method [97]. The solid line corresponds to the results obtained by the steady state approach, the squares to solutions obtained with the quasidynamic method. For  $F < 1.14$ , the dissipation-free solution is selected by a microscopic lengthscale. There is also no tip scale selected for  $F < 1$ , and the presented solution is obtained for a specific set of parameters  $v_r h/D = 10$ .

- For low driving forces  $1 < F \approx 1.14$ , there exist no dissipative solutions and the tail opening tends to zero, as dissipation becomes zero for  $F \approx 1.14$  and almost all energy is converted to surface energy. Only some kinetic energy remains, but is transported out of the system through the soft phase. This is due to the fact that in this regime, there is no intrinsic microscopic lengthscale present in the model.
- In the regime of driving forces  $1.14 < F < 2.5$ , steady state solutions exist. One notes, however, that the velocity is a monotonically decreasing function of the driving force.
- At driving forces around  $F \approx 1.8$ , the tip curvature becomes negative.
- For driving forces  $F > 2.5$ , the propagation velocity vanishes and the lengthscale given by the tail opening  $h$  diverges. The dissipation rate  $vh/D$  is a monotonic growing function that remains finite, however.

This can be interpreted as follows: obviously, the model prefers tip blunting over faster tip propagation as a mechanism to reduce the elastic stresses. This counterintuitive behavior could be a specific feature of the minimal model. The negative tip curvatures hint at a tip splitting mechanism due to a secondary Grinfeld instability, but this behavior cannot be resolved numerically with the multipole expansion approach, since the assumptions of symmetrical steady state solutions are intrinsically included in the solving methods.



### 5.3. Phase-Field Modeling for Crack Propagation

There are many phase-field models for fracture based on a non-conserved order parameter that encompass much of the expected behavior of cracks [62, 52, 2, 30]. But as long as the scale of the growing patterns is set by the phase-field interface width  $\xi$ , these models do not possess a quantitatively valid sharp interface limit. While phase-field models are often used to model physical processes associated with microstructural evolution, we want to emphasize that this is not our goal here. The diffuse interface model we present in this section is instead used primarily as a numerical tool to solve the sharp interface equations Eqs. (5.3)-(5.6). This means that the phase-field model permits a strict physical interpretation only in the limit of vanishing interface thickness,  $\xi \rightarrow 0$ , requiring that  $\xi$  is much smaller than any characteristic lengthscale in the problem. In order to succeed in this undertaking, our phase-field model has to fulfill two fundamental requirements: it has to have a valid sharp interface limit for the case  $\xi \rightarrow 0$ , and the results must not depend on the phase-field width  $\xi$ . Both requirements are directly connected to the fact that  $\xi$  is a purely numerical parameter and not directly connected to physical properties.

Alternative descriptions, which are intended to investigate the influence of elastic stresses on the morphological deformation of surfaces due to phase transition processes, are also based on macroscopic equations of motion. But they suffer from inherent finite time singularities which do not allow steady state crack growth unless the tip radius is again limited by the phase-field interface width [69].

In this section, we will present our phase-field model as given along the lines of section 2.5. We choose the minima for the phase-field to be the at  $\phi = 0$  for a “soft” phase inside the crack and  $\phi = 1$  for the “hard” phase outside of the crack. The energy functional has the usual three contributions:

$$\mathcal{F}[\phi, u_i] = \int dV (f_{dw} + f_s + f_{el}). \quad (5.17)$$

The first term is the double well potential

$$f_{dw}(\phi) = 6\gamma\phi^2(1 - \phi)^2/\xi,$$

with the interface width  $\xi$  and the surface energy density  $\gamma$ . The second term gives the surface energy

$$f_s(\phi) = \frac{3\gamma\xi}{2}(\nabla\phi)^2$$

and depends on the gradient of the phase-field.

Finally, the coupling to the external elastic forces is achieved through the elastic energy density

$$f_{el}(\phi, u_i) = \mu(\phi)\epsilon_{ij}^2 + \frac{\lambda(\phi)(\epsilon_{ii})^2}{2} \quad (5.18)$$

where the elastic material properties are written in terms of the interpolated shear modulus and Lamé coefficient

$$\mu(\phi) = h(\phi)\mu^{(h)} + (1 - h(\phi))\mu^{(s)}, \quad (5.19)$$

$$\lambda(\phi) = h(\phi)\lambda^{(h)} + (1 - h(\phi))\lambda^{(s)} \quad (5.20)$$

and the superscripts denote the bulk values. They depend on the phase-field and vary smoothly in the interface region with an interpolating function between the phases

$$h(\phi) = \phi^2(3 - 2\phi).$$

Note that the dependence of the functional  $\mathcal{F}$  on the displacements  $u_i$  is introduced in Eq. (5.18) by the strain tensor  $\epsilon$ . The elastodynamic equations are derived from the energy by the variation with respect to the displacements  $u_i$ ,

$$\rho \ddot{u}_i = -\frac{\delta \mathcal{F}}{\delta u_i} = \frac{\partial \sigma_{ij}(\phi)}{\partial x_j}, \quad (5.21)$$

and the dissipative phase-fields dynamics follows from

$$\frac{\partial \phi}{\partial t} = -\frac{D}{3\gamma\xi} \frac{\delta \mathcal{F}}{\delta \phi}, \quad (5.22)$$

where  $D$  again denotes the kinetic coefficient that also appears in Eq. (5.3).

Taking the functional derivative with respect to  $\phi$ , the full phase-field equation takes the form

$$\frac{\partial \phi}{\partial t} = D \left( \nabla^2 \phi - \frac{4}{\xi^2} \phi(1-\phi)(1-2\phi) - \frac{\mu_s}{3\gamma\xi} \phi(1-\phi) \right), \quad (5.23)$$

It has been shown in [69] that in the quasistatic case, the above equations lead to the sharp interface equations (5.3) – (5.6) if the interface width  $\xi$  is significantly smaller than all physical lengthscales present in the system.

We want to point out why the phase transformation model does *not* have the same problems as the surface diffusion model. The phase-field equation of the free model can be written as

$$\frac{\partial \phi}{\partial t} = K \left( \nabla^2 \phi - \frac{2}{\xi} w'(\phi) \right).$$

where  $w = \phi^2(1-\phi)^2$  denotes the double-well potential. The difference is that the velocity is already determined at the next-to-leading order. If we perform the sharp-interface analysis along the lines of chapter 3, we obtain

$$-v_n \partial_\rho \Phi^{(0)} = K \left( \partial_{\rho\rho} \Phi^{(1)} + \kappa \partial_\rho \Phi^{(0)} - 2w''(\Phi^{(0)}) \Phi^{(1)} \right) \quad (5.24)$$

instead of Eq. (3.34). We can again conclude that all terms on the right-hand side vanish in the limit  $\rho \rightarrow \pm\infty$ . However, this does not lead to any constraints, since the left-hand side depends on  $\rho$  now and goes to zero as well. Therefore, the limit is automatically fulfilled. In the surface diffusion case, we could only conclude that a function of  $s$ , namely  $d_2$  vanishes. So, the alternative approach does not introduce any new constraints, and the model approaches its asymptotic limit.

As we mentioned in section 5.1, when we explained the chemical potential Eq. (5.2), the soft phase only resembles an “elastic vacuum” due to the small elastic constants. If the phases are modeled to have comparable elastic moduli, one can also investigate solid-solid transformations. A systematic demonstration of this behavior can be seen in Fig. (5.3), where the Poisson ratios in both the surrounding solid and the new inner phase are chosen

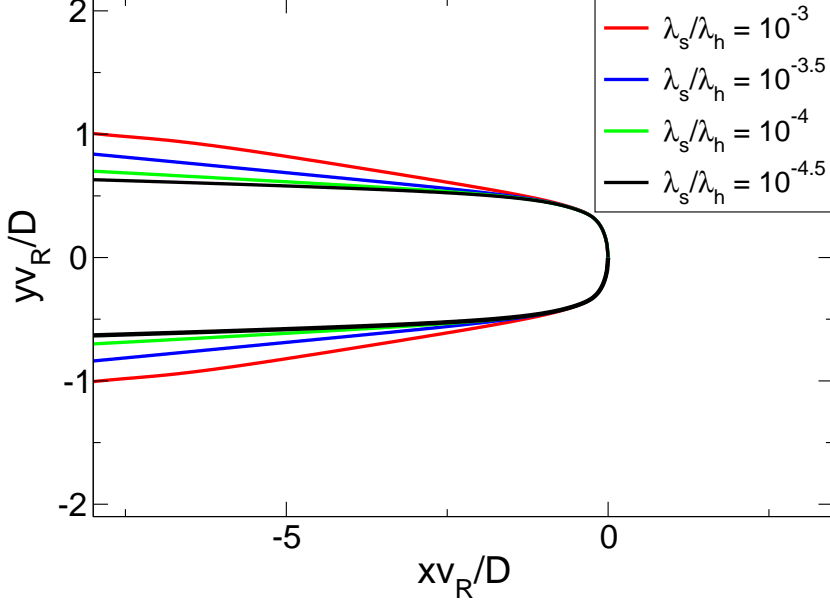


Figure 5.3.: Solid-solid transformation in a strip. A very soft phase grows at the expense of a harder phase. Parameters are  $Lv_R/D = 11.03$  ( $v_R$  is the Rayleigh speed of the hard phase),  $D/\xi v_R = 9.27$ , the aspect ratio is 2 : 1. The Poisson ratio  $\nu = 1/3$  is equal in both phases, and the driving force is  $F = 1.4$ .

equally,  $\nu = 1/3$ , but the bulk moduli differ by many orders of magnitude. The softer the inner phase becomes, the less the opening of the “crack” grows with increasing distance from the tip, and only very far away, the new phase fills the whole channel.

When this phase-field model was used in a previous publication [16], in comparing the results to [97], one could see that the phase-field simulations are still significantly influenced by finite size effects and insufficient separation of the appearing length scales, and therefore the results did not coincide. To overcome this problem, we resorted to large scale calculations and performed a careful extrapolation of the obtained data. As it turns out, we obtain an extremely satisfying agreement of the independent approaches.

### 5.3.1. Extrapolation

We want to recall briefly the ingredients and the strategy of our theory. We start from a macroscopic description of the system that does not account for the appearance of any processes at atomic length-scales. The theory is based on standard dynamic linear theory of elasticity, surface energy contributions and linear non-equilibrium transport theory, corresponding to a phase-transformation process, where the hard phase serves as a particle reservoir for the advancing soft phase whose propagation is driven by the

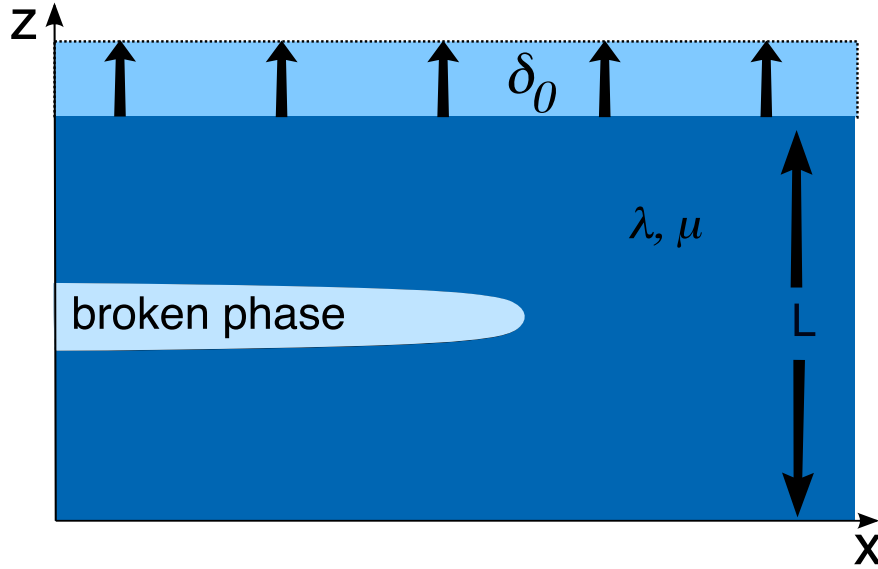


Figure 5.4.: Typical setup of the strip geometry. There is a fixed displacement at the upper and lower grip of the system which provides the elastic driving force. The solid phase is characterized by the elastic constants  $\lambda$ ,  $\mu$ ; the broken phase has vanishing elastic constants.

interplay of the reduction of elastic energy at the cost of increasing surface energy. The central prediction of this theory of fracture is that a well-defined steady-state growth with finite tip radius and velocities appreciably below the Rayleigh speed is possible. By taking dynamic elastic effects into account, this also cures the problem of the finite-time cusp singularity of the Grinfeld instability, as was shown in section 5.2. These predictions have been confirmed by sharp interface methods [97] which are based on a multipole expansion of the elastodynamic fields and also by phase-field simulations [109]. Surprisingly, it turned out that the obtained results seem to differ significantly in the overlapping parameter range. In particular, the sharp interface method predicts a range of driving forces inside which the velocity of the crack is a monotonically decreasing function. Here, we show that the discrepancy of results is due to finite size effects of the previous phase-field results [109], and that by careful extrapolation of large-scale simulations, a coinciding behavior is obtained. The multipole expansion technique described in section 5.2.1 is designed to model a perfect separation of the crack tip scale  $D/v_R$  to the strip width  $L$ . Since in most real cases, crack tips are very small, it is theoretically desirable to describe this limit. For the phase-field method, however, a finite strip width  $L$  is necessary, and a good separation of the scales therefore requires time-consuming large-scale calculations.

The Griffith point is defined by the equilibrium condition between the energy stored far ahead of the crack and that far behind the crack tip. In a plane strain situation, see section 2.1.6, a finite displacement  $\delta_0$  is applied to a rectangular strip of width  $L$ , as shown in Fig. 5.4. Far behind the crack tip, the elastic energy has been released due to the crack opening and the stored energy is simply given by the surface energy of the newly created

### 5.3. PHASE-FIELD MODELING FOR CRACK PROPAGATION

---

crack interfaces,  $E_{surf} = 2\gamma$ . In the region ahead of the crack, the material stores only elastic energy due to the initial displacement, which is given by the elastic energy density and the strip width,  $E_{el} = \sigma_{ij}\epsilon_{ij}L/2$ . For the isotropic material under consideration here, Hooke's law couples stresses and strains,

$$\sigma_{ij} = 2\mu\epsilon_{ij} + \lambda\delta_{ij}\epsilon_{kk}$$

with the Lamé-coefficient  $\mu$ , the bulk modulus  $\lambda$  and  $\delta_{ij}$  denoting the Kronecker-Delta. Since  $\epsilon_{xx}$  vanishes in the chosen setup, the elastic energy density can be written in the form

$$\frac{1}{2}\sigma_{ij}\epsilon_{ij} = \frac{1}{2}\sigma_{zz}\epsilon_{zz} = \frac{1}{2}(2\mu + \lambda)\epsilon_{zz}^2. \quad (5.25)$$

The elastic state far ahead of the crack tip can be assumed to be homogeneous and free of shear strains, so that strain  $\epsilon_{zz}$  is given by  $\epsilon_{zz} = \delta_0/L$ . The equilibrium condition for crack propagation

$$E_{surf} = E_{el} \quad (5.26)$$

is then given by

$$2\gamma = \frac{2\mu + \lambda}{L}\delta_0^2,$$

which we use to define a dimensionless driving force

$$F = \frac{(\lambda + 2\mu)}{4\gamma L}\delta_0^2. \quad (5.27)$$

The Griffith point [42] corresponds to the value of  $F = 1$ , and for larger values of  $F$ , the crack grows.

We would like to point out that if the soft phase is modeled to have significant elastic moduli, as is the case for solid-solid transformations, but the interface is still assumed to be coherent (i. e. there is no lattice mismatch between the two phases), the equilibrium condition Eq. (5.26) can easily be generalized to

$$\frac{2\mu^{(s)} + \lambda^{(s)}}{L} + 2\gamma = \frac{2\mu^{(h)} + \lambda^{(h)}}{L},$$

leading to a slightly modified definition of the driving force,

$$F = \frac{(2\mu^{(h)} + \lambda^{(h)})\delta_0^2}{4\gamma L + (2\mu^{(s)} + \lambda^{(s)})\delta_0^2}. \quad (5.28)$$

Apart from the finite size restriction, the phase-field method necessitates the introduction of the interface width  $\xi$  as a numerical parameter, and one has to make sure that all physical lengthscales are much larger in order to obtain results that are in quantitative agreement with the corresponding sharp interface equations. Therefore, the simulations have to satisfy the hierarchy relation

$$\Delta x \ll \xi \ll \frac{D}{v_R} \ll L, \quad (5.29)$$

where  $\Delta x$  denotes the numerical grid spacing. For the numerical realization, we employ

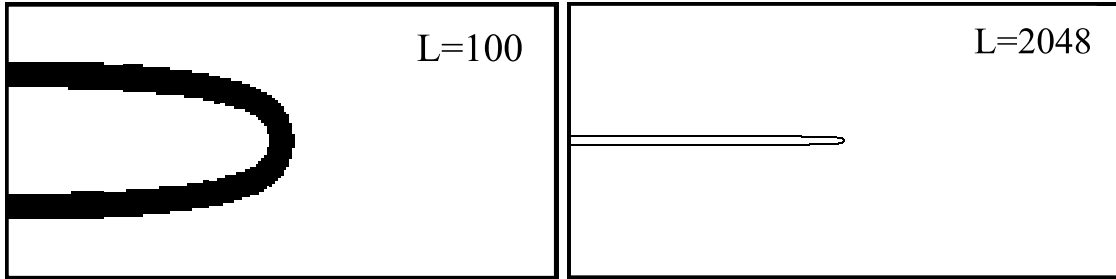


Figure 5.5.: Crack shapes for different system sizes. The interface width  $\xi$  is kept constant. For the crack shape on the left, the scale separation is not good, since the interface width and the system height are of the same order of magnitude. For the crack shape on the right, the scales are obviously well separated.

explicit representations of both the elastodynamic equations and the phase-field dynamics, where the elastic displacements are defined on a staggered grid [114]. Details of the numerical implementation are given in Appendix A.5.

The smoothness of the interface region has to be resolved numerically, so the interface width  $\xi$  has to be noticeably larger than  $\Delta x$ . While it is possible to choose  $\xi = 2.5\Delta x$  [10, 11], the discrete nature of the grid is noticeable for such low resolutions and can lead to spurious effects like lattice trapping or anisotropy effects [46]. Since we do not want to eliminate this additional finite-size effect, we start with a resolution for  $\xi$  that is definitely on the safe side. Tests show that the choice  $\xi = 5\Delta x$  is by far sufficient to resolve the phase-field profile very accurately and avoid lattice trapping and will be kept constant. Note that this choice actually means that approximately ten points are used to resolve the smooth interface region.

The other scales have to be varied in comparison to the phase-field width over several orders of magnitude, which is numerically hard to achieve due to the large grids that need to be used. The typical set-up is to use strip lengths  $2L$  and shift the system such that the tip remains in the horizontal center. Thus, we can study crack growth over long times in relatively small systems. Typical dimensions used here are  $1000 \times 500$  grid points, but could be considerably larger (up to  $8200 \times 4100$  grid points). The Poisson ratio is chosen to be  $\nu = 1/3$  and the elastic constants of the new phase inside the crack are set close to zero (typically the ratio between the values in the soft phase and the ones in the hard phase was  $10^{-8}$ , however, these values are qualitatively not significant).

For being able to handle the large grids, we developed a parallel code using MPI. This was strongly facilitated by the use of explicit schemes, where domain decomposition is straight-forward and many processors can be used efficiently. All simulations were performed on the supercomputers JUBL, JUMP and JUGENE, which are operated at the research center Jülich. Benchmarks reveal that if we increase the system size with the number of processors (weak scaling), the speedup is an excellent 98% on up to 8192 processors. In the case of strong scaling, where the same computational domain is handled by an increasing number of processors, the speedup is still an excellent 92% if we use up to 8192 cpus. The benchmark results can be seen in Fig. 5.6.

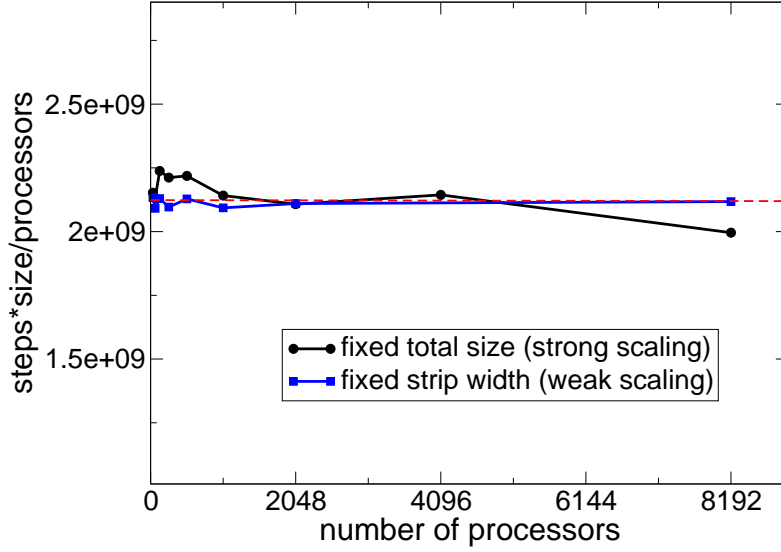


Figure 5.6.: Scaling behavior of the phase-field implementation. The ideal scaling behavior is indicated by the red line. The slight decrease of the strong scaling curve is due to the fact that the portion of the original computational domain becomes quite small for each of the many processors used. If the processor load is kept constant and the total system size scales with the number of processors, the speedup is almost perfect.

Close to crack tips, stresses become large, exhibiting characteristic square-root singularities which are related to stress intensity factors, see Fig. 5.7, and the phase-field code can also be used to extract them. For cracks with finite tip radius  $r_0$ , the stress scaling  $\sigma \sim r^{-1/2}$  at a distance  $r$  from the tip is only valid in an intermediate regime in finite systems: Close to the tip, higher order terms can appear,

$$\sigma_{ij} = \frac{K}{(2\pi r)^{1/2}} \left( f_{ij}^{(0)} + \sum_{n=1}^{\infty} \frac{A_n f_{ij,d}^{(n)} + B_n f_{ij,s}^{(n)}}{r^n} \right), \quad (5.30)$$

which are suppressed only for sharp tips. Here, the functions  $f_{ij,d}^{(n)}(\theta_d, v)$  and  $f_{ij,s}^{(n)}(\theta_s, v)$  are the universal angular distributions for the dilatational and shear contributions. Far away from the tip, the stress distribution is significantly influenced by the specific boundary conditions. However, from the intermediate region, the stress intensity factor can be extracted. This is done here for a fast moving crack with propagation velocity  $v/v_R = 0.68$  ( $v_R$  is the Rayleigh speed) subjected to a mode I loading; a deviation of about 10% for the dynamical stress intensity factor from its theoretical expectation is due to the fact that the crack opening is rather large in comparison to the system size.

We mentioned in section 5.2.1 that in the framework of the model, it was shown that dissipation free solution exist close to the Griffith point [97]: In this regime  $1 < F < 1.14$ , an additional microscopic length scale is needed to select the small tip radius which is no

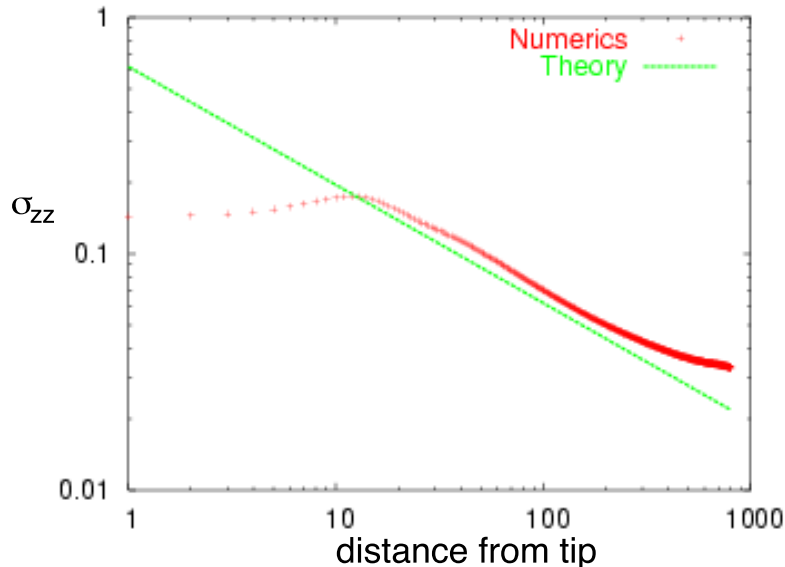


Figure 5.7.: Determination of a dynamical stress intensity factor for a crack with good scale separation like shown in the lower panel of Fig. 5.3.1. The value of the vertical stress component  $\sigma_{zz}$  as a function of the distance from the tip is shown in a logarithmic presentation. In an intermediate regime, the square-root behavior is clearly visible.

longer determined by the ratio  $D/v_R$ . In the phase-field simulation, this "atomic" cutoff can be mimicked by the phase-field interface width and was already done in [109].

Here, we focus first on the more interesting regime of higher driving forces, but still below the threshold of instability. One can see the effect of the numerical scale separation in Fig. 5.8, where typical crack shapes in the vicinity of the tip are shown. The effects of better scale separations become less and less pronounced. In order to fulfill the scale separation requirements (5.29), we remove the finite-size effects in the obtained steady state velocities  $v_{L,\xi}$  systematically through a double extrapolation procedure. The subscripts indicate the additional non-resolved length scale dependencies.

In the first step, we extrapolate the results of the simulations to an infinite system size by decreasing the ratio  $\xi/L \rightarrow 0$  for fixed tip scale ratio  $D/\xi v_R$ . This step is demonstrated in Fig. 5.9 for  $F = 1.4$ , where the dimensionless propagation velocity  $\tilde{v}_{L,\xi} = v_{L,\xi}/v_R$  is plotted as function of the inverse square root of the system size  $(\xi/L)^{1/2}$ . In this representation, the data for the larger systems can be extrapolated linearly to infinite system sizes, since numerically we get a scaling

$$\tilde{v}_{L,\xi} \left( F, \frac{D}{v_R \xi}, \frac{L}{\xi} \right) = \tilde{v}_\xi \left( F, \frac{D}{v_R \xi} \right) + \alpha \left( \frac{\xi}{L} \right)^{1/2} \quad (5.31)$$

for large systems,  $\xi/L \ll 1$ , with a constant  $\alpha > 0$  for each curve. Because the points to the very far right correspond to the *smallest* system sizes, the corresponding runs yield the least accurate results.



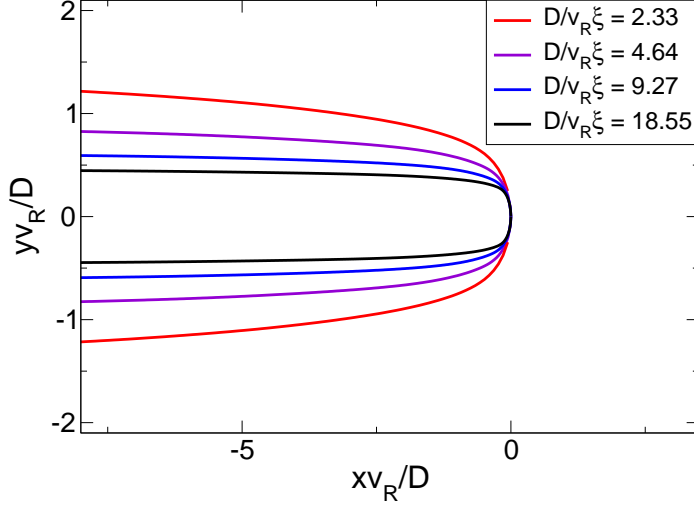


Figure 5.8.: Crack shapes for different scale separations  $D/v_R\xi$  and fixed ratio  $Lv_R/D = 11.03$ ; the aspect ratio of the system is 2 : 1. The driving force is  $F = 1.4$ . By improvement of the separation, the crack opening is reduced, and finally the boundaries become straight parallel lines.

If the separation of  $D/v_R$  to  $\xi$  were perfect, the extrapolated values  $\tilde{v}_\xi(F, D/v_R\xi)$  would cumulate to a single point. But Fig. 5.9 shows clearly that this is not the case and therefore a second extrapolation step is necessary.

This second step, shown in Fig. 5.10 (again for  $F = 1.4$ ), consists of resolving the dependence of the velocity  $v_\xi/v_R$  on the separation parameter  $v_R\xi/D$ . To do so, we use the extrapolated values from Fig. 5.9 to obtain a scaling

$$\tilde{v}_\xi\left(F, \frac{D}{v_R\xi}\right) = \tilde{v}(F) - \beta \frac{v_R\xi}{D} \quad (5.32)$$

with a constant  $\beta > 0$  and the dimensionless sharp interface limit velocity  $\tilde{v} = v/v_R$ . The colors of the symbols correspond to the respective lines in Fig 5.9. Both scaling relations (5.31) and (5.32) are obtained empirically from the numerical data. The constant  $\tilde{v}(F)$  is the final extrapolated tip velocity for one given value of the parameter  $F$  that can then be compared to the results from the multipole expansion method.

We performed this tedious procedure for several driving forces, and the comparison to the multipole expansion method [97] is shown in Fig. 5.11. The agreement of the results which are obtained from completely different and independent methods is convincing.

In particular, we find evidence for the prediction that the steady state velocity decays weakly with increasing driving force. It turns out that the increase of the dissipation rate

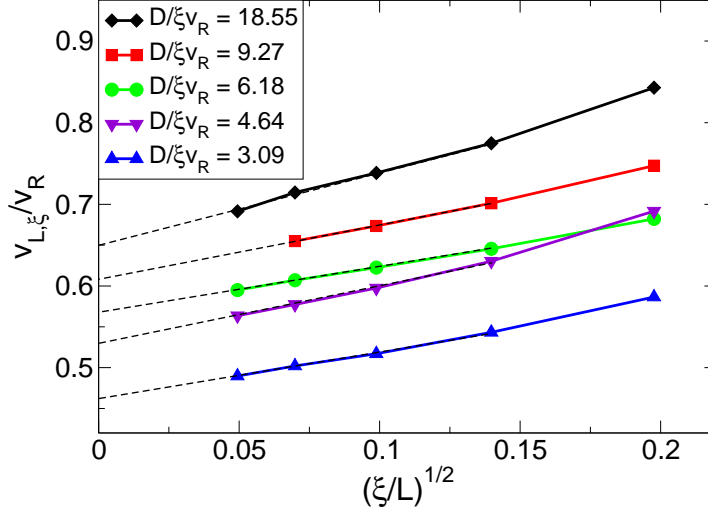


Figure 5.9.: First step of the extrapolation procedure for the dimensionless velocity  $v/v_R$ . The system size  $L/\xi$  is increased and the ratio  $D/\xi v_R$  is kept fixed for each curve. For each ratio, an extrapolated velocity  $v_\xi/v_R$  corresponding to an infinite system size is obtained, as indicated by the dashed lines. The driving force is  $F = 1.4$ .

is due to the strong tip blunting, which is a new degree of freedom in the current model, since the entire crack shape is selected self-consistently. The explanation for this behavior is that the dissipation function is given by the dimensionless quantity  $vr_0/D$ , and this is indeed a monotonically increasing function of the driving force  $F$ , as can be seen in Fig. 5.12; theoretically, it is not required that  $v/v_R$  itself grows. If the tip radius were fixed due to additional constraints, which we carefully avoided to contain in the current description, an increasing velocity  $v(F)$  would be the consequence. A possible way to mimic such a constraint in the phase-field description is to introduce a length-scale cutoff in the tip by a small lengthscale  $D/v_R$ , which results in  $r_0 \sim \xi$ . This behavior was already studied in [109], and a growing function  $v(F)$  was found, in qualitative agreement with other phase-field descriptions and molecular dynamics models with sharp tips. However, the decreasing velocity might be an artefact of the model. We also note that it is conceivable for other transport mechanisms that the effect of tip blunting is less pronounced or does not occur, and therefore an increase of the propagation velocity with the driving force  $F$  would be possible even for full scale separation  $r_0 \gg \xi$ .

As we already discussed at the end of section 5.2.1, in the regime of higher driving forces, the tip curvatures became negative, hinting at a possible tip splitting scenario which could not be resolved with neither the steady-state nor the quasi-dynamic multipole expansion method. The phase-field method, however, is able to reliably resolve also this parameter

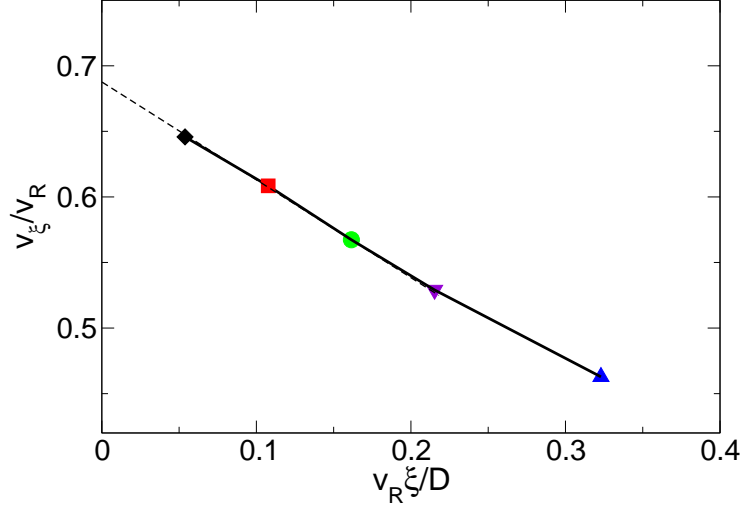


Figure 5.10.: Second extrapolation step to obtain the sharp interface velocity  $v$ . The extrapolated velocities obtained from Fig. 5.9 are plotted as function of the scale separation parameter  $v_R \xi / D$ . In this example  $F = 1.4$  is used.

regime, and for higher driving forces, we observe tip splitting indeed. The scaling analysis 5.2 predicts that for both mechanisms, surface diffusion and phase transformation, tip splitting is possible for high applied tensions due to a secondary ATG instability: Since the stresses scale as  $\sigma \sim K r_0^{-1/2}$  in the tip region and the local ATG length is  $L_G \sim E \gamma / \sigma^2$ , an instability can occur, provided that the tip radius becomes of the order of the ATG length. In dimensionless units, this leads to the prediction  $F_{split} \sim \mathcal{O}(1)$  for the dimensionless driving force  $F$ . Therefore steady-state solutions exist only up to a critical value of  $F$ . A prototypical series of snapshots for such a crack at different times is shown in Fig. 5.13 for a value of  $F = 2.0$ . The color coding represents the elastic stresses present in the system. The crack tip starts blunting, finally splitting up in two cracks. One crack tip wins the competition and continues to grow while the other stops, as the material around it has relaxed. This is qualitatively in very good agreement with experimental observations [75, 76, 104, 105]. The complex interaction between the elastic fields and the free moving boundary is clearly visible, indicating that a sharp tip approach might not be sufficient to describe such a propagation behavior.

It is worth mentioning that the onset of the irregular branching behavior depends sensitively on the system size, since the scale separation and the system size need to be large enough. In relatively small systems, the branches of the crack cannot separate since they are repelled by the boundaries and are effectively stabilized by the limited system size. Therefore, the steady state growth is always stabilized by finite size effects. On the other hand, initial conditions can trigger an instability, and then a long transient is required to get back to steady state solutions. Despite these restrictions, we are still able

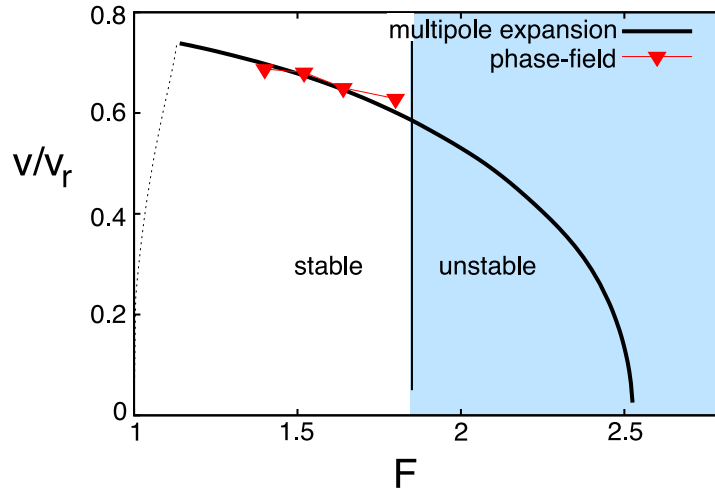


Figure 5.11.: Comparison of the steady-state crack velocity obtained from the multipole expansion technique [97] and the extrapolated value from phase-field simulations. The colored region indicates the range of driving forces for which the multipole expansion method has only unstable solutions with negative tip curvature, hinting at a tip splitting instability (see text).

to make the prediction that the threshold of splitting obeys  $F_{split} \lesssim 1.9$  in the phase-field model. This is in agreement with the conjecture that branching occurs as soon as the steady state tip curvature becomes negative, leading to the prediction  $F_{split} \approx 1.8$  obtained by multipole expansion [97]. The small deviation of the velocity in Fig. 5.11 for  $F = 1.8$  can be traced back to the fact that this value is already close to the threshold of the tip-splitting instability which cannot be captured by the multipole expansion method.

Consequently, even for (weakly) growing velocities  $v(F)$  in models similar to the one presented here, the steady state velocity would remain well below the Rayleigh speed due to the termination of the steady state branch; moreover, even without the tip splitting instability, the velocity could remain below  $v_R$  for sufficiently strong tip blunting, depending on the particular model.

The numerical determination of a characteristic crack width scale in the sharp interface limit is more difficult, and therefore we refrain from performing a double extrapolation procedure. Because the soft phase inside the crack still possesses small nonvanishing elastic constants, the equilibrium situation far behind the crack tip corresponds to a full opening of the crack, instead of the opening being of the order  $D/v_R$ , and the elastic energy is minimized if the hard phase completely disappears. Small remaining elastic constants can be due to an insufficient separation of the scales  $D/v_R$  and  $\xi$ , since according to Eqs. (5.19) and (5.20), the elastic constants decay only exponentially inside the crack, even if this soft phase has nominally vanishing elastic coefficients. Therefore, the crack

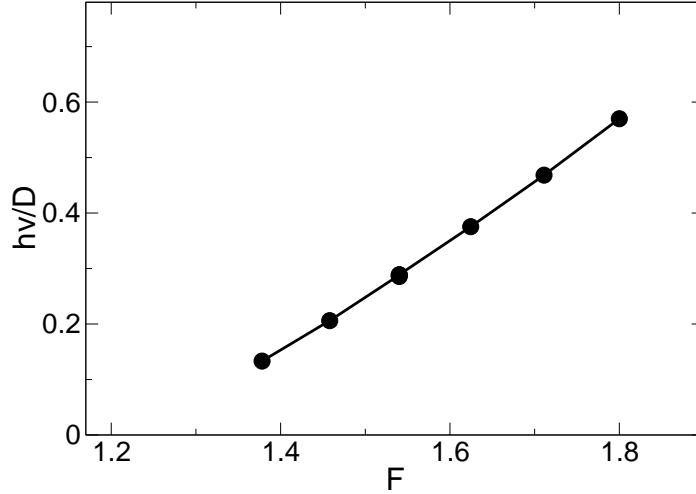


Figure 5.12.: Dissipation rate as function of the external driving force. Since the velocity is a decreasing function, the tendency to dissipate energy by tip blunting is very pronounced.

opening is a weakly growing function of the distance from the crack tip, and this slope becomes smaller with better scale separation, as can be seen Fig. 5.8. We point out that the opening of these crack shapes is solely due to the phase transition process. To obtain the real shape under load, one would have to add the elastic displacements to the drawn shapes. For example, the vertical displacement obeys the usual scaling  $u_y \sim \sqrt{|x|}$  for large distances  $|x|$  from the tip.

## 5.4. Conclusion

In this chapter, we investigated the behavior of a minimal continuum model for crack propagation by an elastically induced phase transition between two coherent phases which does not contain any specific assumptions about cracks and can even be used for solid-solid transformations (see Fig. 5.3). We can model the elastic vacuum by assigning vanishing elastic constants to the inner phase and take the late stage of the Grinfeld instability as a starting point, where deep grooves form that advance very rapidly. The link to conventional fracture mechanics is given by the fact that in both cases, the interface movement is determined by the competition between elastic and surface energy effects. In our approach, we treat the crack as a free boundary, and we showed in section 5.2 that by using dynamic theory of elasticity, the finite time cusp singularity can be removed and a simultaneous selection of crack velocity and tip radius is possible. The central finding of this theory are that it predicts a regime of steady-state growth with velocities well below the

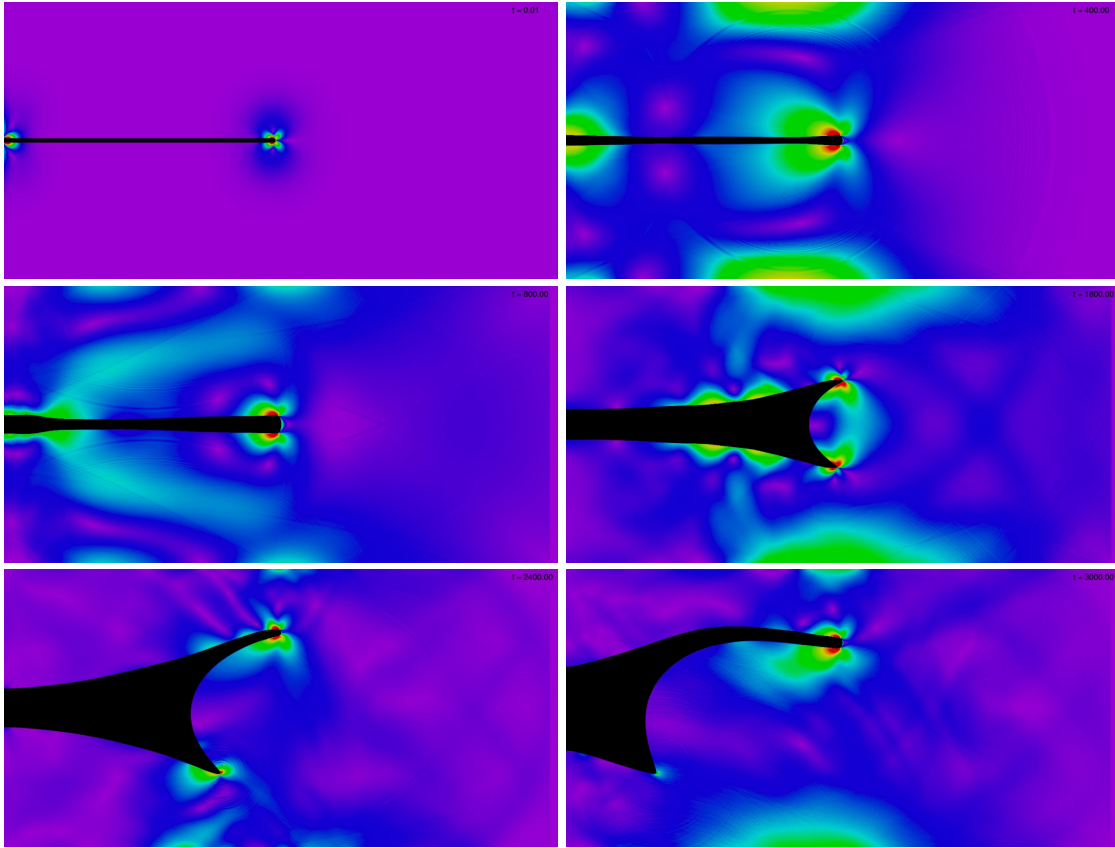


Figure 5.13.: Irregular tip splitting scenario for  $F = 2.0$ . We used  $Lv_R/D = 44.2$  and  $D/v_R\xi = 9.3$ ; the aspect ratio of the system is 2:1. Time is given in units  $D/v_R^2$ . The color coding visualizes the stress field, where violet indicates the lowest and red the highest stresses.

Rayleigh speed. This is in agreement with findings obtained by sharp interface methods from the literature [97]. A careful comparison of the quantitative data in the overlapping parameter regime revealed that it is of great importance to remove finite size effects in the phase-field simulations. We therefore performed a double extrapolation, first to infinite system sizes, see Fig. 5.9, and then to vanishing interface widths, see Fig. 5.10, and obtained an extreme convincing agreement of the totally independent numerical methods, see Fig. 5.11. We are also able to determine quantities like the dynamical stress intensity factor numerically. Extending the simulations into the regime of higher driving forces, we found a dynamic tip splitting instability, see Fig. 5.13, a behavior that is known from experiments [36, 75, 76, 104, 105].



## 6. Collective Behavior of Multi-Cracked Material

As was made clear in the previous chapters, fracture provides an effective mechanism for the material to release elastic energy. Of course, the properties of a cracked material can be strikingly different from the uncracked one, total failure just being an extreme case. Very often, a material contains many micro-cracks which do not necessarily lead to total failure, but their presence alters the elastic properties of the system. Therefore, one is interested in an estimation of the effective material constants that can be attributed to the now heterogeneous system consisting of the original solid matrix and the inclosed cracks. Cracked material is just one case in the widely dealt-with topic of physical properties of heterogeneous media [59]. The different physical properties to be described encompass conductive, transport and also elastic quantities [101, 32, 48, 34]. Often, one starts from a coarse-grained picture and aims to find an effective description for the heterogeneous mixture. Much effort has been put into the calculation of effective elastic properties of composed media where the constituents have different elastic coefficients [49, 102, 13, 39, 40, 41]. A comprehensive overview can be found in in [86].

A very important step towards an effective medium theory was the work of Eshelby [32]. His calculation of the elastic fields around and inside a single ellipsoidal inhomogeneity in an infinitely extended, linearly elastic homogeneous solid provides the starting point for many approximative approaches. In the context of conductivity and dielectrics of heterogeneous media, Bruggeman [18] introduced a method he named SYMMETRIC EFFECTIVE MEDIUM THEORY, since its results are insensitive to phase interchange; this method became known as SELF CONSISTENT SCHEME (SCS) [19, 26, 56] later, which is an unfortunate choice of name, since self-consistency is too weak a requirement to fully characterize the approach [47]. Being very similar to an averaging method known as DILUTE DISTRIBUTION MODEL, it predicts that the elastic constants vanish linearly with the void volume fraction, which is in disagreement with experimental and numerical results [86]. The phase-biased method, where one phase is considered to be a solid matrix that contains inclusions of a second phase, has been developed further to become the DIFFERENTIAL SCHEME, also known as ITERATED HOMOGENIZATION METHOD and has later been used in many different applications [79, 87, 47, 93, 39, 41].

One should note that since the basic ideas for the different approaches are conceptually similar and the predictions can be identical for the systems under consideration, the naming convention in the literature is not always consistent. The common basic assumption of most approaches is that the the concentration or volume fraction of the inclusions is the most important quantity by which a heterogeneous system can be characterized: in a very dilute distribution, one may neglect interaction effects. If the concentration increases, however, interaction effects play an increasingly important role. So the question arises how the different effective schemes include these interaction effects.



It turns out that the elastic properties of the system depend not only on the inclusion concentration, but the positional and orientational distributions of the inclusions also have a strong effect. Even different loading paths can lead to a different elastic response of the material under investigation [56]. Therefore, special attention has to be paid to the underlying assumptions of the cavity distribution. It has been shown that the most restrictive bounds that can be obtained for the bulk modulus of two-phase materials in terms of phase moduli and volume fractions are Hashin-Shtrikman-type bounds [48, 49]. Improvement to these bounds have to involve considerations of statistical details of phase distributions Torquato91.

Quite naturally, there has always been considerable interest in the special case that a homogeneous material becomes heterogeneous by the appearance of cracks. While often cracks constitute the limit of the elastic moduli of the second phase going to zero for many theories, they are special in the sense that they can weaken a material substantially also if the cracks are slitlike and the volume fraction is very small. This necessitates a different measure of defect concentration, leading to entirely different material behavior.

We will see in the following that while the differential scheme predicts an exponential decay of the effective elastic constants for random crack distributions, we can show here by simple scaling arguments that for an arrangement of parallel cracks, the effective elastic constants show a power law decay.

## 6.1. Differential Homogenization Method

The differential scheme has been developed to estimate the effective elastic properties and has been used by numerous authors [18, 19, 34, 80, 47, 93] to treat dilute suspensions of inclusions or cracks. One can imagine that due to high stresses, many small cracks can form independently and randomly within a loaded material to relax the stress in their immediate neighborhood. The cracks can advance until their relaxed zones come into contact. The largest and most favorably oriented cracks continue to grow to reduce the elastic energy, winning the competition against their smaller neighbors. This growth then continues on a larger scale until the larger crack's respective regions of influence come into contact and so on. Because the inclusions/cracks are of larger size, they "see" an effectively homogeneous medium that includes the smaller inhomogeneities. This process is illustrated in Fig. 6.1.

One should note, however, that this can only be considered to be a thought experiment as the requirements of an infinitesimal inclusion increment, large numbers of inclusions and increasing order of magnitude of inclusions are mutually contradictory. Despite its highly idealistic hierarchical picture, it turns out that this self-consistent approximation approach produces reasonable results even for static, nonhierarchical random mixtures. In the following paragraphs, we will outline the line of reasoning in more detail.

First, we consider the general situation where the system under consideration consists of two different homogeneous isotropic elastic materials; the special case of cracks, where the second phase is modeled as a material that does not support any stresses at all, will be treated later in section 6.3.2. The idea of the differential scheme is the following: A system of dimensionless "volume"  $V_0 = 1$  contains inclusions of a second phase, characterized by

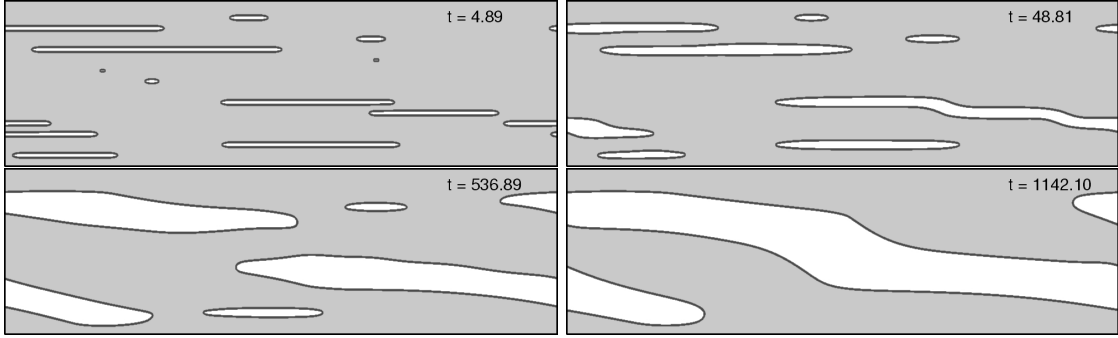


Figure 6.1.: Illustration of the coarsening process as obtained with phase-field simulations for an irregular arrangement of cracks in a uniaxially strained solid with periodic boundary conditions in lateral direction. Large cracks grow at the expense of smaller ones. The parameters used here are  $\Delta = 6$ ,  $D/\xi v_R = 2.32$ , and the system size is  $1000 \times 300$  grid points. Time is given in units  $D/v_R^2$ .

the initial concentration  $c_0$ , which in turn means that the concentration of the first phase is  $1 - c_0$ . If density differences are neglected, the volume fraction of phase two is therefore also  $c_0$ .

Now, a volume of  $dc_0$  of the second phase to the original volume  $V_0 = 1$  is added, leading to a total volume of  $V = 1 + dc_0$ . The total volume of phase two has increased to  $c_0 + dc_0$ , resulting in a total volume fraction of

$$\begin{aligned} c &= \frac{c_0 + dc_0}{1 + dc_0} \\ &= c_0 + (1 - c_0)dc_0 + O(dc_0^2) \end{aligned} \quad (6.1)$$

The change of concentration of the second phase is therefore

$$dc = (1 - c_0)dc_0 \quad (6.2)$$

Let  $M_{eff}$  denote a complete set of elastic constants, for instance  $M = \{\lambda, \mu\}$ . If the effective constants  $M_{eff}$  are of the form

$$M_{eff} = F(M_1, M_2, c), \quad (6.3)$$

they can always be written equivalently in the form

$$M_{eff} = F(M_{eff}, M_2, c = 0). \quad (6.4)$$

Employing the above identity and performing a series expansion of  $F$  leads to

$$\begin{aligned} M_{eff} + dM_{eff} &= F(M_1, M_2, c + dc) \\ &= F(M_{eff}, M_2, dc_0) \\ &= F(M_{eff}, M_2, 0) + \left. \frac{\partial F(M_1, M_2, c)}{\partial c} \right|_{\substack{c=0 \\ M_1=M_{eff}}} \frac{dc}{1 - c}, \end{aligned}$$

where we used Eq. (6.2) for the last equality, which in turn leads to the relation

$$\frac{dM_{eff}}{dc} = \frac{1}{1-c} \left. \frac{\partial F(M_1, M_2, c)}{\partial c} \right|_{\substack{c=0 \\ M_1=M_{eff}}}, \quad (6.5)$$

which is the central set of differential equations that determine the solutions for the effective elastic moduli in the framework of the differential homogenization approach. We would like to point out that, after performing the derivative on the right hand side, it is important to set the concentration to zero first and only then to replace  $M_1$  by  $M_{eff}(c)$ , as these operations do not commute.

Obviously, this approach is independent of the dimensionality of the system. For a one-dimensional system, which can be pictured as consisting of two different connected springs, the exact solution can be easily derived. This one-dimensional exact solution can also be recovered with the described method, since the geometrical aspects of the theory of elasticity do not come into play; this is shown in Appendix A.3. For two and three dimensions, the differential approach ceases to be exact due to the geometrical aspects of elastic interaction, but it still obeys the Hashin-Shtrikman-bounds [60]. While two and three dimensional systems differ strongly to one dimensional systems due to these geometrical interactions, these higher dimensional systems can be very similar to each other. Setups with transverse isotropy in one direction under plane strain loading are specifically designed to exploit this similarity.

Before we investigate the applicability of the differential homogenization method to various physical setups, we would like to display the conversion rules of two- and three-dimensional elasticity.

### 6.1.1. Two- and Three Dimensional Elasticity

The results presented in this chapter pertain to both two and three dimensional systems. For the *three dimensional* problems, we particularly concentrate on plane strain situations, see section 2.1.6, i. e.

$$u_x = u_x(x, z), \quad u_z = u_z(x, z), \quad u_y = 0. \quad (6.6)$$

where  $u$  denotes the displacement field. The linear relations between the stress  $\sigma$  and the strain  $\epsilon$  as given by Hooke's law, see section 2.1.5, then take the form

$$\begin{aligned} \epsilon_{xx} &= \frac{1}{E} [(1 - \nu^2)\sigma_{xx} - \nu(1 + \nu)\sigma_{zz}] , \\ \epsilon_{xz} &= \frac{1 + \nu}{E} \sigma_{xz} , \\ \epsilon_{zz} &= \frac{1}{E} [(1 - \nu^2)\sigma_{zz} - \nu(1 + \nu)\sigma_{xx}] , \end{aligned}$$

and all other strain components vanish.

Two-dimensional elasticity uses a different representation, however. The geometrical considerations that lead to the definition of the Young's modulus  $E$  and the Poisson ratio

$\nu$  are identical, but since the stiffness tensor contains fewer entries, Hooke's law leads to

$$\begin{aligned}\epsilon_{xx} &= \frac{1}{\bar{E}} [\sigma_{xx} - \bar{\nu}\sigma_{zz}] , \\ \epsilon_{xz} &= \frac{1 + \bar{\nu}}{\bar{E}} \sigma_{xz} , \\ \epsilon_{zz} &= \frac{1}{\bar{E}} [\sigma_{zz} - \bar{\nu}\sigma_{xx}] ,\end{aligned}$$

where we denoted the corresponding two-dimensional elastic constants with a bar for clarity. From these relations, it is easy to deduce the following conversion rules:

$$\bar{E} = \frac{E}{1 - \nu^2} , \quad \bar{\nu} = \frac{\nu}{1 - \nu} . \quad (6.7)$$

The inverse relations have the form

$$E = \bar{E} \frac{1 + 2\bar{\nu}}{(1 + \bar{\nu})^2} , \quad \nu = \frac{\bar{\nu}}{1 + \bar{\nu}} \quad (6.8)$$

Of course, these conversion rules are only valid if the three-dimensional problem is posed in such a way that no contribution of the third dimension has to be taken into account. This is typically the case for plane strain and plane stress situations with transverse isotropy in one direction. We also remark that the usage of  $E$  and  $\nu$  as the only elastic constants implies the assumption of an homogeneous isotropic material.

## 6.2. Random Distribution of Spherical Holes

The first system under investigation is that of a two-dimensional solid isotropic body in a plane strain situation that contains randomly placed circular holes which are allowed to overlap. This system has already been investigated numerically by Day et al. [27]. We use this scenario to demonstrate the applicability of our numerical method to determine the effective elastic constants. For  $N$  spherical holes of radius  $r$  in the solid phase with area  $A$ , the true void concentration  $c$  is related to the void area ratio  $\tilde{c} = N\pi r^2/A$  according to the relation

$$c = 1 - \exp^{-\tilde{c}} , \quad (6.9)$$

which takes into account that the circles can overlap. The above relation can be easily understood from the following analysis: Assume that already the fraction  $c$  of the total area is covered by holes. Addition of holes with area  $dA$  leads to a change of the void concentration by

$$dc = \frac{(1 - c)dA}{A} , \quad (6.10)$$

where the factor  $1 - c$  takes into account that only the area  $(1 - c)dA$  covers parts of the solid phase. Integration of this relation then immediately leads to Eq. (6.9). Notice that this is conceptually the same idea as in the derivation of Eq. (6.5).

Our numerical simulations, which are based on the phase-field programs used in the previous chapters, are of course done with finite systems; here we use grid sizes of  $2047 \times$

1023 lattice units  $dx^2$ , and apply periodic boundary conditions horizontally and fixed displacements vertically. In this homogeneous system, we insert  $N$  spherical holes with radius  $r = 20dx$ , which are allowed to overlap. Note that in contrast to the previous chapters, we consider only *static* situations. This is due to the fact that neither the analytic approaches nor the finite element simulations treat the fully dynamical problem. In order to compare our newly obtained results against these methods, the phase-field dynamics are "frozen", corresponding to a vanishing kinetic coefficient. The concentrations obtained by the finite system simulations that we perform as a check agree perfectly with the prediction Eq. (6.9), as can be seen in Fig. 6.2. We then measure the average stresses

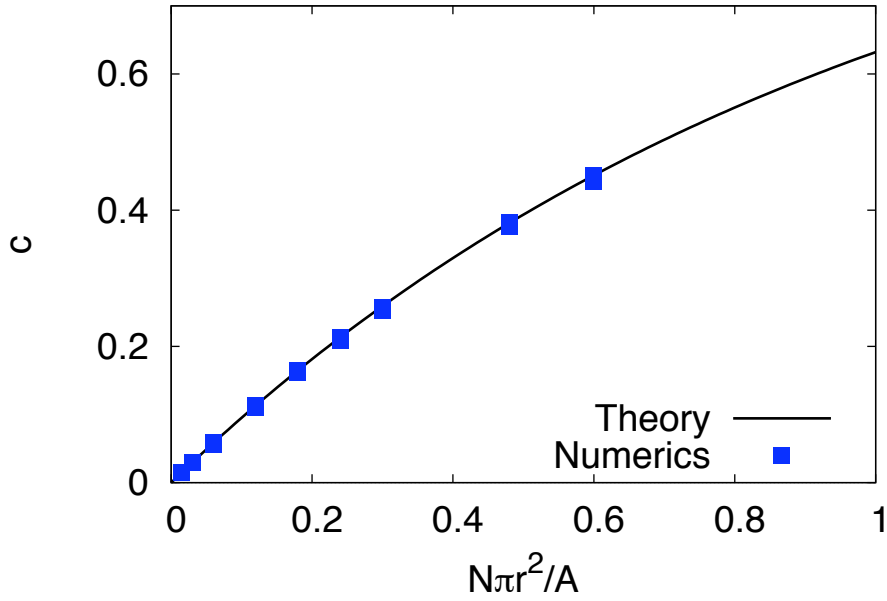


Figure 6.2.: Void concentration  $c$  as function of the total spherical hole area fraction, as obtained from the numerical simulations. The data are compared to the theoretical prediction Eq. (6.9).

in these systems as well. Notice that the system remains isotropic, and is therefore characterized by  $E_{eff}$  and  $\nu_{eff}$ . Since  $\bar{\nu}$  is a dimensionless quantity, we know that it cannot depend on  $E_{eff}$ , so we have  $\nu_{eff}(E_{eff}, c) = \nu_{eff}(c)$ .

Starting from the exact expression for a single inclusion [32], low-density expressions for the effective elastic constants can be derived in terms of the two-dimensional elastic moduli:

$$\bar{E}_{low} = \bar{E} - 3\bar{E}c + \mathcal{O}(c^2), \quad (6.11)$$

$$\bar{\nu}_{low} = \bar{\nu} + (1 - 3\bar{\nu})c + \mathcal{O}(c^2) \quad (6.12)$$

with the elastic constants  $\bar{E}, \bar{\nu}$  of the solid phase and the void concentration  $c$ . This result is attributed to numerous authors [56, 106].

The above expressions, truncated after the leading nontrivial order  $\mathcal{O}(c)$ , are approximate expressions known as the dilute distribution model [86] and predict a linear dependence of the effective moduli also for higher concentrations  $c$ . We also observe that the effective elastic modulus does not depend on the Poisson ratio, a behavior that is known to be exact and which is also reflected by this approximative theory. This theory predicts a "percolation point" at  $c = 1/3$ , from where on the effective elastic constant  $E$  becomes zero and the Poisson ratio equals  $\bar{\nu} = 1/3$  then. However, the true percolation threshold is at  $c = 0.68$  [5, 4] and therefore the dilute distribution model loses its predictive power for higher concentrations, *underestimating* the true stiffness. This tendency is increased by the fact that interactions can modify the percolation threshold, depending on whether they are attractive or repulsive [20].

Using the above low-density expressions (6.11) and (6.12), we can also derive another approximative model for the elastic constants in the framework of the differential medium theory explained above. According to equation (6.5), we start from

$$\frac{dE_{eff}}{dc} = \frac{-3E_{eff}}{1-c} \tag{6.13}$$

$$\frac{d\nu_{eff}}{dc} = \frac{1-3\nu_{eff}}{1-c} \tag{6.14}$$

and obtain as solution

$$E_{eff}(c) = \bar{E}(1-c)^3, \tag{6.15}$$

$$\nu_{eff} = \frac{1}{3} - \left(\frac{1}{3} - \bar{\nu}\right)(1-c)^3. \tag{6.16}$$

The first thing we note is that this model also reflects the independence of the two-dimensional elastic modulus on the Poisson ratio. Second, this model predicts percolation only for  $c = 1$ , i.e. if the solid phase has completely disappeared. It is obvious that this model therefore must be invalid for high cavity concentrations as well, *overestimating* the elastic constants of the heterogeneous system.

The dependence of the effective elastic modulus on the concentration as predicted by the theories, see Eq. (6.11) and Eq. (6.15), and as obtained by numerical simulations is shown in Fig. 6.3. The independence of  $E_{eff}$  on the Poisson ratio is clearly visible also in the numerics, where we checked this explicitly for  $\nu = 1/3$  and  $\nu = -0.7$ . We find that for the same random arrangement of circular holes the elastic constants match. Since we wanted to obtain a reasonable statistical averaging, we also performed repeated runs with different initializations. As we increase the void concentration  $c$ , one can clearly see that the scattering of the data points increases for higher concentrations, since larger clusters can form which can become comparable to the (finite) system size used in the simulations. Also, the relaxation time increases strongly with  $c$ , and therefore we refrain from presenting data for higher concentrations. In [27], Day et al. performed simulations based on an elastic spring network formulation for system setups analogous to ours. The comparison of our numerical results to the simulation data of Day et al. are also included in Fig. 6.3. The results for the independent numerical approaches are in reasonable agreement. In particular, all sets correctly reproduce the exactly known low density limit  $c \rightarrow 0$ . For higher concentrations, we obtain a higher effective elastic modulus than Day

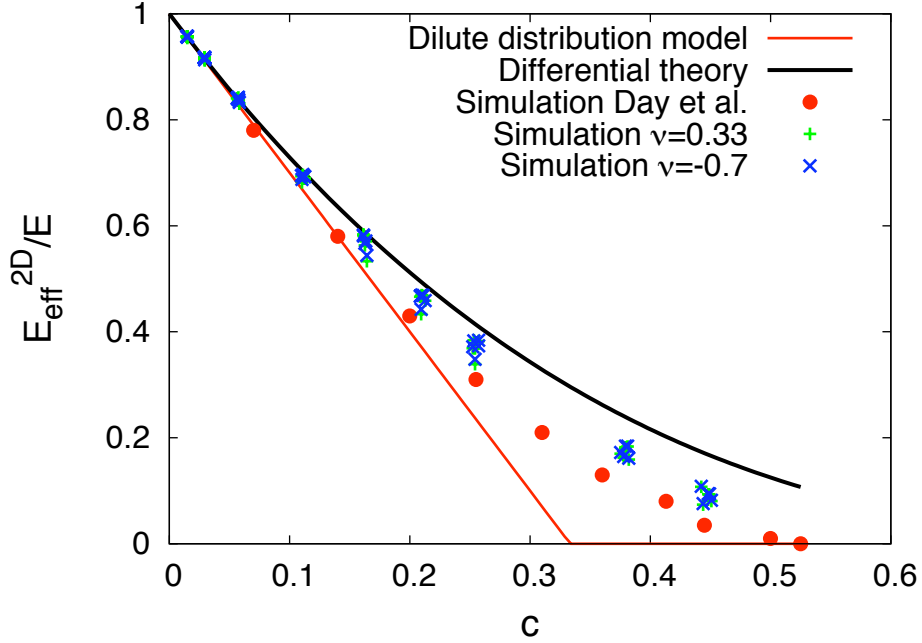


Figure 6.3.: Effective elastic modulus as function of the void concentration  $c$ . The plot shows numerical data for different Poisson ratios, in comparison to numerical results obtained by Day et al. The independence of the Poisson ratio is clearly visible.

et al., and we believe that this is a consequence of the considerably larger systems that we used.

Next, we compare the results of  $\bar{\nu}_{eff}$  to the approximative analytical expressions of the dilute distribution model and the differential theory. According to the numerical results, it seems that the differential theory gives a slightly better approximation, especially for materials with negative Poisson ratio, see Fig. 6.4. However, as we already noted, this theory must fail fundamentally above the percolation threshold.

The physical system we considered so far is that of a two-dimensional sheet that contains circular holes. Since the elastic modulus and the Poisson ratio decouple completely, this system is particularly convenient to solve. The effective three-dimensional elastic modulus however, does *not* have the property of being independent of the Poisson ratio. But with the results we obtained so far, we can easily give the solution for a three-dimensional system that contains long void parallel cylinders, by applying the conversion rules Eq. (6.8). This way, we obtain

$$E_{eff} = \frac{3E (c-1)^3 (c(8\nu-2)(c^2-3c+3) - 3(1-\nu))}{(c(4\nu-1)(c^2-3c+3) - 3)^2 (\nu+1)} \quad (6.17)$$

$$\nu_{eff} = \frac{c(4\nu-1)(c^2-3c+3) - 3\nu}{c(4\nu-1)(c^2-3c+3) - 3} \quad (6.18)$$

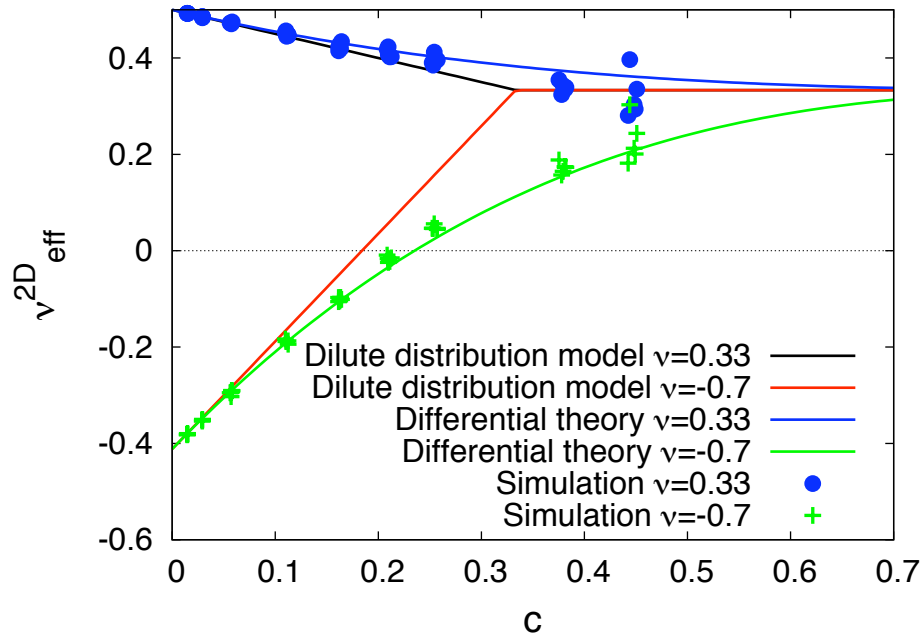


Figure 6.4.: Poisson ratio as function of the void concentration  $c$ . For  $\nu = 1/3$ , both, the dilute distribution model and the differential theory show fairly good agreement with the numerical results. For negative Poisson ratios, the differential theory coincides much better with the simulations.

A plot of the three-dimensional effective elastic modulus  $E$  as a function of the concentration  $c$  is shown in Fig. 6.5.

In fact, for negative Poisson ratios, the effective elastic modulus can first increase if the material is "weakened" by spherical holes. Negative Poisson ratios as low as  $\nu = -0.8$  have been experimentally observed in foam structures [72]. The counter-intuitive stability increase of the solid is due to the fact that peculiar boundary conditions have to be applied to avoid out-of-plane strain and the special microstructure that auxetics need to have, see Section 2.1.5. When measuring the elastic modulus under plane strain conditions in one direction, some other forces have to act in the orthogonal directions in order to fulfill the plain strain conditions. We would like to point out that the initial increase of the elastic modulus is only due just for the different representation of two- and three-dimensional elasticity and the special set of loading that is needed to generate the plane strain conditions.

### 6.3. Random Distribution of Elliptical Cracks

In [41], a problem related to the circular hole setup was investigated, namely that of infinitesimally thick ellipsoidal cracks. While this particular choice of shape allows to use exact results for ellipsoidal inclusions, it mimicks the flat, long shape of cracks; especially,



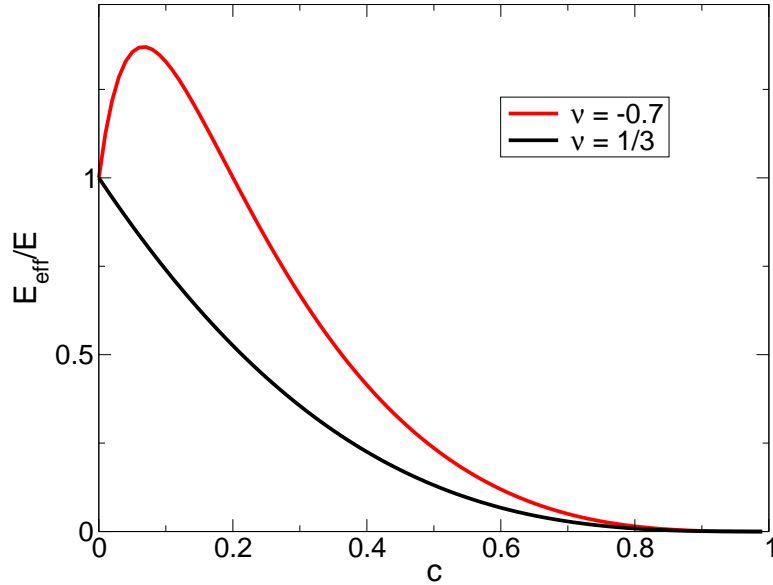


Figure 6.5.: Effective elastic modulus for a solid containing parallel cylindrical holes under plane strain conditions. Whereas for  $\nu = 1/3$ , a monotonic decrease of the effective modulus is observed, this is not true for auxetic materials. Here, the negative values of  $\nu$  lead to an initial increase of the effective strength.

the cracks have a vanishing volume fraction, in contrast to the circular voids considered in the previous section. Another issue to be addressed is the angular distribution of the cracks.

### 6.3.1. Crack Density Parameter

Cracks can weaken a material considerably even when their height is very small. It is therefore necessary to find a better suited measure of the crack density than the void concentration  $c$ . To do so, we consider a region of the  $x$ - $z$ -plane with total area  $A$  and  $N$  elliptic inclusion with aspect ratio  $e = a_z/a_x$ . In the limit  $e \rightarrow 0$ , this is equivalent to slit cracks. Please note that in contrast to [41], where the setup defined cracks along the  $x$ -axis in the  $y$ - $z$ -plane, we use the  $x$ - $z$ -plane instead in order to keep our notation and geometrical setup consistent. In addition to the porosity density parameter, an additional parameter has to be introduced in order to quantify the directional variability of the inclusions. Assuming that the cracks are arbitrarily rotated with an angle  $\theta \in (-\pi/2, \pi/2)$  around the  $y$ -axis, which is the axis of transverse isotropy here, their angular distribution is characterized by the order parameter

$$P = \langle \sin^2(\theta) \rangle. \quad (6.19)$$

It describes the distribution of cracks, where the values  $P = 0$  and  $P = 1$  correspond to a parallel arrangement of cracks along the  $x$ - or  $z$ -axis, respectively;  $P = 1/2$  means that

the cracks are randomly oriented in the plane, see Fig. 6.6. The volume fraction  $c$  of the inclusions is given by the number of cracks  $N$  times their area  $\pi a_x a_z$ , divided by the total area  $A$ :

$$c = \frac{\pi a_x a_z N}{A} = \frac{\pi e b^2 N}{A} = \alpha e \quad (6.20)$$

where we used  $a_x = b$  and  $e = a_z/a_x$  for the second equality. This results in the new dimensionless quantity

$$\alpha = \frac{\pi b^2 N}{A} \quad (6.21)$$

which effectively describes the crack density and respects the fact that they have a van-

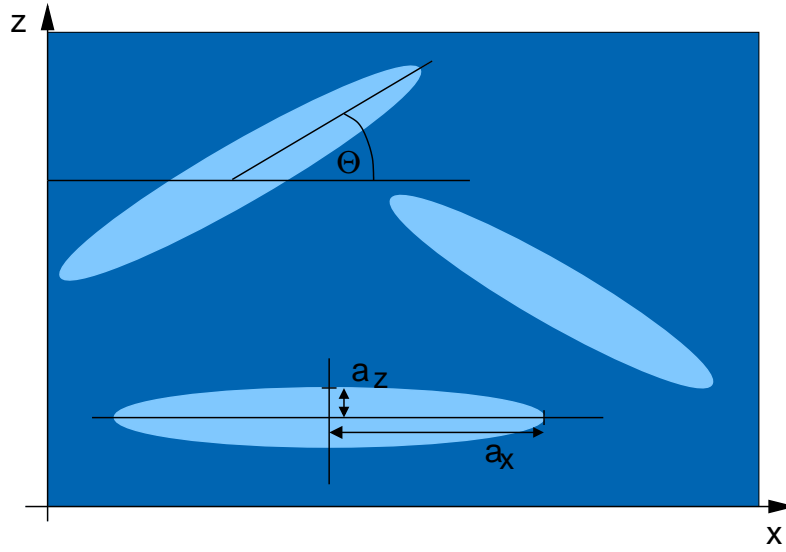


Figure 6.6.: In the case of an unordered system with  $P = 1/2$ , elliptic inclusions of equal length  $L = 2a_x$  and aspect ratio  $e = a_z/a_x$  are distributed at random positions and arbitrarily rotated with an angle  $\theta$  around the  $y$ -axis.

ishing volume fraction for  $e \rightarrow 0$ .

### 6.3.2. Iterated Homogenization for Randomly Oriented Cracks

In the following, we will outline roughly the line of reasoning that was taken in [41], before we will present a simpler approach to the considered problem of randomly oriented cracks. The main result is that for  $P = 1/2$ , the effective elastic modulus and the poisson ratio decay exponentially with the density parameter  $\alpha$  in the case of arbitrarily oriented cracks of the same length  $L = 2b$ :

$$E_{eff} = \frac{E[2\nu + (1 - \nu)e^\alpha]}{[\nu + (1 - \nu)e^\alpha]^2(1 + \nu)} \quad (6.22)$$

$$\nu_{eff} = \frac{\nu}{\nu + (1 - \nu)e^\alpha} \quad (6.23)$$

In [41], the case of a parallel crack arrangement is not treated, as it is not easily possible with the presented method. We will show in section 6.4 that for parallel cracks, the decrease of the effective elastic constant follows a power law instead.

The starting point to the homogenization approach is provided by the so-called ESHELBY TENSOR [85]. It contains all physical information required to predict the mechanical interaction between the inclusion and the outer solid matrix under external load. For inclusions that support elastic stresses, the internal stress and strain fields are constant for constant external strain fields. If the inclusion is a void, the Eshelby tensor  $\underline{\underline{S}}$  provides the relationship between the external strain  $\underline{\underline{\epsilon}}_{ext}$  and the induced strain  $\underline{\underline{\epsilon}}_{int}$ :

$$\underline{\underline{\epsilon}}_{int} = (\underline{\underline{I}} - \underline{\underline{S}})^{-1} \underline{\underline{\epsilon}}_{ext} \quad (6.24)$$

where  $\underline{\underline{I}}$  denotes the identity tensor. For a crack that has an elliptical shape in the  $x$ - $z$ -plane and is extended in along the  $y$ -plane, the Eshelby tensor depends only on the aspect ratio  $e = a_z/a_x$  with the semiaxes  $a$  along the corresponding direction, and on the poisson ratio of the surrounding matrix [85].

Let us address the random orientation case with  $P = 1/2$  first. A solid with a two-dimensional arbitrary orientational distribution of parallel slit cracks normally exhibits the symmetry of an orthorhombic crystal: the different orientation of the cracks along the  $x$ - and  $z$ -axis leads to different elastic behavior in these directions. The third inequivalent direction stems from the alignment along the  $y$ -axis. The corresponding effective stiffness tensor has 9 independent entries that depend on the Young's modulus  $E$ , the Poisson ratio  $\nu$ , the crack density parameter  $\alpha$  and the orientation order parameter  $P$ .

Starting with the hypothesis of low crack density so that the cracks do not interact, the effective stiffness tensor of a non-isotropic, 3d orthorhombic system can be explicitly given in Voigt notation, see section 2.1.5, but keeping all four indices for better readability:

$$C_{eff} = \begin{pmatrix} C_{1111} & C_{1122} & C_{3311} & 0 & 0 & 0 \\ C_{1122} & C_{2222} & C_{2233} & 0 & 0 & 0 \\ C_{3311} & C_{2233} & C_{3333} & 0 & 0 & 0 \\ 0 & 0 & 0 & C_{1212} & 0 & 0 \\ 0 & 0 & 0 & 0 & C_{2323} & 0 \\ 0 & 0 & 0 & 0 & 0 & C_{3131} \end{pmatrix} \quad (6.25)$$

The closed form expressions for  $P = 1/2$ , depending on the parameters  $E$ ,  $\nu$  and  $\alpha$ , are

[41]:

$$\begin{aligned}
 C_{1111} &= \frac{E[\alpha^2(1+\nu)(1-\nu)^2 + 2\alpha(1-\nu) + 1-\nu]}{D} \\
 C_{2222} &= \frac{E(1-\nu)(1+\alpha)}{D} \\
 C_{3333} &= \frac{E(1-\nu)(1+\alpha)}{D} = C_{2222} \\
 \\ 
 C_{1122} &= \frac{E\nu(1+\alpha(1-\nu))}{D} \\
 C_{3311} &= \frac{E\nu(1+\alpha(1-\nu))}{D} = C_{1122} \\
 C_{2233} &= \frac{E\nu}{D} \\
 \\ 
 C_{1212} &= \frac{2E}{(2+\alpha)(2+2\nu)} \\
 C_{3131} &= \frac{2E}{(2+\alpha)(2+2\nu)} = C_{1212} \\
 C_{2323} &= \frac{E}{(1+\alpha(1-\nu))(1+\nu)}
 \end{aligned} \tag{6.26}$$

where the denominator  $D$  is given by

$$D = [\alpha^2(1-\nu)^2 + 2\alpha(1-\nu)^2 + 1 - 2\nu](1+\nu).$$

But since the material is transversely isotropic along the  $y$ -axis and a random orientation in the  $x-z$ -plane is assumed, the material becomes transversely isotropic. Under the conditions of plane stress or plane strain, the material appears to be isotropic and can be fully described by the two material constants  $E_{eff}$  and  $\nu_{eff}$ . Giordano and Colombo then arrive at their final result Eq. (6.22) and Eq. (6.23) via the iterated homogenization method, which allows them to drop the assumption of low crack density.

We would like to present an equivalent, but much simpler way to derive the above results. Our derivation shows clearly that the iterated homogenization method cannot predict percolation and must therefore overestimate the real effective elastic modulus.

In three dimensions, Hooke's law, written in terms of  $E$  and  $\nu$ , has the form

$$\sigma_{ij} = \frac{E}{1+\nu} \left( \epsilon_{ij} + \frac{\nu}{1-2\nu} \delta_{ij} \epsilon_{kk} \right). \tag{6.27}$$

Reduction to a plane-strain situation in the  $x-z$ -plane means

$$\begin{aligned}
 u_y &= 0, u_y = u(x, z), u_z = u(x, z) \\
 \Rightarrow \epsilon_{xx}, \epsilon_{zz}, \epsilon_{xz} &\neq 0, \text{ all other components vanish,}
 \end{aligned}$$

so we obtain

$$\begin{pmatrix} \sigma_{xx} \\ \sigma_{zz} \\ \sigma_{zx} \end{pmatrix} = \frac{E}{(1+\nu)(1-2\nu)} \begin{pmatrix} 1-\nu & \nu & 0 \\ \nu & 1-\nu & 0 \\ 0 & 0 & 1-2\nu \end{pmatrix} \begin{pmatrix} \epsilon_{xx} \\ \epsilon_{zz} \\ \epsilon_{zx} \end{pmatrix}. \quad (6.28)$$

On the other hand, we have

$$\sigma_{ij} = C_{ijkl}\epsilon_{kl},$$

which leads to

$$\sigma_{xx} = C_{1111}\epsilon_{xx} + C_{1133}\epsilon_{zz} + \underbrace{C_{1113}}_{=0}\epsilon_{zz}.$$

Comparing the coefficients, one can easily read off

$$C_{1111} = \frac{E(1-\nu)}{(1+\nu)(1-2\nu)} \quad (6.29)$$

$$C_{1133} = \frac{E\nu}{(1+\nu)(1-2\nu)} \quad (6.30)$$

$$C_{1313} = \frac{E}{1+\nu}. \quad (6.31)$$

These equations can be used to express the Poisson number  $\nu$  in terms of the coefficients:

$$\begin{aligned} \frac{C_{1133}}{C_{1111}} &= \frac{\nu}{1-\nu} \\ \Leftrightarrow \nu &= \frac{C_{1133}}{C_{1133} + C_{1111}}. \end{aligned} \quad (6.32)$$

Using this result, the Young's modulus can also be expressed in terms of the Hooke's tensor components:

$$E = \frac{(2C_{1133} + C_{1111})(C_{1111} - C_{1133})}{C_{1133} + C_{1111}}. \quad (6.33)$$

We start solving for  $\nu$  first, since the Poisson ratio is a dimensionless quantity and cannot depend on  $E$ . Since the components of the effective stiffness tensor  $C_{ijkl}$  still depend on the crack density parameter  $\alpha$ , we also employ the initial assumption of low density by linearization in  $\alpha$  to obtain

$$\nu_{eff} = \nu + \nu(\nu - 1)\alpha + \mathcal{O}(\alpha^2). \quad (6.34)$$

Applying the conversion rule Eq. (6.8) leads to the low density expression

$$\bar{\nu}_{eff} = \frac{\bar{\nu}^2 + \bar{\nu} - \bar{\nu}\alpha}{\bar{\nu} + 1 + \bar{\nu}\alpha}. \quad (6.35)$$

The differential equation to be solved is now simply

$$\frac{d\bar{\nu}_{eff}}{d\alpha} = -\bar{\nu}_{eff}, \quad (6.36)$$

which is integrated with the initial condition  $\bar{\nu}_{eff}(0) = \bar{\nu}$  to yield

$$\bar{\nu}_{eff}(\alpha) = \bar{\nu}e^{-\alpha}. \quad (6.37)$$

The same procedure can now be applied to determine the Young's modulus: starting from Eq. (6.33), the low density expansion reads

$$E_{eff} = E + \frac{E(2\nu^2 - \nu - 1)\alpha}{1 + \nu}. \quad (6.38)$$

Again, the conversion rules Eq. (6.7) and the result Eq. (6.37) are applied to obtain the two-dimensional representation

$$\bar{E}_{eff} = -\frac{E(-1 - 3\bar{\nu} - 2\bar{\nu}^2 + \alpha + 3\alpha\bar{\nu})(1 + \nu e^{-\alpha})^2}{(1 + \bar{\nu})^3(1 + 2\bar{\nu}e^{-\alpha})} \quad (6.39)$$

of the effective elastic module. The partial derivative at  $\alpha = 0$  gives just

$$\frac{d\bar{E}_{eff}}{d\alpha} = -\bar{E}_{eff}, \quad (6.40)$$

which of course has the simple solution

$$\bar{E}_{eff}\alpha = \bar{E}e^{-\alpha}, \quad (6.41)$$

when the initial condition  $\bar{E}_{eff}(0) = \bar{E}$  is used. Converting the results back to three dimensions, one obtains the formulas Eq. (6.22) and Eq. (6.23).

At this point, several remarks are at order:

- The first is that the result obtained for the full plane strain crack problem by the fully three-dimensional homogenization and the homogenization in two dimensions which are then converted in the three-dimensional representation are equivalent and differ only by the representation of two- and three-dimensional theory of elasticity. This is due to the transverse isotropy of the original three-dimensional problem, which means there are two equivalent ways to tackle the elastic problem: The first is to do the homogenization in the fully three-dimensional representation, as was done in [41]; the conversion to two dimensions then leads to the same  $\bar{E}_{eff} = \bar{E} \cdot e^{-\alpha}$  and  $\bar{\nu}_{eff} = \bar{\nu} \cdot e^{-\alpha}$ . The alternative consists of doing the calculation for the two-dimensional problem, which leads to simpler expressions, and obtain the three-dimensional result by conversion Eq. (6.7), if still desired. The two-dimensional approach using Young's modulus and the Poisson ratio as elastic constants is especially appealing, since the differential equations that need to be solved decouple completely. The fact that this is true for the iterated homogenization scheme for circular holes as well as for randomly oriented cracks hints at the possibility that this could be a very general feature.
- Secondly, the homogenization method as outlined in [41] becomes much more involved for any other case than  $P = 1/2$ . While the effective stiffness tensor still respects the possible orthorhombic symmetry, the homogenization method is built on

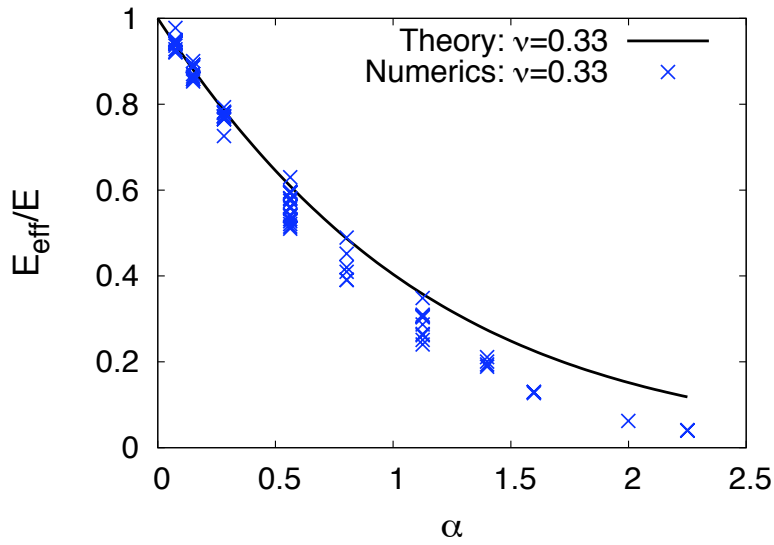


Figure 6.7.: Effective elastic modulus as function of the crack density for plane strain loading,  $\nu = 1/3$ , for several random distributions ( $P = 1/2$ ) of cracks of equal length.

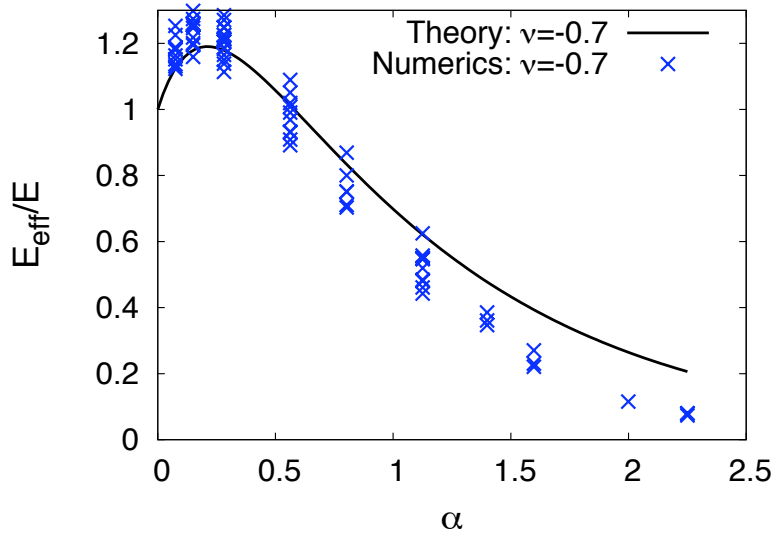


Figure 6.8.: Effective elastic modulus as function of the crack density for plane strain loading,  $\nu = -0.7$ , for several random distributions ( $P = 1/2$ ) of cracks of equal length. The initial stiffness increase predicted by the differential homogenization theory is clearly visible. For higher crack densities, the theory overestimates the effective elastic modulus significantly.

the assumption that the cracks are added consecutively into an *effectively isotropic* matrix. For any other order parameter than  $P = 1/2$ , this would no longer be true. While it might be possible to extend the iterated homogenization scheme to include anisotropy, one would get as many coupled homogenization equations as there are independent elastic parameters, leading to a much more involved system of coupled differential equations.

- The observed *increase* of the effective elastic modulus for auxetic materials under plane strain can only be observed in three dimensions. In two dimensions, the equations decouple, and  $\bar{E}_{eff}$  does not depend on  $\bar{\nu}$ . This initial increase is also not restricted to cracks, the previously treated circular cylinder problem exhibits the same feature, even though the solution of the homogenization equation shows a power law decay instead of an exponential decay. This difference stems from the fact that the homogenization equation for the circular holes Eq.(6.10) still contains the corresponding density parameter  $c$ , while this is not the case for cracks.
- Furthermore, Eq. (6.41) and Eq. (6.37) show clearly that the homogenization approach cannot take into account percolation effects. However, for large  $\alpha$ , which corresponds to high crack densities, percolation occurs. For the two-dimensional system under consideration and a random arrangement of infinitely thin cracks with equal length and equally distributed angular orientations, the percolation threshold for sticks of the same length is  $\alpha_p \approx 4.49$  [95]. This implies that the exponential decay of the effective elastic modulus according to Eq. (6.22) and Eq. (6.23) can describe only an intermediate behavior; beyond the above threshold, a single long crack penetrates the whole system, and the effective elastic modulus must be exactly zero.

Apart from the above analytical calculations, we investigated the case of randomly oriented cracks of equal length also numerically for plane strain loading using finite difference relaxation methods, see Appendix A.5. This was done by distributing the crack centers randomly over the sample and then assigning a random angle to each crack. The number of cracks was kept constant at 100 cracks with a length of ten grid points each; the cracks were allowed to overlap and the size of the system was varied to obtain the respective values of the crack density parameter  $\alpha$ . For each value of alpha, up to 10 runs with different initial distributions were performed. The results are shown in Figs. 6.7 and 6.8. For low crack densities, the numerical results agree with the prediction Eq. (6.22) in [41], but for higher values they seem to be systematically lower, probably due to prospective percolation. The scatter in the numerical data shows the impact that the difference in microstructure can have on the effective elastic modulus of the total system. Note that most numerically obtained values are considerably lower than the analytical prediction. This demonstrates that the iterated homogenization method must *overestimate* the effective elastic moduli since it cannot take percolation effects into account.

## 6.4. Asymptotic Behavior of Parallel Cracks

The only arrangement where percolation does not occur is that of a parallel alignment of all cracks [6], which is a situation that can appear quite naturally, as will be explained



below. Thus only here a nontrivial asymptotic behavior for high crack densities exists.

In the previous section, we assumed an equal probability for all possible crack orientations. The situation of random orientational crack distribution corresponds to the case  $P = 1/2$  and an approximation scheme for the effective elastic constants was given by the differential homogenization method. For higher crack densities, a crack network forms and the system breaks due to percolation.

If, however, the system is stretched in only one direction (which we define to be the  $z$ -direction), the situation is different. We start with considering an initially uncracked solid body. Stretching it in the  $z$ -direction leads to a uniform strain  $\epsilon_{zz}^{(0)}$ , which is obviously a non-equilibrium situation, since the elastic energy density  $w_{el} \sim E\epsilon_{zz}^{(0)}$  could be released if cracks were present. In the ideal case, one crack would traverse the whole system and the whole elastic energy was released at the cost of the surface energy of the separated crack interfaces. We will not discuss the possible nucleation process here, but if several cracks form, they will be aligned perpendicular to the  $z$ -axis, since this maximizes the elastic energy release rate. For low crack densities, the effective constants have also been calculated in [41], corresponding to an order parameter of  $P = 0$  for parallel arrangement. In particular, one obtains

$$C_{3333}^{low} = \frac{(1 - \nu)E}{D} \quad (6.42)$$

with the denominator now having the form

$$D = [(1 - \nu)^2 + 2(1 - \nu)^2\alpha + 1 - 2\nu](1 - \nu). \quad (6.43)$$

However, for higher crack densities, the differential homogenization approach is not well suited, since the parallel cracks cause the system to be anisotropic. Therefore, the assumption that cracks are iteratively introduced into a system that can be described through effective *isotropic* elastic constants is no longer justified.

With the following scaling argument [15] that originated in the investigations of dynamic crack coarsening processes, the high density behavior for parallel cracks can still be assessed, however. The first important observation is that if the cracks are assumed to be very narrow and parallel, no percolation will occur [6]. We assume that in the  $xz$ -plane, the cracks are all aligned in the  $x$ -direction. So, it is immediately clear that any stretching of the material in this  $x$ -direction does not open the cracks, which means that e.g.  $C_{1111}^{eff} = C_{1111}$ , hence, the strain tensor is homogeneous in the whole sample and unaffected by the cracks.

We start with looking at high crack densities,  $\alpha \rightarrow \infty$ , and see that two different lengthscales are important for the description of the problem at hand, the length  $L$  of the cracks and the average vertical distance  $h$  between them. For high crack densities  $\alpha$ , the vertical distance  $h$  between neighboring cracks is smaller than the average crack length  $L$ , and the relation between the two characteristic length scales can be given through  $\alpha$  only, so we obtain  $h \sim L/\alpha$ . If the cracked body is subjected to tensile loading perpendicular to the cracks, the solid regions between two cracks can be understood as a thin bent plate of a width proportional to  $L$  and thickness  $h$ . The opening of the cracks is the displacement  $u_z$ . The stress of a thin bent plate scales as [73]:

$$\sigma_{zz} \sim \frac{Eh^3}{1 - \nu^2} \frac{\partial^4 u_z}{\partial x^4}. \quad (6.44)$$

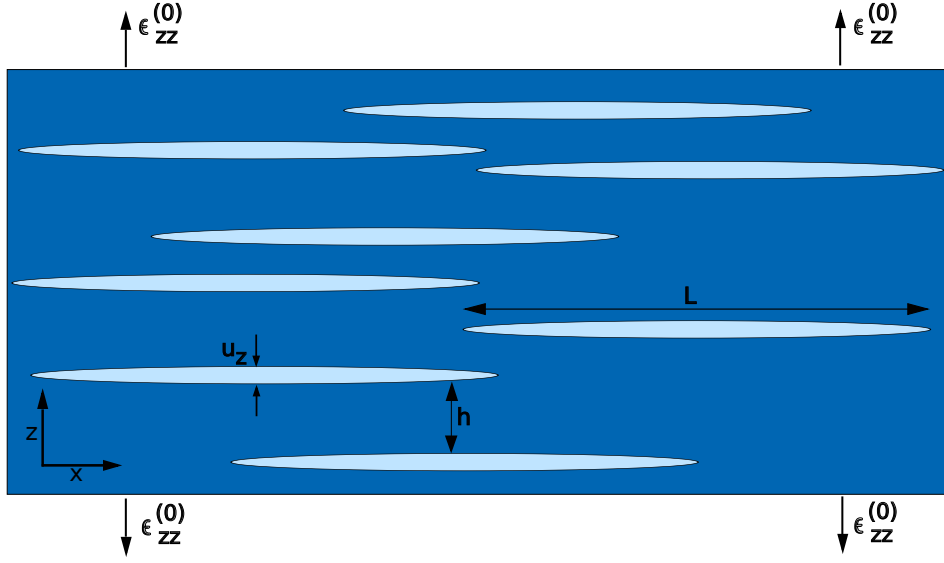


Figure 6.9.: Random arrangement of parallel cracks. The average crack length is  $L$ , and the average vertical distance between neighboring cracks is denoted by  $h$ .

With this equation, it follows readily that the average stress and the opening  $u_z$  have to scale like

$$\langle u_z \rangle \sim \langle \sigma_{zz} \rangle \frac{(1 - \nu^2)L^4}{Eh^3}. \quad (6.45)$$

The total displacement is distributed among the opening of all cracks, which relax the material around them. Since for this loading, all other average strain components vanish [73], the average strain  $\langle \epsilon_{zz} \rangle$  is simply given by

$$\langle \epsilon_{zz} \rangle = \frac{\langle u_z \rangle}{h} \quad (6.46)$$

Plugging this into Eq. (6.45), we finally obtain for the case  $\alpha \gg 1$

$$\langle \sigma_{zz} \rangle \sim \langle \epsilon_{zz} \rangle \frac{E}{(1 - \nu^2)\alpha^4}. \quad (6.47)$$

In other words, the relevant elastic constant

$$C_{3333}^{eff} = \frac{\langle \epsilon_{zz} \rangle}{\langle \sigma_{zz} \rangle} \quad (6.48)$$

decays as a power law

$$C_{3333}^{eff} \sim C_{3333}\alpha^{-4}. \quad (6.49)$$

That Eq. (6.49) holds analytically was shown in [15] and a more detailed derivation for the case of a regular array of parallel cracks is given in Appendix A.4. It also holds for situations where the cracks have unequal lengths, with an average length  $L$ . Details of the length distribution function can affect only the numerical prefactor of the above prediction in the limit  $\alpha \rightarrow \infty$ .

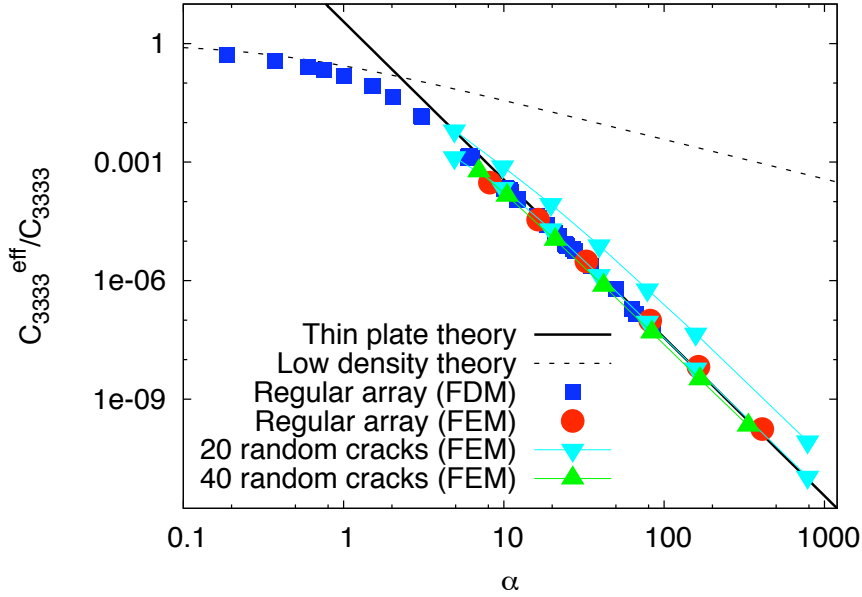


Figure 6.10.: Scaling behavior of the effective elastic constant  $C_{3333}^{eff}$  as a function of the crack density  $\alpha$  for a parallel arrangement of cracks in logarithmic representation. For a regular arrangement of cracks, the agreement of the numerical simulations with thin plate theory is excellent. If the cracks are placed at random positions, they still exhibit the same power law scaling behavior.

We carried out various numerical investigations for the different crack arrangements, using both the finite difference elastic solver (FDM) used in the previous chapters, and, as an independent numerical approach, finite element methods (FEM) based on the open source package FREEFEM++ [51]. The results can be seen in Fig. 6.10. For the regular arrangement of cracks, only systems with relatively few cracks need to be simulated due to the spatial periodicity. The numerical prefactor was chosen such that it corresponds to the specific overlap-gap ratio of  $g = 1/2$  as explained in Appendix A.4.

For the random case, the crack centers are placed randomly within the system. The relative crack arrangement is then kept fixed while the height of the system is rescaled in order to change the value of the crack density parameter  $\alpha$ . The main difference to the previous case is that the overlap-gap ratio  $g$ , which is a dimensionless parameter, would have to be determined statistically. Since it enters only in the numerical prefactor of the effective constants and does not affect the scaling behavior, we refrained from measuring or specifying it. Obviously, the exact results have to depend on the specific configuration, and the differences would only disappear in the limit  $N \rightarrow \infty$ . Since the scaling holds very well for each configuration, it reflects the true ensemble average in an infinitely large system. Two cases with  $N = 20$  cracks are shown here to exemplify that different geometrical setups can affect the numerical prefactor, but not the scaling behavior. We checked that systems with different numbers of cracks exhibit the same scaling behavior

and show only representative results for  $N = 20$  and  $N = 40$  cracks.

Fig. 6.10 reveals that the low density theory can clearly not describe the material behavior properly if higher crack densities are reached. The expected crossover behavior between the low density theory and the asymptotic scaling for high crack densities is well visible. We also see that the results of the finite difference and the finite element calculations coincide extremely well. While the finite element method is computationally more efficient than the simple relaxation solver, the geometrical description is easier with finite differences, since e.g. intersections with boundaries (or crack overlap for the case of randomly oriented cracks, as discussed in the previous sections) do not require separate treatment.

## 6.5. Conclusion

In this chapter, we studied the effective moduli of solids that contains spherical and crack-like cavities. A widely used analytical approximate approach, the differential homogenization method, was presented. We tested this technique first on the problem of a two-dimensional sheet containing circular holes. The analytical predictions were compared to numerical result we obtained with our finite-difference based phase-field code. Additionally, we implemented a finite element description to simulate the setup. The results of the two numerical methods were in excellent agreement. The comparison of the numerical data with the analytics revealed that while the linearized dilute distribution model underestimates the effective elastic constants but can predict percolation (albeit for too low crack densities), the differential homogenization method tends to overestimate them. The numerical results were in good agreement with previous results found in the literature; the difference is due to the much larger systems we simulated. Extending these results to three dimensions, we found that the effective elastic constants can show an initial increase under plane strain loading if the material has a negative Poisson ratio.

A conceptually very similar approach was used in [41] for randomly oriented cracks in three dimensions and an exponential decay of the effective elastic constants was predicted. The authors also observed the initial increase of stiffness for auxetic materials. We could show that by exploiting the present symmetries, the treatment of the corresponding two-dimensional problem yields identical results in a simpler way. The inability of the homogenization method to predict percolation becomes evident, and it again overestimates the remaining stiffness of the cracked material.

In addition, we also treated the case of parallel oriented cracks. Here, no percolation occurs, but the simple homogenization approach cannot be used since the crack arrangement renders the material anisotropic. By simple scaling arguments, we could show that the effective elastic constants have to decay as a power law instead of an exponential function. This analytical result was confirmed by large scale numerical simulations.

Our results show that the effective elastic constants of multicroaked material depend sensitively on the geometrical setup. We claim that the treatment of the multicroack problem in two dimensions is, whenever applicable, advantageous, since the equations for the Young modulus and the Poisson ratio decouple, which seems to be a very general feature. It is of notable interest that the scaling prediction for parallel cracks is complementary to conventional homogenization theories, as it becomes accurate for *increasing*

## 6.5. CONCLUSION

---

crack densities.

## 7. Summary

This thesis describes the behavior of cracks and pores under the influence of elastic and curvature effects. In a continuum theory approach, these structure deformations are treated as free moving boundaries. The Grinfeld instability provides the link between the chosen pattern formation description and conventional fracture process theory. Both have their origin in a competition between the release of elastic energy and the increase of surface energy. The deep notches that form in the late stage of this morphological instability are comparable to fast growing cracks in many aspects. By incorporating elastodynamic effects into the theory, the usual unphysical finite time cusp singularity in the late stage of the Grinfeld instability can be overcome, making the simultaneous self-consistent selection of a tip radius scale and the propagation velocity possible. The starting point of our investigations is given by well established sharp interface equations that include only linear dynamical elasticity and non-equilibrium kinetic theory. We concentrated on two different material transport processes, namely surface diffusion and phase transition dynamics. Both transport processes require the dynamical evaluation of the chemical potential and a numerical solution of the elastodynamic equations.

Our primary method of choice to tackle fully time-dependent free moving boundary problem is the phase-field method. It avoids explicit interface tracking and is versatile enough to deal even with topological changes. It does so by spreading out the formerly sharp interfaces over a region of finite width, allowing to set up an identical set of coupled partial differential equations for the whole computational domain which are then solved numerically. This convenient description comes at the cost of introducing the interface width as a new purely numerical length-scale. Since the phase-field model does not yield an exact representation of the original sharp interface problem anymore, it has to be ensured that the original interface problem is recovered in the asymptotic limit when the numerical interface width vanishes in comparison to all other physically relevant length-scales.

The first material transport process we focused on was surface diffusion, which has long been assumed to be responsible for pore movement and the Grinfeld instability. While being comparatively slow for flat surfaces, it can be fast enough for corrugated surfaces of stressed material to even drive fast crack propagation. Its modeling leads automatically to mass conservation of each phase. One important result of this thesis is that phase-field modeling of surface diffusion is less trivial than it appears at first sight, as the requirement for the phase-field method to converge to the desired sharp interface equations lead to subtle, but severe implications. We could show analytically that the intuitive approach, which has been widely used in the literature, for constructing a phase-field model for surface diffusion fails (section 3.3). This standard approach, which consists of using the chemical potential to define a current, involving its gradient, and taking the divergence of

---

this current as the time derivative of the phase-field, reproduces only the *equilibrium limit* correctly. For *non-equilibrium* situations, this standard scalar model does not reduce to the desired sharp interface equations, so the traditional scalar mobility (SM) model turns out to provide an uncontrolled approximation to the dynamics.

Two completely new models, the LOCALLY CONSERVED TENSORIAL MODEL (LCT) (section 3.5) and the GLOBALLY CONSERVED TENSORIAL MODEL (GCT) (section 3.6), were developed that are not flawed by the above error and ensure the correct asymptotic behavior. The key to the model development was to exploit the anisotropy of the diffusion process along the interface by making the mobility a tensorial quantity instead of a scalar one. While we show that the straightforward approach utilizing a tensorial mobility has to fail in a drastic way, we were able to modify the tensorial mobility in such a way that the obtained models show the correct asymptotic behavior.

We found one model in the literature (section 3.7), that was not subject of the aforementioned flaw; it introduced an additional diverging term to the chemical potential that had no physical motivation and which, according to the authors' claim, only stabilized the numerics. Our analysis showed, however, that this term does in fact induce the correct asymptotic behavior, even though it does not exploit the geometrical aspects of the surface diffusion process.

All four models were implemented and thoroughly compared to assess the relative merits of each approach for several different situations. One important aspect was numerical stability, especially in stabilizing and keeping the correct interface profile for the transition region (Figs. 4.2–4.9). An advanced test of the correct modeling was provided by the evolution of an elliptical inclusion. Subject only to free curvature driven surface diffusion, the ellipse should morph to a circle of the same area. Here, the analytic result that the scalar mobility model provides the correct dynamics only in the limit of vanishing curvature could be seen clearly: all models with correct asymptotic behavior reproduced the circle with the correct radius, while the SM model does so only asymptotically for infinitely large ellipses (Fig. 4.12).

We could also explore the nonequilibrium regime for all models by coupling the surface diffusion process to elastic fields, which can then provide an external driving force. Exposing an elliptical pore to external elastic loading lead to the expected slit-like form of the inclusion (Fig. 4.14), indicating that crack growth due to surface diffusion is possible. For a quantitative analysis, we chose the Grinfeld instability as a highly nontrivial setup. The Grinfeld instability constitutes the link between pattern formation processes and conventional fracture mechanics; additionally, it is one of the rare cases where analytic results are available for comparison. All models could reproduce the spectrum of the instability very well, with the SM model again clearly showing the least quantitative agreement to the analytic expectation (Fig. 4.18). The first of our newly developed models, the LCT model, is most efficient in suppressing the unwanted diffusion perpendicular to the interface. This analytically desirable property makes the model numerically less robust for situations where curvatures are small or the diffusion along the interface is not sufficiently fast. Our second new model, the GCT model, relaxes the strict requirement of local matter conservation, enforcing it only on a global scale. It proves to be extremely accurate, versatile and able to deal with variations of the interface width very well, making it the simulation method of choice in most cases.

---

A severe disadvantage of modeling crack propagation by surface diffusion are the high order equations that require substantial numerical effort. We therefore derived another phase-field model which is based on a non-conservative phase transition process instead, where a stressed solid phase releases the stored elastic energy by transforming into a softer, "broken" phase. While this model is originally intended to describe solid-solid transformations, it can also be used to model dynamic fast crack propagation if the soft phase is modeled as an elastic vacuum. Since our model also includes the fully dynamical theory of elasticity, we can investigate fast fracture processes and the same selection principles as for surface diffusion apply.

The phase transition phase-field model we present can be derived from variational principles and converges to the desired sharp interface limit without the problems encountered in the surface diffusion case. Our simulations show that it describes the complicated tip behavior and the elastic far-field behavior correctly, also allowing the numerical extraction of quantities like the stress intensity factor (Fig. 5.7). However, despite the benign asymptotic behavior of the phase-field model, we showed clearly that finite-size effects and insufficient separation of the tip radius and the numerical phase field interface width can strongly influence the numerical results. As a central result, we present an extrapolation technique that enables us to remedy this problem in a systematic manner. In a two step process, we extrapolate the obtained data first to infinite system sizes and then to the limit of vanishing interface widths. The necessary large scale simulations required that the simulation program was parallelized to make efficient use of the supercomputers JUMP, JUBL and JUGENE, which are operated at the Research Center Jülich; we obtained an excellent scaling behavior up to several thousand processors. Our extrapolated values were then compared to the results of a recently developed sharp interface description based on a multipole expansion technique [97] with the *same* underlying sharp interface equations. The comparison exhibited a very convincing agreement between the completely unrelated methods (Fig. 5.11). We can confirm that the sharp interface model has a regime in which the crack reaches a steady state in which it grows with speeds comparable to, but considerably slower than the Rayleigh speed, in agreement with experimental observations. This is also in agreement with results from molecular dynamics simulations and experiments. Treating the crack as a fully time dependent free boundary problem, both the propagation velocity and the crack shape are determined in a fully self-consistent manner. We also find the tip velocity to be a weakly decaying function of the external driving force as tip blunting is the preferred mechanism to release the elastic energy (Fig. 5.12).

The flexibility of the phase-field method allows us to explore the parameter range of higher elastic driving forces, where steady state propagation no longer persists. This unstable regime is not accessible to the multipole expansion technique, because the assumption of steady state growth is implicitly built into the method. Here, we find a branching instability, where the crack splits in two due to a secondary Grinfeld instability at the blunt tip, and one of the two crack branches outgrows the other (Fig. 5.13).

Structures that are subjected to external loading often contain many small cracks already, which can weaken the structure substantially, depending on the initial crack density. It is therefore important to have reliable schemes to estimate the effective elastic behav-



---

ior of such multi-cracked materials. Two analytical approximation schemes, the effective medium theory and the differential homogenization method, are frequently used in the literature to predict the elastic behavior. Since the behavior of cracks depends on the local elastic fields, which in turn depend sensitively on the geometric crack distribution, it is a priori unclear how important interaction effects are and how the analytical approaches include them. Since our finite-difference based phase-field code could faithfully reproduce the behavior of a single crack, we compared simulations of static inclusions with the predictions we obtained with the effective medium theory and the differential homogenization method. As an additional test, we performed finite element simulations, which were always in good agreement with the results obtained by the phase-field calculations. This was done for several two- and three-dimensional systems. We could show that it is favorable for the analytic treatment to convert plane strain problems into a two-dimensional representation wherever possible, since the resulting equations are much simpler to treat analytically. In all cases, we found that the effective medium theory underestimates the stiffness of the system, while the differential homogenization overestimates it. For a two-dimensional sheet containing circular holes, our numerical results were in good agreement with results found in the literature (Fig. 6.3). For the corresponding system in three dimensions, we found an initial increase of the effective Young's modulus for auxetic materials under plane strain conditions (Fig. 6.5). For systems that contain cracks, our proposed approach simplifies the analytical calculations tremendously. The two-dimensional treatment predicts a simple exponential decay of the elastic modulus as a function of the crack density and exhibits the inability of the differential homogenization method to predict percolation. The simple conversion of the results for two dimensions into the three-dimensional representation prove to be equivalent to previous results from the literature, where the stiffness increase for materials with negative Poisson ratios was also seen (Fig. 6.7).

The case of a parallel arrangement of slit-like cracks, where percolation does not occur, is not easily accessible to any of the aforementioned analytical techniques. We could show by use of thin-plate theory and scaling arguments that for this geometrical setup, the relevant effective elastic constant decays as a power-law instead of exponentially, which we could also confirm by numerical simulations (Fig. 6.10).

All results show the potential of treating cracks as a free boundary problem. The phase-field method is particularly well suited for such a task if one pays attention to the effects that appear due to the introduction of the phase-field interface width as an additional length scale into the problem. By using phase-field models that have a well-defined sharp interface limit, we demonstrated for two different nonequilibrium transport processes that handling the finite-size effects and precise quantitative analysis is possible in a systematic and controlled way.

# A. Appendix

## A.1. Derivation of the Sharp Interface Equations

Here, we explain in detail how to derive in a unique way from variational principles the equations of motion, the appropriate boundary conditions and the chemical potential, which is responsible for interface motion. We assume that the two phases are coherent, i.e. the displacement field is continuous across the interface, and the mass densities are equal in both phases. Since we do not consider lattice strains or surface tension here, all elastic stresses stem from external forces and contributions due to surface energy do not couple to the elastic fields. Ultimately, they give only an additive curvature-dependent term to the chemical potential, as incorporated in Eq. (5.3). For simplicity, we assume a two-dimensional plane-strain situation.

The kinetic energy density is in both phases

$$T = \frac{1}{2} \rho \dot{u}_i^2, \quad (\text{A.1})$$

and the potential energy density reads

$$U^{(\alpha)} = \frac{1}{2} \sigma_{ik}^{(\alpha)} \epsilon_{ik}^{(\alpha)}. \quad (\text{A.2})$$

We would like to point out that certain components of the stress and strain tensors can in general be discontinuous at the interface, as will be explained below.

We assume the total volume  $V$  of the entire system to be constant in time and to be decomposed into two subvolumes  $V^{(1)}(t)$  and  $V^{(2)}(t)$  of different solids. Upper indices discriminate between the phases (see Fig. 5.1). The common interface  $A(t) := \partial V^{(1)}(t) \cap \partial V^{(2)}(t)$  with normal  $n$  and tangential  $\tau$  is moving in time due to phase transitions, and consequently, the phase volumes are time-dependent as well. However, we do not yet specify a concrete dynamical process here.

The Lagrangian is defined as

$$L(t) = \int_V T dV - \int_{V_1(t)} U^{(1)} dV - \int_{V_2(t)} U^{(2)} dV, \quad (\text{A.3})$$

and the action is

$$S = \int_{t_0}^{t_1} L(t) dt, \quad (\text{A.4})$$

with arbitrary beginning and end times  $t_0$  and  $t_1$ .

We obtain the usual elastic equations by varying the action (A.4) with respect to the displacement field for fixed interface positions. In contrast, in the next section, we will

## A.1. DERIVATION OF THE SHARP INTERFACE EQUATIONS

---

obtain the chemical potential and the equation of motion for the phase transition by variation of the interface profile for fixed elastic fields. Thus we get

$$\begin{aligned}
\delta S &= \int_{t_0}^{t_1} dt \left[ \int_V \rho \dot{u}_i \delta \dot{u}_i dV - \int_{V_1(t)} \sigma_{ik}^{(1)} \delta \epsilon_{ik}^{(1)} dV \right. \\
&\quad \left. - \int_{V_2(t)} \sigma_{ik}^{(2)} \delta \epsilon_{ik}^{(2)} dV \right] \\
&= \int_{t_0}^{t_1} dt \left[ \int_V \rho \dot{u}_i \delta \dot{u}_i dV + \int_{V_1(t)} \frac{\partial \sigma_{ik}^{(1)}}{\partial x_k} \delta u_i dV \right. \\
&\quad - \int_{A(t)} \sigma_{in}^{(1)} \delta u_i d\tau + \int_{V_2(t)} \frac{\partial \sigma_{ik}^{(2)}}{\partial x_k} \delta u_i dV \\
&\quad \left. - \int_{A(t)} \sigma_{in}^{(2)} \delta u_i d\tau \right].
\end{aligned}$$

The first integral is integrated by parts, assuming as usual that the variations  $\delta u_i$  vanish for  $t_0$  and  $t_1$ . Since also the normal vectors of both phases are antiparallel,  $\mathbf{n} := \mathbf{n}^{(1)} = -\mathbf{n}^{(2)}$ , thus  $\sigma_{in}^{(2)} = -\sigma_{in}^{(1)}$ , we get

$$\begin{aligned}
\delta S &= \int_{t_0}^{t_1} dt \left[ \int_{V_1(t)} \left( \frac{\partial \sigma_{ik}^{(1)}}{\partial x_k} - \rho \ddot{u}_i \right) \delta u_i dV \right. \\
&\quad + \int_{V_2(t)} \left( \frac{\partial \sigma_{ik}^{(2)}}{\partial x_k} - \rho \ddot{u}_i \right) \delta u_i dV \\
&\quad \left. - \int_{A(t)} (\sigma_{in}^{(1)} - \sigma_{in}^{(2)}) \delta u_i d\tau \right].
\end{aligned}$$

Demanding vanishing variation  $\delta S$  gives in the bulk the usual equations of motion

$$\frac{\partial \sigma_{ik}^{(\alpha)}}{\partial x_k} = \rho \ddot{u}_i, \tag{A.5}$$

and on the interface we obtain the continuity of normal and shear stresses

$$\sigma_{in}^{(1)} = \sigma_{in}^{(2)}. \tag{A.6}$$

The next step is to calculate the change of the total energy when the interface moves in the course of time. This is done in three steps: First, we calculate the change of energy due to the time evolution of the elastic fields for fixed interface position. Second,

we calculate the change of elastic energy due to the motion of the interface for fixed elastic fields in the bulk phases. After this second step, the coherency condition at the interface is violated. In the last step, we therefore have to do additional work to adjust the displacements appropriately.

The first contribution is

$$\begin{aligned}
 \frac{dW_1}{dt} &= \int_{V^{(1)}(t)} \frac{\partial}{\partial t} (T + U^{(1)}) dV \\
 &+ \int_{V^{(2)}(t)} \frac{\partial}{\partial t} (T + U^{(2)}) dV \\
 &= \int_V \rho \dot{u}_i \ddot{u}_i dV + \int_{V^{(1)}(t)} \sigma_{ik}^{(1)} \dot{\epsilon}_{ik}^{(1)} dV \\
 &+ \int_{V^{(2)}(t)} \sigma_{ik}^{(2)} \dot{\epsilon}_{ik}^{(2)} dV.
 \end{aligned}$$

We note that the kinetic energy density is continuous across the interface. Furthermore, by the equations of motion (A.5)

$$\begin{aligned}
 \frac{dW_1}{dt} &= \int_{V^{(1)}(t)} \dot{u}_i \frac{\partial \sigma_{ik}^{(1)}}{\partial x_k} dV + \int_{V^{(2)}(t)} \dot{u}_i \frac{\partial \sigma_{ik}^{(2)}}{\partial x_k} dV \\
 &+ \int_{V^{(1)}(t)} \frac{\partial}{\partial x_k} (\sigma_{ik}^{(1)} \dot{u}_i) dV - \int_{V^{(1)}(t)} \frac{\partial \sigma_{ik}^{(1)}}{\partial x_k} \dot{u}_i dV \\
 &+ \int_{V^{(2)}(t)} \frac{\partial}{\partial x_k} (\sigma_{ik}^{(2)} \dot{u}_i) dV - \int_{V^{(2)}(t)} \frac{\partial \sigma_{ik}^{(2)}}{\partial x_k} \dot{u}_i dV \\
 &= \int_{A(t)} \sigma_{in}^{(1)} \dot{u}_i d\tau + \int_{A(t)} \sigma_{in}^{(2)} \dot{u}_i d\tau = 0,
 \end{aligned}$$

where we assumed for simplicity that  $\dot{u}_i = 0$  on all boundaries apart from  $A(t)$ , i. e. no external work is exerted to the solids. In the last step, we used the boundary conditions (A.6),  $\sigma_{in}^{(1)} = \sigma_{in}^{(2)} = -\sigma_{in}^{(2)}$ ; also, by definition, the displacement rate  $\dot{u}_i$  is continuous across the interface. The above result is quite clear since the elastodynamic time evolution is purely conservative.

The second contribution arises due to the motion of the interface for fixed elastic fields. We extend the elastic state of the growing phase analytically into the newly acquired region. This assures that the bulk equations remain fulfilled in both phases even after the forward motion of the interface. Thus this contribution to the energy change rate reads

$$\frac{dW_2}{dt} = \int_{A(t)} v_n (U^{(1)} - U^{(2)}) d\tau. \tag{A.7}$$

## A.1. DERIVATION OF THE SHARP INTERFACE EQUATIONS

---

The interface normal velocity is positive if the phase 1 locally extends. Here, we immediately used the continuity of the kinetic energy density, which therefore cancels.

After the phase transformation in this second step, the displacements are no longer continuous at the interface. Thus extra work has to be invested to remove this misfit. In the local coordinate system  $n$  and  $\tau$  (see Fig. 5.1) the strain tensor becomes

$$\epsilon_{nn} = \partial_n u_n, \quad (\text{A.8})$$

$$\epsilon_{\tau\tau} = \partial_\tau u_\tau + \kappa u_n, \quad (\text{A.9})$$

$$\epsilon_{n\tau} = \epsilon_{\tau n} = \frac{1}{2} (\partial_\tau u_n + \partial_n u_\tau - \kappa u_\tau). \quad (\text{A.10})$$

Here,  $\kappa$  is the interface curvature, which is positive if the phase 1 is convex.

At this point, a few comments concerning the continuity of various fields across the coherent interface are in order. Since the displacement field has to be continuous across the interface, also its tangential derivatives are continuous, but the normal derivatives are not. Consequently, the following quantities are continuous:  $\partial_\tau u_\tau, \partial_\tau u_n, \kappa u_n, \kappa u_\tau, \epsilon_{\tau\tau}$ . On the other hand,  $\partial_n u_n, \partial_n u_\tau, \epsilon_{nn}, \epsilon_{n\tau}$  are discontinuous across the interface.

In the second step of energy calculation, we extended smoothly the fields into the receding domain. The interface at this new time  $t + \Delta t$  is now located at a different position. This leads to discontinuities of the displacements, e. g. for the normal component at the new position of the interface

$$\Delta u_n = \left( [\partial_n u_n]^{(1)} - [\partial_n u_n]^{(2)} \right) v_n \Delta t = (\epsilon_{nn}^{(1)} - \epsilon_{nn}^{(2)}) v_n \Delta t,$$

where  $[\dots]^{(\alpha)}$  denotes the evaluation of a probably discontinuous expression at the previous interface position, taken for the phase  $\alpha$ . Similarly, for the tangential component

$$\begin{aligned} \Delta u_\tau &= (2\epsilon_{n\tau}^{(1)} - [\partial_\tau u_n]^{(1)} + [\kappa u_\tau]^{(1)} - 2\epsilon_{n\tau}^{(2)} + [\partial_\tau u_n]^{(2)} \\ &\quad - [\kappa u_\tau]^{(2)}) v_n \Delta t \\ &= 2(\epsilon_{n\tau}^{(1)} - \epsilon_{n\tau}^{(2)}) v_n \Delta t. \end{aligned}$$

To zeroth order in  $\Delta t$ , the stresses at the new interface position are equal on both sides and identical to the stresses at the previous interface position. To reconnect the displacements, we have to apply the coherency work rate

$$\frac{dW_3}{dt} = \int_{A(t)} v_n \left[ -(\epsilon_{nn}^{(1)} - \epsilon_{nn}^{(2)}) \sigma_{nn} - 2(\epsilon_{n\tau}^{(1)} - \epsilon_{n\tau}^{(2)}) \sigma_{n\tau} \right] d\tau.$$

Altogether, the change of the energy is given by

$$\begin{aligned} \frac{dW}{dt} &= \frac{d(W_1 + W_2 + W_3)}{dt} \\ &= \int_{A(t)} v_n \left[ \left( \frac{1}{2} \sigma_{\tau\tau}^{(1)} \epsilon_{\tau\tau}^{(1)} - \frac{1}{2} \sigma_{nn}^{(1)} \epsilon_{nn}^{(1)} - \sigma_{n\tau}^{(1)} \epsilon_{n\tau}^{(1)} \right) \right. \\ &\quad \left. - \left( \frac{1}{2} \sigma_{\tau\tau}^{(2)} \epsilon_{\tau\tau}^{(2)} - \frac{1}{2} \sigma_{nn}^{(2)} \epsilon_{nn}^{(2)} - \sigma_{n\tau}^{(2)} \epsilon_{n\tau}^{(2)} \right) \right] d\tau. \end{aligned}$$

We can therefore define an appropriate chemical potential for each phase at the coherent interface

$$\mu_{el}^{(\alpha)} = \Omega \left( \frac{1}{2} \sigma_{\tau\tau}^{(\alpha)} \epsilon_{\tau\tau}^{(\alpha)} - \frac{1}{2} \sigma_{nn}^{(\alpha)} \epsilon_{nn}^{(\alpha)} - \sigma_{n\tau}^{(\alpha)} \epsilon_{n\tau}^{(\alpha)} \right). \quad (\text{A.11})$$

Notice that, in contrast to a free surface, the normal and shear contributions appear with negative sign. Then, the energy dissipation rate can be written as

$$\frac{dW}{dt} = \frac{1}{\Omega} \int_{A(t)} (\mu_{el}^{(1)} - \mu_{el}^{(2)}) v_n d\tau. \quad (\text{A.12})$$

Due to the coherency condition and the requirement of equal mass density, the kinetic energy density does not appear.

## A.2. Matching Conditions

We assume to have solved the outer equations with a solution  $\tilde{\psi}(x, z, t) = \psi(r, s, t)$  that is some arbitrary (sufficiently often differentiable) function of space and time. The corresponding inner solution is defined to be  $\Psi(\rho, s, t)$ . Since the following relations are independent of  $s$  and  $t$ , we refrain from carrying them along in our notation.

The inner and outer solutions must satisfy the asymptotic relationship

$$\Psi(\rho) \sim \psi(r) = \psi(\xi\rho) \quad (\text{A.13})$$

in the simultaneous limits ( $\rho \rightarrow \infty$ ,  $\xi \rightarrow 0$ ,  $\xi\rho \rightarrow 0$ ). We start by expanding both functions in the interface width  $\xi$  and obtain

$$\Psi(\rho) = \Psi^{(0)}(\rho) + \xi\Psi^{(1)}(\rho) + \xi^2\Psi^{(2)}(\rho) + \dots, \quad (\text{A.14})$$

for the inner solution and

$$\begin{aligned} \psi(\xi\rho) &= \psi^{(0)}(r) + \xi\psi^{(1)}(r) + \xi^2\psi^{(2)}(r) + \dots \\ &= \psi_0(0) + \xi \left( \rho \frac{\partial\psi^{(0)}(0)}{\partial\rho} + \psi^{(1)}(0) \right) \\ &\quad + \xi^2 \left( \rho^2 \frac{1}{2} \frac{\partial^2\psi^{(0)}(0)}{\partial\rho^2} + \rho \frac{\partial\psi^{(1)}(0)}{\partial\rho} + \psi_2(0) \right) + \dots, \end{aligned} \quad (\text{A.15})$$

for the outer solution. If the derivatives are discontinuous at  $r = 0$ , the derivatives are to be taken for  $r \rightarrow +0$ . Analogous expressions with  $r \rightarrow -0$  are obtained for the asymptotics as  $\rho \rightarrow -\infty$ . Now, both functions can be compared order by order in powers of  $\xi$ , to arrive at the following asymptotic relationships

$$\lim_{\rho \rightarrow \pm\infty} \Psi^{(0)}(\rho) = \psi^{(0)}(\pm 0), \quad (\text{A.16})$$

$$\Psi^{(1)}(\rho) \sim \rho \frac{\partial\psi^{(0)}(\pm 0)}{\partial\rho} + \psi^{(1)}(\pm 0) \quad (\rho \rightarrow \pm\infty), \quad (\text{A.17})$$

$$\Psi_2(\rho) \sim \frac{1}{2} \rho^2 \frac{\partial^2\psi^{(0)}(\pm 0)}{\partial\rho^2} + \rho \frac{\partial\psi^{(1)}(\pm 0)}{\partial\rho} + \psi_2(\pm 0) \quad (\rho \rightarrow \pm\infty). \quad (\text{A.18})$$

Moreover, asymptotic relations such as (A.17) can be decomposed into statements about function limits

$$\lim_{\rho \rightarrow \pm\infty} \partial_\rho \Psi^{(1)}(\rho) = \frac{\partial \psi^{(0)}(\pm 0)}{\partial \rho}, \quad (\text{A.19})$$

$$\lim_{\rho \rightarrow \pm\infty} \left( \Psi^{(1)}(\rho) - \rho \frac{\partial \psi^{(0)}(\pm 0)}{\partial \rho} \right) = \psi^{(1)}(\pm 0). \quad (\text{A.20})$$

### A.3. Homogenization Method for One-Dimensional Springs

The problem of one-dimensional springs is special in the sense that all geometric aspects of the problem are nonexistent. Therefore, it helps to concentrate on some mathematical aspects of homogenization theory.

We pull on two connected springs  $i = 1, 2$  with initial length  $l_i$ , a spring constant  $k_i$ , strain  $\varepsilon_i$ , stress  $\sigma_i$ . The pull with an external force  $F$  results in the individual displacements  $u_i$  with total displacement  $u = u_1 + u_2$ . We are interested in the effective elastic constants for the spring system.

In the following, the effective moduli of the combined system are written without index, whereas the partial values for each phase have the corresponding indices. The macroscopic strain is given by

$$\varepsilon l = u = u_1 + u_2 = \varepsilon_1 l_1 + \varepsilon_2 l_2 \quad (\text{A.21})$$

$$\Rightarrow \varepsilon = \varepsilon_1 \frac{l_1 + \frac{\varepsilon_2}{\varepsilon_1} l_2}{l}. \quad (\text{A.22})$$

Eliminating  $l_1 = l - l_2$  and defining the concentration  $c$  as  $c = l_2/l$ , we obtain

$$\varepsilon = \varepsilon_1 \left[ 1 + \left( \frac{\varepsilon_2}{\varepsilon_1} - 1 \right) c \right]. \quad (\text{A.23})$$

The stresses should be continuous,

$$\sigma = k\varepsilon = \varepsilon_1 k_1 = \varepsilon_2 k_2 \quad \Rightarrow \quad \frac{\varepsilon_2}{\varepsilon_1} = \frac{k_1}{k_2}, \quad (\text{A.24})$$

so we can solve for the effective  $k$ :

$$k = \frac{\sigma}{\varepsilon} = \frac{k_1 k_2}{c k_1 + (1 - c) k_2}. \quad (\text{A.25})$$

This result for the effective spring constant is exact.

The low density expansion for  $k$  of a two-dimensional system containing circular or elliptical inclusions is [40]:

$$k = k_1 + \frac{\mu_1 + k_1}{\mu_1 + k_2} (k_2 - k_1) c + O(c^2). \quad (\text{A.26})$$

#### A.4. EFFECTIVE ELASTIC CONSTANTS FOR A REGULAR ARRAY OF CRACKS

The higher order terms in  $c$  contain all the elastic interactions between different inclusions and can be neglected. We are only interested in the one-dimensional case, so by setting  $\mu = 0$ , we specialize to the one-dimensional expression

$$k = k_1 + \frac{k_1}{k_2}(k_2 - k_1)c + O(c^2). \quad (\text{A.27})$$

As a first check, we also perform an expansion of Eq. (A.25) in the concentration  $c$ , which gives us immediately

$$k(c) = k_1 + \frac{k_1}{k_2}(k_2 - k_1)c + O(c^2). \quad (\text{A.28})$$

We see that the results of Eqs. (A.27) and (A.28) are identical.

Using the homogenization condition (see Eq. (6.5))

$$\frac{dk}{dc} = \frac{1}{1-c} \left. \frac{\partial F(k_1, k_2, c)}{\partial c} \right|_{\substack{c=0 \\ k_1=k}} \quad (\text{A.29})$$

and using the initial condition  $k_1 = k$ , we obtain immediately the following solution for the differential equation

$$k = \frac{k_1 k_2}{k_1 c + k_2 (1 - c)}, \quad (\text{A.30})$$

which reproduces the exact result.

### A.4. Effective Elastic Constants for a Regular Array of Cracks

In this section, we present a more detailed derivation of the asymptotic scaling behavior of a system that contains many aligned cracks. Specifically, we consider a regular arrangement of cracks, where the effective elastic constants for the crack density parameter  $\alpha$  can be calculated rigorously for  $\alpha \rightarrow \infty$ . It should be noted that in this regular arrangement, the plate length  $R$ , which is given by the overlap of the cracks, appears as an additional parameter. It is related to the gap distance  $s$  and the crack length  $L$  by  $L = 2R + s$ , and the final solution must therefore contain the dimensionless parameter  $g = s/R$ , which describes the ratio of the gaps between the cracks and their overlap. The calculation is based on the fact that the displacement applied to the sample is mainly stored in the crack opening, whereas the material between the cracks is only slightly stretched; instead, it behaves as a bent plate, which is thin in the limit of  $R \gg h$ , where  $h$  denotes the vertical distance between the horizontally aligned cracks, see Fig. A.1.

The area of the stretched material that is elastically affected by the presence of a single crack,  $N = 1$ , is given by

$$A = (L + s)h = 2(R + s)h,$$

which is illustrated as the dashed box in Fig. A.1. Subsequently, the crack density parameter

$$\alpha = \frac{\pi(L/2)^2 N}{A}$$



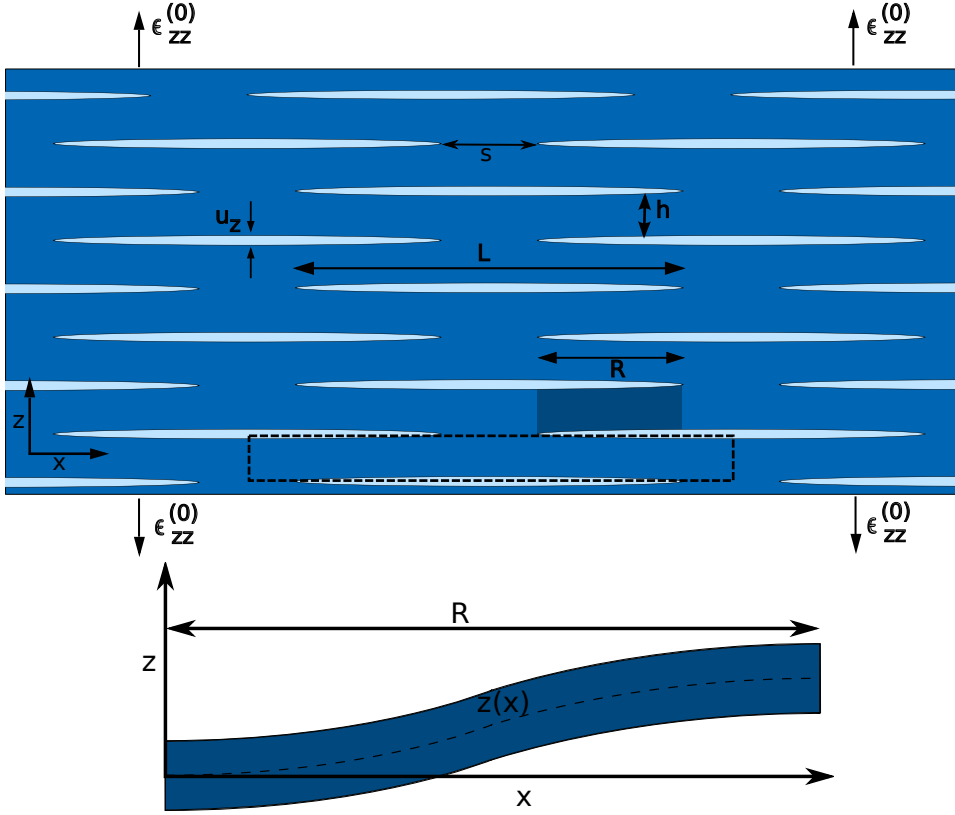


Figure A.1.: Sketch of a regular arrangement of parallel cracks which we investigate both analytically as well as numerically. The dashed rectangle shows a periodic unit cell in which the elastic problem is solved numerically. The average crack length is  $L$ , the overlap between two cracks is  $R$ , and the average vertical distance between neighboring cracks is denoted by  $h$ . The region marked by the darker box behaves like a plate that is bent under the applied load, as shown in the enlarged sketch below. The dashed line visualizes the deformation of the neutral fiber.

can be expressed as

$$\alpha = \frac{\pi}{2} \frac{(1 + g/2)^2 R}{1 + g} \frac{1}{h}.$$

Since the upper and lower surfaces of the thin bent plate are stress free, the bending leads to the condition [73]

$$\frac{\partial^4 z}{\partial x^4} = 0.$$

Since the total displacement is distributed equally among all crack openings, each plate is displaced by  $z(x) = \langle \epsilon_{zz} \rangle h$ . Together with the symmetry conditions

$$\frac{\partial z}{\partial x}(0) = \frac{\partial z}{\partial x}(R) = 0$$

and the reference value  $z(0) = 0$ , the general solution

$$z(x) = ax^3 + bx^2 + cx + d$$

has the coefficients

$$b = \frac{3\langle\epsilon_{zz}\rangle h}{R^2} \text{ and } a = \frac{-2b}{3R}.$$

The force per unit length in  $x$ -direction that is required to bend the plate by the given amount is given by

$$F = \frac{-Eh^3}{12(1-\nu^2)} \frac{\partial^4 z}{\partial x^4} = \frac{Eh^4\langle\epsilon_{zz}\rangle}{(1-\nu^2)R^3},$$

which gives us the average stress in vertical direction

$$\langle\sigma_{zz}\rangle = \frac{F}{s+R} = \frac{\langle\epsilon_{zz}\rangle}{1-\nu^2} \left(\frac{\pi}{2}\right)^4 \frac{(1+g/2)^8}{(1+g)^5} \alpha^{-4},$$

which in turn, by employing Hooke's law for the effective medium, simply gives us

$$C_{3333}^{eff} = \frac{E}{1-\nu^2} \left(\frac{\pi}{2}\right)^4 \frac{(1+g/2)^8}{(1+g)^5} \alpha^{-4}.$$

Since the bare elastic constant  $C_{3333}$  is related to the isotropic moduli by

$$C_{3333} = \frac{E(1-\nu)}{(1+\nu)(1-2\nu)},$$

we obtain

$$\frac{C_{3333}^{eff}}{C_{3333}} = \frac{1-2\nu}{(1-\nu)^2} \left(\frac{\pi}{2}\right)^4 \frac{(1+g/2)^8}{(1+g)^5} \alpha^{-4}$$

as final result for the asymptotic behavior of  $\alpha \rightarrow \infty$ .

## A.5. Numerical aspects

In this section, we explain in more detail the numerical discretization procedure which is designed to obtain a stable numerical algorithm for the elastic problem with moving boundaries. We use explicit schemes for both the phase-field and the elastic equations of motion for two reasons: the first reason is that the problem-inherent nonlinearity poses serious restrictions on the admissible timesteps even for implicit schemes, eating up most of the advantage of unconditional stability. The second reason is that a parallelization of a grid based explicit scheme is rather straightforward. The computational domain is split up among the used processors which can do most of the calculations independently. After each timestep, information about the changed boundaries needs to be exchanged. This is a one-to-one communication, which is very efficient and scales well on many processors.

The dissipative phase-field dynamics is normally rather robust. If non-obvious aspects have to be considered, they are mentioned at the appropriate locations in the main text. In contrast, more care has to be taken in the treatment of the elastic equations of motion. They conserve energy, and therefore, tiny numerical errors can easily add up, destroying

the solution. We would like to emphasize that energy conservation follows from the continuous time translation symmetry, which is violated in any numerical discretization approach. While fluctuations in energy cannot be avoided, it has to be assured that the average energy does not change in time. Therefore, naive discretization schemes can lead to long time instabilities. We can overcome this problem by using a generic time symmetric scheme that does not suffer from this problem. It is not specifically related to the phase-field description and can easily be extended to three dimensional systems or spatially varying mass densities. For the solution of elastic problems, a sufficient amount of boundary conditions have to be provided. Since they depend on the problem and are given explicitly in the main text whenever needed, we do not discuss them here and concentrate on bulk properties instead. The equation of motions can be obtained from variational principles, so the elastodynamic evolution follows from the action

$$\frac{\delta S}{\delta u_i} = 0. \quad (\text{A.31})$$

We investigate the contributions from the kinetic and the potential energy separately:

$$S_T := \int \int \frac{1}{2} \rho \dot{u}_i^2 dV dt, \quad S_U := - \int \int \frac{1}{2} \sigma_{ij} \epsilon_{ij} dV dt, \quad (\text{A.32})$$

and obtain for the potential part

$$S_U = - \frac{1}{2} \int \int [ (2\mu + \lambda)(\epsilon_{xx}^2 + \epsilon_{zz}^2) + 2\lambda \epsilon_{xx} \epsilon_{zz} + 4\mu \epsilon_{xz}^2 ] dV dt.$$

We use a staggered grid [114], i.e. the mass density and the elastic constants are defined on the grid points, displacements between them (see Fig. A.2).

In our case, the spatial (and temporal) values of the elastic coefficients  $\mu, \lambda$  are related to the phase-field. Similar to the derivation above, we keep the phase-field fixed (and thus the elastic coefficients) during the variation with respect to the elastic displacements. We use the notation  $u_k^{(n)}(i, j)$ , where  $i, j$  are the spatial and  $n$  is the time index; in the phase-field formulation, no explicit distinction between the different phases has to be made, and therefore the upper index cannot be confused with previous notations. We assume the grid spacing  $\Delta x$  to be the same in both spatial directions.

The central idea for derivation of the discrete equations of motion is the discretization of the action (obeying symmetry in space and time) and to perform discrete variations with respect to each degree of freedom  $u_x^{(n)}(i, j)$  and  $u_z^{(n)}(i, j)$ . We study the potential contribution to  $S$  first:

$$S_U \rightarrow - \frac{1}{2} (\Delta x)^2 \Delta t \sum_n \sum_{i,j} \left[ \underbrace{(2\mu + \lambda)(\epsilon_{xx}^2 + \epsilon_{zz}^2) + 2\lambda \epsilon_{xx} \epsilon_{zz}}_{\text{on grid points}} + \underbrace{4\mu \epsilon_{xz}^2}_{\text{in square center}} \right].$$

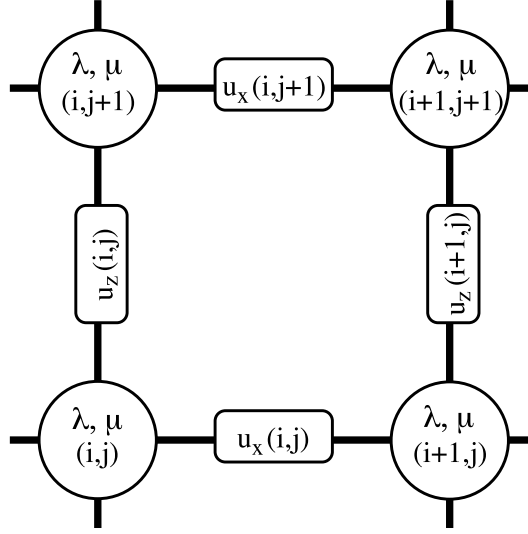


Figure A.2.: The staggered grid: Shear modulus  $\mu$  and Lamé coefficient  $\lambda$  are defined on the nodes (circles), the displacements  $u_i$  on the connecting lines. Thus we have three different lattices which are shifted by  $\Delta x/2$ .

We express the first part on the grid points, and therefore replace the elastic coefficients as follows:

$$\mu \rightarrow \mu(i, j), \quad \lambda \rightarrow \lambda(i, j). \quad (\text{A.33})$$

Strains also have to be evaluated on the nodal points:

$$\epsilon_{xx} \rightarrow \epsilon_{xx}^{(n)}(i, j) = \frac{u_x^{(n)}(i, j) - u_x^{(n)}(i-1, j)}{\Delta x}, \quad (\text{A.34})$$

$$\epsilon_{zz} \rightarrow \epsilon_{zz}^{(n)}(i, j) = \frac{u_z^{(n)}(i, j) - u_z^{(n)}(i, j-1)}{\Delta x}. \quad (\text{A.35})$$

The second part is expressed in the center of the squares, i. e.:

$$\begin{aligned} \mu &\rightarrow \mu(i+1/2, j+1/2) \\ &= \frac{1}{4} (\mu(i, j) + \mu(i+1, j) + \mu(i, j+1) + \mu(i+1, j+1)), \\ \epsilon_{xz} &\rightarrow \epsilon_{xz}^{(n)}(i+1/2, j+1/2) \\ &= \left[ u_x^{(n)}(i, j+1) - u_x^{(n)}(i, j) + u_z^{(n)}(i+1, j) \right. \\ &\quad \left. - u_z^{(n)}(i, j) \right] / (2\Delta x). \end{aligned}$$

We illustrate the discrete variation with respect to  $u_x^{(n)}(i, j)$ ,

$$\begin{aligned} \frac{\partial S_U}{\partial u_x^{(n)}(i, j)} = & -\Delta t \Delta x \left\{ [2\mu(i, j) + \lambda(i, j)] \epsilon_{xx}^{(n)}(i, j) \right. \\ & - [2\mu(i+1, j) + \lambda(i+1, j)] \epsilon_{xx}^{(n)}(i+1, j) \\ & + \lambda(i, j) \epsilon_{zz}^{(n)}(i, j) - \lambda(i+1, j) \epsilon_{zz}^{(n)}(i+1, j) \\ & - 2\mu(i+1/2, j+1/2) \epsilon_{xz}^{(n)}(i+1/2, j+1/2) \\ & \left. + 2\mu(i+1/2, j-1/2) \epsilon_{xz}^{(n)}(i+1/2, j-1/2) \right\}. \end{aligned}$$

For the kinetic contribution, we proceed in a similar way. Here, the terms are defined between the lattice points:

$$S_T \rightarrow \frac{1}{2} (\Delta x)^2 \Delta t \sum_n \sum_{i, j} \underbrace{\rho \dot{u}_x^2}_{\text{at } u_x} + \underbrace{\rho \dot{u}_z^2}_{\text{at } u_z}. \quad (\text{A.36})$$

Discretization of the first term defines the displacement rate  $v_x^{(n+1/2)}(i, j)$  at intermediate timesteps

$$\dot{u}_x \rightarrow v_x^{(n+1/2)}(i, j) := \frac{u_x^{(n+1)}(i, j) - u_x^{(n)}(i, j)}{\Delta t}, \quad (\text{A.37})$$

and similarly for the second term

$$\dot{u}_z \rightarrow v_z^{(n+1/2)}(i, j) := \frac{u_z^{(n+1)}(i, j) - u_z^{(n)}(i, j)}{\Delta t}. \quad (\text{A.38})$$

Variation of the kinetic contribution to the discrete action therefore gives

$$\begin{aligned} \frac{\partial S_T}{\partial u_x^{(n)}(i, j)} = & -(\Delta x)^2 \rho \left[ v_x^{(n+1/2)}(i, j) - v_x^{(n-1/2)}(i, j) \right] \\ = & -(\Delta x)^2 \rho \Delta t \frac{u_x^{(n+1)}(i, j) - 2u_x^{(n)}(i, j) + u_x^{(n-1)}(i, j)}{(\Delta t)^2}. \end{aligned}$$

Notice that this expression is invariant against time inversion. Vanishing total variation of  $S = S_U + S_T$  with respect to  $u_x^{(n)}(i, j)$  leads to the desired explicit evolution equation. The same procedure has to be performed for  $u_z$ .

# Bibliography

- [1] T. Abel, E. Brener, and H. Müller-Krumbhaar. Three-dimensional growth morphologies in diffusion-controlled channel growth. *Phys. Rev. E*, 55(6):7789–7792, Jun 1997.
- [2] I. S. Aranson, V. A. Kalatsky, and V. M. Vinokur. Continuum Field Description of Crack Propagation. *Phys. Rev. Lett.*, 85:118–121, 2000.
- [3] R. J. Asaro and W. A. Tiller. Interface Morphology Development During Stress Corrosion Cracking: Part I. Via Surface Diffusion. *Metal. Trans.*, 3:1789–1796, 1972.
- [4] I. Balberg. Universal percolation-threshold limits in the continuum. *Phys. Rev. B*, 31:4053–4055, Mar 1985.
- [5] I. Balberg, C. H. Anderson, S. Alexander, and N. Wagner. Excluded volume and its relation to the onset of percolation. *Phys. Rev. B*, 30:3933–3943, Oct 1984.
- [6] I. Balberg and N. Binenbaum. Computer study of the percolation threshold in a two-dimensional anisotropic system of conducting sticks. *Phys. Rev. B*, 28:3799–3812, Oct 1983.
- [7] P. Berger, P. Kohlert, K. Kassner, and C. Misbah. Pattern selection in biaxially stressed solids. *Phys. Rev. Lett.*, 90(17):176103, 2003.
- [8] J. Berréhar, C. Caroli, C. Lapersonne-Meyer, and M. Schott. Surface patterns on single-crystal films under uniaxial stress: Experimental evidence for the grinfeld instability. *Phys. Rev. B*, 46(20):13487–13495, 1992.
- [9] M. Bertalmío, L.-T. Cheng, S. Osher, and G. Sapiro. Variational problems and partial differential equations on implicit surfaces. *J. Comput. Phys.*, 174(2):759–780, 2001.
- [10] D. N. Bhate, A. F. Bower, and A. Kumar. A phase field model for failure in interconnect lines due to coupled diffusion mechanisms. *J. Mech. Phys. Solids*, 50(10), 2002.
- [11] D. N. Bhate, A. Kumar, and A. F. Bower. Diffuse interface model for electromigration and stress voiding. *J. Appl. Phys.*, 87:1712–1721, Feb 2000.
- [12] E. Bouchbinder, A. Pomyalov, and I. Procaccia. Dissipative Viscoplastic Deformation in Dynamic Fracture: Tip Blunting and Velocity Selection. *Phys. Rev. Lett.*, 97(13):134301, Sep 2006.

- [13] S. Boucher. On the Effective Moduli of Isotropic Two-Phase Elastic Composites. *Journal of Composite Materials*, 8(1):82–89, 1974.
- [14] E. A. Brener, V. I. Marchenko, and R. Spatschek. Influence of strain on the kinetics of phase transitions in solids. *Phys. Rev. E*, 75(4):041604, Apr 2007.
- [15] E. A. Brener, H. Müller-Krumbhaar, and R. Spatschek. Coarsening of Cracks in a Uniaxially Strained Solid. *Phys. Rev. Lett.*, 86:1291–1294, 2001.
- [16] E. A. Brener and R. Spatschek. Fast crack propagation by surface diffusion. *Phys. Rev. E*, 67(1):016112, 2003.
- [17] David Broek. *The Practical Use of Fracture Mechanics*. Springer, 2nd edition edition, Oct 1988.
- [18] D. A. G. Bruggeman. Berechnung verschiedener physikalischer Konstanten von heterogenen Substanzen: I. *Ann. der Physik*, 22:636, 1935.
- [19] B. Budiansky and R. O’Connell. Elastic moduli of a cracked solid. *Int. J. Solids Structures*, 12(2), 1976.
- [20] A. L. R. Bug, S. A. Safran, G. S. Grest, and I. Webman. Do interactions raise or lower a percolation threshold? *Phys. Rev. Lett.*, 55(18):1896–1899, Oct 1985.
- [21] M. Burger, F. Hauber, C. Stöcker, and A. Voigt. A level set approach to anisotropic flows with curvature regularization. *J. Comput. Phys.*, 225:183–205, Jul 2007.
- [22] G. Caginalp. Conserved-phase field system: Implications for kinetic undercooling. *Phys. Rev. B*, 38:789–791, Jul 1988.
- [23] G. Caginalp and X. Chen. Convergence of the phase field model to its sharp interface limits. *European Journal of Applied Mathematics*, 9:417–445, 1998.
- [24] G. Caginalp and P. Fife. Phase-field methods for interfacial boundaries. *Phys. Rev. B*, 33:7792–7794, Jun 1986.
- [25] J. W. Cahn, C. M. Elliott, and A. Novick-Cohen. The cahn-hilliard equation with a concentration dependent mobility: motion by minus the laplacian of the mean curvature. *Euro. J. Appl. Math*, 7:287, 1996.
- [26] M. P. Cleary, S. Lee, and I. Chen. Self-consistent techniques for heterogeneous media. *J. Engrn. Mech. Div. ASCE*, 106(5):861–887, 1980.
- [27] A. R. Day, K. A. Snyder, E. J. Garboczi, and M. F. Thorpe. The elastic moduli of a sheet containing circular holes. *J. Mech. Phys. Solids*, 40(5):1031–1051, 1992.
- [28] J. E. Jr. Dennis and R. B. Schnabel. *Numerical Methods for Unconstrained Optimization and Nonlinear Equations*. Number 16 in Classics in Applied Mathematics. Soc for Industrial & Applied Math, 1996.

- 
- [29] S.-J. Doong and R. T. Yang. *Bulk separation of multicomponent gas mixtures by pressure swing adsorption: Pore/surface diffusion and equilibrium models*, volume 32. AIChE Journal, 1986.
- [30] L. O. Eastgate, J. P. Sethna, M. Rauscher, T. Cretegny, C.-S. Chen, and C. R. Myers. Fracture in mode I using a conserved phase-field model. *Phys. Rev. E*, 65(3):036117, Mar 2002.
- [31] K. R. Elder, M. Grant, N. Provatas, and J. M. Kosterlitz. Sharp interface limits of phase-field models. *Phys. Rev. E*, 64(2):021604, Jul 2001.
- [32] J. D. Eshelby. The Determination of the Elastic Field of an Ellipsoidal Inclusion, and Related Problems. *Proceedings of the Royal Society of London. Series A, Mathematical and Physical Sciences (1934-1990)*, 241(1226):376–396, 1957.
- [33] M. L. Falk and J. S. Langer. Dynamics of viscoplastic deformation in amorphous solids. *Phys. Rev. E*, 57:7192–7205, JunJul 1998.
- [34] S. Feng, M. F. Thorpe, and E. J. Garboczi. Effective-medium theory of percolation on central-force elastic networks. *Phys. Rev. B*, 31(1):276–280, Jan 1985.
- [35] F. H. Fenton, E. M. Cherry, A. Karma, and W.-J. Rappel. Modeling wave propagation in realistic heart geometries using the phase-field method. *Chaos: An Interdisciplinary Journal of Nonlinear Science*, 15(1):013502–11, 2005.
- [36] J. Fineberg and M. Marder. Instability in dynamic fracture. *Phys. Rep.*, 313:1–2, 1999.
- [37] L. B. Freund. *Dynamic Fracture Mechanics*. Cambridge Monographs on Mechanics and Applied Mathematics. Cambridge University Press, first edition edition, 1998.
- [38] H. Garcke, B. Nestler, and B. Stoth. A multiphase field concept: numerical simulations of moving phase boundaries and multiple junctions. *SIAM J. Appl. Math.*, 60(1):295–315, 1999.
- [39] S. Giordano. Differential schemes for the elastic characterisation of dispersions of randomly oriented ellipsoids. *Eur. J. Mech. A Solids*, 22(6):885–902, 2003.
- [40] S. Giordano. Relation Between Microscopic and Macroscopic Mechanical Properties in Random Mixtures of Elastic Media. *J. Engin. Mat. Tech.*, Proof Copy, Apr 2007.
- [41] S. Giordano and L. Colombo. Effects of the Orientational Distribution of Cracks in Solids. *Phys. Rev. Lett.*, 98(5):055503, Feb 2007.
- [42] A. A. Griffith. The phenomena of rupture and flow in solids. *Phil. Trans. A.*, 221(163), 1921.
- [43] M. A. Grinfeld. Instability of the separation boundary between a nonhydrostatically stressed elastic body and a melt. *Sov. Phys. Dok.*, 31:831, Oct 1986.



- [44] C. Gugenberger, R. Spatschek, and K. Kassner. Comparison of phase-field models for surface diffusion. *Phys. Rev. E*, 78(1):016703, 2008.
- [45] M. Haataja, J. Müller, A. D. Rutenberg, and M. Grant. Dislocations and morphological instabilities: Continuum modeling of misfitting heteroepitaxial films. *Phys. Rev. B*, 65(16):165414, Apr 2002.
- [46] M. Hartmann. *Phasenfeld-Untersuchungen zur Hydrodynamik partieller Benetzung*. PhD thesis, RWTH Aachen, 2003.
- [47] Z. Hashin. The differential scheme and its application to cracked materials. *J. Mech. Phys. Solids*, 36:719–734, 1988.
- [48] Z. Hashin and S. Shtrikman. A variational approach to the theory of the elastic behaviour of polycrystals. *J. Mech. Phys. Solids*, 10(4):343–352, 1962.
- [49] Z. Hashin and S. Shtrikman. A variational approach to the theory of the elastic behaviour of multiphase materials. *J. Mech. Phys. Solids*, 11(2):127–140, 1963.
- [50] J. A. Hauch, D. Holland, M. P. Marder, and H. L. Swinney. Dynamic Fracture in Single Crystal Silicon. *Phys. Rev. Lett.*, 82:3823–3826, 1999.
- [51] F. Hecht and O. Pironneau. *FreeFem++*. Universite Pierre et Marie Curie, 2007. <http://www.freefem.org/ff++/ftp/freefem++doc.pdf>.
- [52] H. Henry and H. Levine. Dynamic Instabilities of Fracture under Biaxial Strain Using a Phase Field Model. *Phys. Rev. Lett.*, 93(10):105504, Sep 2004.
- [53] C. Herring. Surface tension as a motivation for sintering. In W. E. Kingston, editor, *Physics of Powder Metallurgy*. McGraw-Hill Book Company, Inc., 1951.
- [54] J. A. Hodgdon and J. P. Sethna. Derivation of a general three-dimensional crack-propagation law: A generalization of the principle of local symmetry. *Phys. Rev. B*, 47(9):4831–4840, Mar 1993.
- [55] P. C. Hohenberg and B. I. Halperin. Theory of dynamic critical phenomena. *Rev. Mod. Phys.*, 49:435–479, 1977.
- [56] H. Horii and S. Nemat-Nasser. Overall moduli of solids with microcracks: Load-induced anisotropy. *J. Mech. Phys. Solids*, 31(2):155–171, 1983.
- [57] D. Hull and D. E. Rimmer. The growth of grain-boundary voids under stress. *Philosophical Magazine*, 4(42):673–687, 1959.
- [58] G. R. Irwin. *Fracture mechanics*. Structural Mechanics. Pergamon Press, Elmsford, 1960.
- [59] M. Kachanov and I. Sevostianov. On quantitative characterization of microstructures and effective properties. *Int. J. Solids Structures*, 42(2):309–336, 2005.

- 
- [60] M. Kachanov, I. Tsukrov, and B. Shafiro. Effective moduli of solids with cavities of various shapes. *Appl. Mech. Rev.*, 47(1):151–174, Jan 1994.
- [61] M. F. Kanninen and C. H. Popelar. *Advanced fracture mechanics*. Oxford University Pr., New-York, NY, 1985.
- [62] A. Karma, D. A. Kessler, and H. Levine. Phase-Field Model of Mode III Dynamic Fracture. *Phys. Rev. Lett.*, 87(4):045501, 2001.
- [63] A. Karma and A. E. Lobkovsky. Unsteady Crack Motion and Branching in a Phase-Field Model of Brittle Fracture. *Phys. Rev. Lett.*, 92(24):245510, 2004.
- [64] A. Karma and W.-J. Rappel. Phase-field method for computationally efficient modeling of solidification with arbitrary interface kinetics. *Phys. Rev. E*, 53:3017, Apr 1996.
- [65] A. Karma and W.-J. Rappel. Quantitative phase-field modeling of dendritic growth in two and three dimensions. *Phys. Rev. E*, 57(4):4323–4349, Apr 1998.
- [66] K. Kassner. How to model surface diffusion using the phase-field approach. cond-mat/0607823, Jul 2006.
- [67] K. Kassner and C. Misbah. Non-Linear Evolution of a Uniaxially Stressed Solid: A Route to Fracture? *Europhys. Lett.*, 28:245–250, Nov 1994.
- [68] K. Kassner and C. Misbah. A phase-field approach for stress-induced instabilities. *Europhys. Lett.*, 46:217–223, Apr 1999.
- [69] K. Kassner, C. Misbah, J. Müller, J. Kappey, and P. Kohlert. Phase-field modeling of stress-induced instabilities. *Phys. Rev. E*, 63(3):036117, 2001.
- [70] R. Kobayashi. Modeling and numerical simulations of dendritic crystal growth. *Phys. D*, 63(3-4):410–423, 1993.
- [71] R. Kobayashi. A numerical approach to three-dimensional dendritic solidification. *Exp. Math.*, 3(1):60, 1994.
- [72] R. Lakes. Foam structures with a negative poisson’s ratio. *Science*, 235(4792):1038–1040, 1987.
- [73] L. D. Landau and E. M. Lifshitz. *Theory of Elasticity*. Pergamon Press, Oxford, 1987.
- [74] J. S. Langer and R. F. Sekerka. Theory of departure from local equilibrium at the interface of a two-phase diffusion couple. *Acta. Metall.*, 23(10):1225–1237, Oct 1975.
- [75] A. Livne, O. Ben-David, and J. Fineberg. Oscillations in rapid fracture. *Phys. Rev. Lett.*, 98(12):124301, 2007.
- [76] A. Livne, G. Cohen, and J. Fineberg. Universality and hysteretic dynamics in rapid fracture. *Phys. Rev. Lett.*, 94(22):224301, 2005.

- [77] M. Mahadevan and R. M. Bradley. Phase field model of surface electromigration in single crystal metal thin films. *Phys. D*, 126:201–213, Feb 1999.
- [78] G. B. McFadden, A. A. Wheeler, R. J. Braun, S. R. Coriell, and R. F. Sekerka. Phase-field models for anisotropic interfaces. *Phys. Rev. E*, 48(3):2016–2024, Sep 1993.
- [79] R. McLaughlin. A study of the differential scheme for composite materials. *Int. J. Engng Sci.*, 15(4):237–244, 1977.
- [80] T. Mukerji, J. Berryman, G. Mavko, and P. Berge. Differential effective medium modeling of rock elastic moduli with critical porosity constraints. *Geophys. Res. Lett.*, 22:555–558, Mar 1995.
- [81] J. Müller and M. Grant. Model of surface instabilities induced by stress. *Phys. Rev. Lett.*, 82(8):1736–1739, 1999.
- [82] H. Müller-Krumbhaar, T. Abel, E. A. Brener, M. Hartmann, N. Eissfeldt, and D. Temkin. Growth-morphologies in solidification and hydrodynamics. *JSME International Journal Series B Fluids and Thermal Engineering*, 45(1):129–132, 2002.
- [83] W. W. Mullins. Theory of thermal grooving. *Journal of Applied Physics*, 28(3):333–339, 1957.
- [84] W. W. Mullins. Flattening of a nearly plane solid surface due to capillarity. *Journal of Applied Physics*, 30(1):77–83, 1959.
- [85] T. Mura. *Micromechanics of Defects in Solids*. Mechanics of Elastic and Inelastic Solids. Springer, 2nd edition edition, 1990.
- [86] S. Nemat-Nasser and M. Hori. *Micromechanics: Overall Properties of Heterogeneous Materials*. Elsevier Science Publishers B. V., 2nd edition edition, 1999.
- [87] A. N. Norris. A differential scheme for the effective moduli of composites. *Mechanics of Materials*, 4:1–16, 1985.
- [88] E. Orowan. Energy criteria of fracture. *Weld. Res. Supp.*, 34:157–160, 1955.
- [89] S. Osher and J. A. Sethian. Fronts propagating with curvature-dependent speed: Algorithms based on hamilton-jacobi formulations. *Journal of Computational Physics*, 79(1):12–49, 1988.
- [90] F. Otto, P. Penzler, A. Rätz, T. Rump, and A. Voigt. A diffuse-interface approximation for step flow in epitaxial growth. *Nonlinearity*, 17:477–491, Mar 2004.
- [91] O. Penrose and P. C. Fife. Thermodynamically consistent models of phase-field type for the kinetic of phase transitions. *Physica D Nonlinear Phenomena*, 43:44–62, 1990.

- 
- [92] O. Penrose and P. C. Fife. On the relation between the standard phase-field model and a “thermodynamically consistent” phase-field model. *Physica D Nonlinear Phenomena*, 69:107–113, Nov 1993.
- [93] D. C. Pham. Differential nonhomogeneous models for elastic randomly cracked solids. *International Journal of Solids and Structures*, 37(52):7759–7768, 2000.
- [94] O. Pierre-Louis. Phase field models for step flow. *Phys. Rev. E*, 68(2):021604, Aug. 2003.
- [95] G. E. Pike and C. H. Seager. Percolation and conductivity: A computer study. I. *Phys. Rev. B*, 10:1421–1434, Aug. 1974.
- [96] D. Pilipenko, R. Spatschek, E. Brener, and C. Müller-Gugenberger. Continuum theory of fracture. *ndt.net*, 11, Dec 2006.
- [97] D. Pilipenko, R. Spatschek, E. A. Brener, and H. Müller-Krumbhaar. Crack propagation as a free boundary problem. *Phys. Rev. Lett.*, 98(1):015503, 2007.
- [98] P. Rabinowitz. *Numerical Methods for Nonlinear Algebraic Equations*. Gordon and Breach Science Publishers, London, 1970.
- [99] A. Rätz, A. Ribalta, and A. Voigt. Surface evolution of elastically stressed films under deposition by a diffuse interface model. *Journal of Computational Physics*, 214:187–208, May 2006.
- [100] K. Ravi-Chandar and W. G. Knauss. An experimental investigation into dynamic fracture: II. microstructural aspects. *International Journal of Fracture*, 26(1):65–80, 1984.
- [101] R. Roscoe. The viscosity of suspensions of rigid spheres. *British Journal of Applied Physics*, 3:267–269, Aug. 1952.
- [102] R. Roscoe. Isotropic composites with elastic or viscoelastic phases: General bounds for the moduli and solutions for special geometries. *Rheologica Acta*, 12(3):404–411, Sep 1973.
- [103] J. A. Sethian. *Level set methods: evolving interfaces in geometry, fluid mechanics, computer vision, and materials science*. Cambridge University Press, 2nd edition, 1999.
- [104] E. Sharon and J. Fineberg. Microbranching instability and the dynamic fracture of brittle materials. *Phys. Rev. B*, 54(10):7128–7139, Sep 1996.
- [105] E. Sharon and J. Fineberg. Confirming the continuum theory of dynamic brittle fracture for fast cracks. *Nature*, 397:333–335, Jan 1999.
- [106] K. A. Snyder, E. J. Garboczi, and A. R. Day. The elastic moduli of simple two-dimensional isotropic composites: Computer simulation and effective medium theory. *Journal of Applied Physics*, 72(12):5948–5955, 1992.

- [107] R. Spatschek, E. A. Brener, and D. Pilipenko. Crack growth by surface diffusion in viscoelastic media. *ArXiv e-prints*, 803, Mar 2008.
- [108] R. Spatschek and M. Fleck. Influence of stress on interface kinetics. *Philosophical Magazine Letters*, 87:909–914, 2007.
- [109] R. Spatschek, M. Hartmann, E. A. Brener, H. Müller-Krumbhaar, and K. Kassner. Phase field modeling of fast crack propagation. *Phys. Rev. Lett.*, 96(1):015502, 2006.
- [110] R. Spatschek, C. Müller-Gugenberger, E. Brener, and B. Nestler. Phase field modeling of fracture and stress-induced phase transitions. *Phys. Rev. E*, 75(6):066111–+, Jun 2007.
- [111] R. Spatschek, D. Pilipenko, C. Müller-Gugenberger, and E. A. Brener. Phase field modeling of fracture and composite materials. *ndt.net*, 11, Dec 2006.
- [112] M. Spivak. *A Comprehensive Introduction to Differential Geometry*, volume 5. Publish or Perish, Berkeley, U.S.A., 2nd edition, 1979.
- [113] A. N. Stroh. A theory of the fracture of metals. *Advances in Physics*, 6:418–465, Oct 1957.
- [114] J. Virieux. P-sc wave propagation in heterogeneous media: Velocity-stress finite difference method. *Geophys.*, 51:889, 1986.
- [115] W. Wang and Z. Suo. Shape change of a pore in a stressed solid via surface diffusion motivated by surface and elastic energy variation. *J. Mech. Phys. Solids*, 45(5):709–729, 1997.
- [116] A. A. Wheeler, G. B. McFadden, and W. J. Boettinger. Phase-field model for solidification of a eutectic alloy. *Proc. Royal Soc. A*, 452(1946):495–525, 1996.
- [117] W. H. Yang and D. J. Srolovitz. Cracklike surface instabilities in stressed solids. *Phys. Rev. Lett.*, 71(10):1593–1596, 1993.
- [118] W. H. Yang and D. J. Srolovitz. Surface morphology evolution in stressed solids: Surface diffusion controlled crack initiation. *Journal of the Mechanics and Physics of Solids*, 42(10):1551–1574, 1994.
- [119] D. H. Yeon, P.-R. Cha, and M. Grant. Phase field model of stress-induced surface instabilities: Surface diffusion. *Acta Materialia*, 54(6):1623–1630, 2006.

## B. Acknowledgements

First, I thank Prof. Dr. Heiner Müller-Krumbhaar for the interesting topics proposed, for providing such a good research environment and for the helpful and stimulating discussions. I am especially grateful for profiting from his long scientific experience and profound advice as well as from his active solution-oriented approach not only to scientific problems.

Next, I would like to express my gratitude to Dr. Robert Spatschek. His intuition, his patience, his effectiveness and his steady optimism were inspiring. He always took the time to discuss my problems and was always there when the going got tough. Through his encouragement to tackle challenging problems, his friendly and team-oriented attitude and by his persevering input, he greatly influenced this thesis, becoming not only a mentor but a friend along the way.

My special thanks go to Dr. Efim Brener for sharing his scientific opinions and knowledge. His door was always open and he always took the time to clear up any questions that arose. His unique approach to science and his ability to ask interesting, clear-cut questions were always helpful for focussing my efforts.

I thank Prof. Dr. Klaus Kassner, Universität Magdeburg, for the interesting, stimulating and fruitful collaboration. His creativity, thoroughness and care for detail were invaluable for the research undertaken in this thesis. His pedagogical and precise explanations of complex coherences provided many insights that found their way in this work.

I thank Prof. Dr. Walter Selke for agreeing to be the second referee of this thesis.

Luise Snyders deserves thanks not only for her organizational support, but even more for being the good natured soul of the Theory III-group.

Thanks to all members of Theory III and Theory I of the Institut für Festkörperforschung for many stimulating, interesting and pleasant conversations as well as arduous soccer games. In particular, I thank Andreas Dolfen, Prof. Dr. Dederichs, Dr. Phivos Mavrououlos, Dr. Theo Costi and Dr. Denis Pilipenko for interesting discussions and their friendly support.

My regards go to our System Administration Staff, especially Joseph Heinen, for his competence in effectively solving the occasional computer problems and for allowing for such a seamless computing environment.

I have to express special gratitude to my colleagues Claas Hüter and Michael Fleck.

---

The scientific discussions were always stimulating, helpful and, most importantly, fun. I am indebted for the effort put into corrections and suggestions concerning the manuscript of this thesis. But above all, I thank for the deep and sincere friendship that extended far beyond our professional lives.

I want to thank my parents Anna-Sophie and Christian, my brother Pascal and my sisters Aniella and Ariane. Despite the distance, they were always close, caring and understanding. I am deeply grateful for my parent's steady support of all my undertakings without which this work would have never been possible.

Finally, I want to thank my wife Caroline for all her love, understanding, support, for putting up with me during the difficult times, for the many happy moments and for truly being my Significant Other.

## C. Publications

Parts of this thesis have been published in the following journals:

- D. PILIPENKO, R. SPATSCHEK, E. BRENER AND C. MÜLLER-GUGENBERGER, Continuum Theory of Fracture, *ndt.net* **11** (2006). (Chapter 5).
- R. SPATSCHEK, D. PILIPENKO, C. MÜLLER-GUGENBERGER AND E. BRENER, Phase Field Modeling of Fracture and Composite Materials, *ndt.net* **11** (2006). (Chapter 5).
- R. Spatschek, C. Müller-Gugenberger, E. Brener and B. Nestler, Phase field modeling of fracture and stress-induced phase transitions, *Phys. Rev. E* **75**, 066111 (2007). (Chapter 5).
- C. GUGENBERGER, R. SPATSCHEK AND K. KASSNER, Comparison of phase-field models for surface diffusion, *Phys. Rev. E* **78**, 016703 (2008). (Chapter 3 and Chapter 4).
- E. Brener, C. Gugenberger, H. Müller-Krumbhaar, D. Pilipenko, R. Spatschek, D. E. Temkin, Elastic effects on phase transitions in multicomponent alloys, in D. Herlach (Editor): “Phase Transformations in Multicomponent Melts”, Wiley-VCH, 1. Auflage (2008). (Chapter 5)



---

# Curriculum Vitae

**Name:** Clemens Gugenberger

**Date of birth** May 6th, 1976

**Place of birth** Filderstadt-Plattenhardt, Germany

**Nationality** German

**Address:** Institut für Festkörperforschung  
Forschungszentrum Jülich  
Leo-Brandt-Straße  
52025 Jülich  
Germany  
e-mail: clemens.gugenberger@yahoo.de

## Education:

09/2005 – 09/2008 Dissertation in condensed matter physics:  
Free-Boundary Problem of Crack Dynamics: Phase-Field Modeling  
Supervisors: Prof. Dr. Heiner Müller-Krumbhaar  
Research Conducted at the Institut für Festkörperforschung  
Forschungszentrum Jülich, Germany  
Dissertation submitted at the RWTH Aachen, Germany

05/2005 – 09/2005 Research Scientist at the Institut für Theoretische Physik  
Universität zu Köln, Germany

04/2004 – 05/2005 Diploma in theoretical condensed matter physics:  
Entanglement und Phasenübergänge in niedrigdimensionalen Spin-Systemen  
Supervisor: Prof. Dr. Achim Rosch & Prof. Dr. Andreas Schadschneider  
Institut für Theoretische Physik, Universität zu Köln, Germany

09/1997 – 04/2004 Studying physics at the Universität zu Köln, Germany

08/1996 – 09/1997 Civil service at the retirement home "Haus am Weinberg" in Stuttgart, Germany

06/1996 Abitur (high-school graduation) at the Kepler-Gymnasium Tübingen, Germany